NANOPOROUS POLYMER/CERAMIC SEPARATOR ELECTROLYTE FOR LITHIUM METAL BATTERY APPLICATIONS

A Thesis

Presented to the Faculty of the Graduate School

Of Cornell University

In Partial Fulfillment of the Requirements for the Degree of

Master of Science

By

Zhengyuan Tu

August 2014

Abstract

In this thesis we report a family of novel nanoporous polymer/ceramic separator electrolyte for application in lithium metal battery. These unique polymer/ceramic composites are achieved by laminating a thin membrane of nanoporous ceramic with macroporous polymer.

Starting with preparing such composite with nanoporous alumina and Poly(vinylidene fluoride-co-hexafluoropropene) (PVDF-HFP), we have obtained composite membranes with good mechanical properties and high ionic conductivity. The membranes are soaked with lithium bis(trifluoromethanesulfonyl)imide/propylene carbonate (LiTFSI/PC) to infuse the nanopores with a liquid electrolyte. The similar lamination technique is also proved to be effective for other ceramics including nanoporous silica and lithium conducting glass. Further electrochemical experiments prove their ability to prevent dendrite formation and proliferation in lithium metal batteries, which ensures efficient battery cycling performance.

Motivated by theory, which predicts that LiF is able to form a covering on lithium surface which facilitates the lithium ion diffusion, we further blend alumina/PVDF-HFP/LiTFSI/PC separator electrolyte with LiF as SEI additive. The alumina/PVDF-HFP/LiTFSI/PC with 30% LiF exhibits the best performance in preventing dendrite formation, with which the battery is able to stably operate over 1000 hours.

The well-known benefit of single ion conductors for lithium battery stimulates us to further explore the functionalization alumina/polymer by either modifying the alumina surface or varying the charge status of polymer. Attempts have been made on functionalizing alumina membrane with ionic liquid, as well as laminating alumina with lithiated Nafion.

BIOGRAPHIC SKETCH

Zhengyuan was born in Nanchang, a medium-size city in south-eastern China. His childhood was surrounded by the love from his family. After receiving secondary education in Nanchang Foreign Language School, he was recommended for admission to Chu-Kochen honor college in Zhejiang University to pursue his Bachelor's degree. Although Zhengyuan's parents once expected him to become an architect in future, they finally agreed to let this young man to find his own life path. He chose Polymer Science and Engineering as major and English as minor, receiving an interdisciplinary education as well as research training. Zhengyuan started his voyage of scientific research under the supervision of Prof. Changyou Gao, Prof. Lie Ma, and Prof. Qiwen Teng. This voyage lasted through Zhengyuan's undergraduate time and extended to his graduate life in Cornell University. Zhengyuan was enrolled in M.S. program in Materials Science field at Cornell University under the guidance of Prof. Lynden A. Archer and Prof. Ulrich B. Wiesner. There he devoted himself into the research related to novel materials for lithium batteries.

ACKNOWLEDGEMENTS

I would like to thank my advisor, Professor Lynden A. Archer, for his patience and wise guidance through my two years research. I have received uncountable benefits from our pleasing conversations regarding professional and personal topics. In addition, Professor Archer's enthusiasm and outlook for research have always been the source of inspiration to me.

I also want to acknowledge my parents, for their unselfish, constant and great love to me. They are my spiritual support during my two years life abroad. Our frequent chats through phone or web have always comforted and relieved me.

I am also grateful to my friends from my high school, my college and here in Cornell, whose accompany and encouragement inspire me to insist on my dream.

Finally I want to thank my colleagues in the lab, whose presence make the research fun. Our discussions about work and life have been very valuable and beneficial for me.

CONTENT

Chapter 1

Introduction

1.1 Motivation

Energy is the foundation for nearly all human activities including lighting, heating, transportation, manufacture and food production that are essential for the sustainable development of the modern society. At present worldwide energy supplies overly rely on fossil fuels (coal, petroleum and natural gas) in which particularly petroleum dominates the majority of energy sources. As non-renewable resources, fossil fuels require millions of years to form while are consumed disproportionally faster than new ones being made. Even an optimistic estimate based on the energy consumption rate today predicts that petroleum and gas will be depleted in less than one century. This predicament underscores the need to not only develop new energy source such as solar, wind and nuclear power but also more importantly to explore new approach to consume and store energy efficiently [1]. Energy storage technology thus has received considerable attentions recently for minimizing energy waste, allowing flexible portability and alleviating pollution. It is urgent to design efficient, safe and large capacity electrochemical energy storage device to fulfill the sustainable energy need.

Rechargeable batteries are considered as promising energy storage units for their high energy output efficiency, pollution-free operation, compact structure and continuously decreasing cost [2-4]. Their high energy density, fast charging/discharging ability and portability satisfy the need for the large-scale deployment in mobile electronics, hybrid electric vehicles (HEVs), and even grid electricity storage [5-7]. Especially, lithium ion batteries (LIB) due to their high potential difference, high capacity and high Coulombic efficiency, become one of the most attractive candidates as the next generation secondary batteries. Since being commercialized in 1991, LIBs have been widely applied in cellphones, laptops, and video cameras with new functions that are impossible decades ago, as well as in HEVs and automatic aircrafts which forecasts a revolution

towards high efficiency and environmental-friendly transportation [8, 9]. The market of LIBs shows a rapidly growing trend in foreseeable future. As predicted, the LIBs sales will increase 100% in four years, showing a rising need for high energy density and low cost batteries. Thus, a broad and attractive market based on LIBs is formed and it is stimulating both academia and industry to develop and design better LIBs (**Figure** 1.1).

Currently although LIBs have achieved great success, their further development and applications are limited by the adoption of low capacity carbonaceous materials as anode which cannot meet the high energy requirement in the future [10]. It has long been realized that a metallic lithium anode which contains no carbon host will enhance the specific capacity of the state-of-art LIBs by as much as ten-fold [8], and will broaden the choice of high capacity cathode such as sulfur [11] and oxygen [12]. As the most electronegative metal, lithium is able to offer high potential difference against various cathodes and thus provides a large electrochemical driving force [13]. A lithium metal anode also minimizes the battery weight due to its low density. Together, these benefits promote the extensive research on lithium metal batteries (LMBs), which specifically refers to lithium batteries with lithium metal anode [14].

The major limitation that impedes the commercialization of LMBs is the potential safety issue known as ‘dendrite caused short circuit’. It stems from the uneven electrodeposition of lithium metal on the anode surface during battery charging, leading to continuous proliferation of dendritic lithium metal which will eventually connect the cathode and anode in the cell [15, 16]. The resultant electronic conductive pathway shorts the battery and generates heat that may cause fire, explosion and other serious hazards. One should note that the dendrite problem is not only limited to LMB but can also happen in LIB, due to the small potential difference that separates lithium ions from depositing onto and inserting into the electrode host. Thus, a LIB can be

(a)

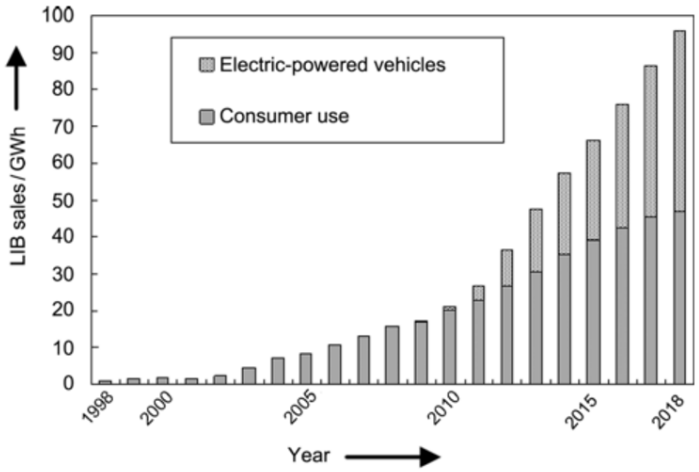

(b)

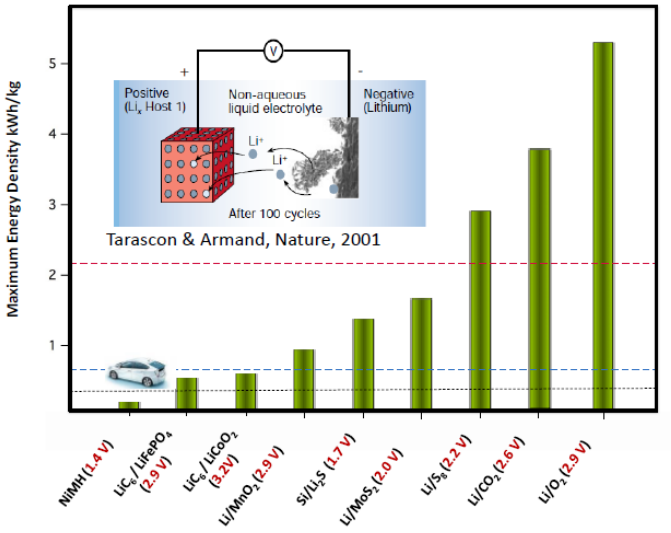

Figure 1.1. a) Expected LIB sales in the next decade. Reproduced with permission [15]. Copyright (2012) WILEY-VCH Verlag GmbH & Co. KGaA, Weinheim. b) theoretical specific energy and nominal voltage for various Li based rechargeable batteries. Red line and black line are long term and short term targets, respectively. Blue line is the target for HEVs. Reproduced with permission [8, 17]. Copyright (2001) Nature Publishing Group. Copyright (2012) WILEY-VCH Verlag GmbH & Co. KGaA, Weinheim

transformed into a LMB in which lithium metal replaces lithium carbon compound as anode if the battery is over charged or too quickly charged, facing the same risk from dendrite growth as LMB [8].

Many approaches have been explored to prevent dendrite growth in the past decades [18]. The list includes blending electrolyte with additive that stabilizes lithium deposition [19], ex-situ modification of electrode by surface coating to retard dendrite proliferation [20], application of external pressure to flatten the dendritic protuberance [21] and so on. Particularly, adopting high modulus electrolytes such as lithium conductive polymer or ceramics has support from theory and has been experimentally verified that they provide satisfactory dendrite suppression ability [22, 23]. However, current high modulus electrolytes either show low ionic conductivity which limits their room temperature application, or lack of accessibility and easy-handleness that are essential for LMB production [24, 25].

1.2 Structure of the thesis

In this work, we report a family of novel ceramic/polymer composites soaked with liquid electrolyte as high-modulus and high conductive separator/electrolytes for LMB. The composites are conveniently created by laminating strong ceramics with polymers. Further study involves blending the composite separator/electrolyte with SEI additives as well as with Nafion to create single-ion conducting composite electrolyte. The organization of the thesis is as follows,

In Chapter 2 a brief review of lithium battery technology is presented from the birth of lithium battery to the challenges it faces today. Lithium metal batteries show much higher capacity and

versatile compatibility with high energy cathode compared with the state-of-art lithium ion battery, but the application of LMBs is limited by safety problem caused by dendrite-induced short circuit. The focus is placed on the dendrite formation mechanism, methods to study dendrite behavior, as well as strategies that have been developed to suppress dendrite growth.

Chapter 3 presents the study of the composite separator prepared by laminating nanoporous alumina with macroporous PVDF-HFP using a phase separation approach. The resultant separator is soaked with 1M LiTFSI/PC solution. The materials structure, mechanical properties, impedance spectra, and battery performance are carefully characterized. The composite separator/electrolyte show great ability to suppress dendrite and achieve long-term stable battery operation.

In chapter 4 we report on the nanoporous silica-based separators for lithium metal batteries. Nanoporous silica is prepared by sintering silica nanoparticles near their melting points to form interconnected open structures. It is observed that such membrane has good mechanical toughness and high ionic conductivity when imbibed with liquid electrolyte.

An improvement of alumina/PVDF-HFP/LiTFSI/PC electrolyte by incorporating LiF as SEI additive into the composite is discussed in Chapter 5. It is concluded based on a theory that the halide ions, especially fluoride is able to greatly reduce the energy barrier for lithium diffusion on the surface. Thus, the stability of lithium electrodeposition can be enhanced at the presence of fluoride. After we blend alumina/PVDF-HFP/LiTFSI/PC with LiF, a stable battery operation for thousands of hours is achieved and no dendrite proliferation is observed in the the post-mortem SEM study.

In chapter 6 we consider single-ion conductor based on alumina/polymer membranes with both satisfactory conductivity and high modulus. The single-ion conductors allow LMBs to be

charged/discharged at high rate and can delay dendrite growth by neutralizing the space charge region which is thought to be the source for dendrite. Attempts are placed on lithium conductive ceramic electrolyte and laminated nanoporous ceramic/Nafion membrane. Their conductivity, impedance, lithium transference number and battery performance are evaluated.

Reference

1. Sims, R.E.H., H.H. Rogner, and K. Gregory, *Carbon emission and mitigation cost comparisons between fossil fuel, nuclear and renewable energy resources for electricity generation.* Energy Policy, 2003. **31**(13): p. 1315-1326.
2. Inaba, M., *Rechargeable Batteries as Innovative Energy Storage Devices.* Electrochemistry, 2010. **78**(5): p. 318-318.
3. Bruce, P.G., *Energy storage beyond the horizon: Rechargeable lithium batteries.* Solid State Ionics, 2008. **179**(21-26): p. 752-760.
4. Franger, S., C. Benoit, and R. Saint-Martin, *The electrochemical energy storage: contribution of the rechargeable lithium-ion batteries.* Actualite Chimique, 2008(325): p. 41-44.
5. Soloveichik, G.L., *Battery Technologies for Large-Scale Stationary Energy Storage.* Annual Review of Chemical and Biomolecular Engineering, Vol 2, 2011. **2**: p. 503-527.
6. Goodenough, J.B., *Evolution of Strategies for Modern Rechargeable Batteries.* Accounts of Chemical Research, 2013. **46**(5): p. 1053-1061.
7. Dunn, B., H. Kamath, and J.M. Tarascon, *Electrical Energy Storage for the Grid: A Battery of Choices.* Science, 2011. **334**(6058): p. 928-935.
8. Tarascon, J.M. and M. Armand, *Issues and challenges facing rechargeable lithium batteries.* Nature, 2001. **414**(6861): p. 359-367.
9. Chiang, Y.M., *Building a Better Battery.* Science, 2010. **330**(6010): p. 1485-1486.

10. Choi, N.S., et al., *Challenges Facing Lithium Batteries and Electrical Double-Layer Capacitors.* Angewandte Chemie-International Edition, 2012. **51**(40): p. 9994-10024.

11. Barghamadi, M., A. Kapoor, and C. Wen, *A Review on Li-S Batteries as a High Efficiency Rechargeable Lithium Battery.* Journal of the Electrochemical Society, 2013. **160**(8): p. A1256-A1263.

12. Christensen, J., et al., *A Critical Review of Li/Air Batteries.* Journal of the Electrochemical Society, 2012. **159**(2): p. R1-R30.

13. Megahed, S. and B. Scrosati, *Lithium-Ion Rechargeable Batteries.* Journal of Power Sources, 1994. **51**(1-2): p. 79-104.

14. Simon, G.K. and T. Goswami, *Improving Anodes for Lithium Ion Batteries.* Metallurgical and Materials Transactions a-Physical Metallurgy and Materials Science, 2011. **42A**(1): p. 231-238.

15. Yoshino, A., *The Birth of the Lithium-Ion Battery.* Angewandte Chemie-International Edition, 2012. **51**(24): p. 5798-5800.

16. Brissot, C., et al., *In situ study of dendritic growth in lithium/PEO-salt/lithium cells.* Electrochimica Acta, 1998. **43**(10-11): p. 1569-1574.

17. Lu, Y.Y., et al., *Ionic Liquid-Nanoparticle Hybrid Electrolytes and their Application in Secondary Lithium-Metal Batteries.* Advanced Materials, 2012. **24**(32): p. 4430-4435.

18. Xu, W., et al., *Lithium metal anodes for rechargeable batteries.* Energy & Environmental Science, 2014. **7**(2): p. 513-537.

19. Eweka, E., J.R. Owen, and A. Ritchie, *Electrolytes and additives for high efficiency lithium cycling.* Journal of Power Sources, 1997. **65**(1-2): p. 247-251.

20. Umeda, G.A., et al., *Protection of lithium metal surfaces using tetraethoxysilane.* Journal of Materials Chemistry, 2011. **21**(5): p. 1593-1599.

21. Gireaud, L., et al., *Lithium metal stripping/plating mechanisms studies: A metallurgical approach.* Electrochemistry communications, 2006. **8**(10): p. 1639-1649.

22. Kalnaus, S., et al., *Design of composite polymer electrolytes for Li ion batteries based on mechanical stability criteria.* Journal of Power Sources, 2012. **201**: p. 280-287.

23. Monroe, C. and J. Newman, *The impact of elastic deformation on deposition kinetics at lithium/polymer interfaces.* Journal of the Electrochemical Society, 2005. **152**(2): p. A396-A404.

24. Agrawal, R.C. and G.P. Pandey, *Solid polymer electrolytes: materials designing and all-solid-state battery applications: an overview.* Journal of Physics D-Applied Physics, 2008. **41**(22).

25. Hayashi, A., *Development of new glassy materials for all-solid-state lithium secondary batteries: a review.* Glass Technology-European Journal of Glass Science and Technology Part A, 2008. **49**(5): p. 213-220.

Chapter 2

Background

2.1 A brief history of lithium batteries

Compared with primary batteries which can only provide one-time discharge and whose disposal seriously harm the environment, secondary (rechargeable) batteries have energy as a popular power source especially for devices that require large amount of electric energy. Before the appearance of lithium ion batteries in late 20^{th} century, the market of rechargeable batteries is dominated by conventional lead-acid battery, nickel-cadmium battery and nickel-metal hydride batteries [26]. These conventional batteries generally used aqueous electrolyte which suffer from potential degradation caused by electrolysis, insufficient energy density and limited output voltage. On the contrary, non-aqueous electrolyte based batteries can provide much higher voltage (>3V) and larger capacity. As one of the most promising secondary batteries with non-aqueous electrolyte, lithium rechargeable batteries had received extensive attentions since 1960, 70s [6, 27] (**Figure** 2.1).

The birth of lithium rechargeable battery originate from three scientific achievements. Firstly, the incomparable physical and chemical properties of lithium, which include electronegativity, low density and high specific capacity, which make metallic lithium suitable as anode [28]. Secondly scientists discovered the phenomenon known as electrochemical intercalation, which has become the basis of reversible lithium transportation in battery [8, 29]. Also, cathode materials for lithium batteries are feasible thanks to the discovery of various inorganic compounds with special crystal structures that are able to accommodate lithium ion [30, 31]. All together, these achievements have catalyzed numerous research and application-oriented projects on developing lithium batteries. For example, Exxon started a lithium battery project in 1972 trying to produce coin cells for watches with metallic lithium anode and TiS_2 cathode [32], in which TiS_2 possesses a well-defined layered structure that is preferable for reversible ion intercalation.

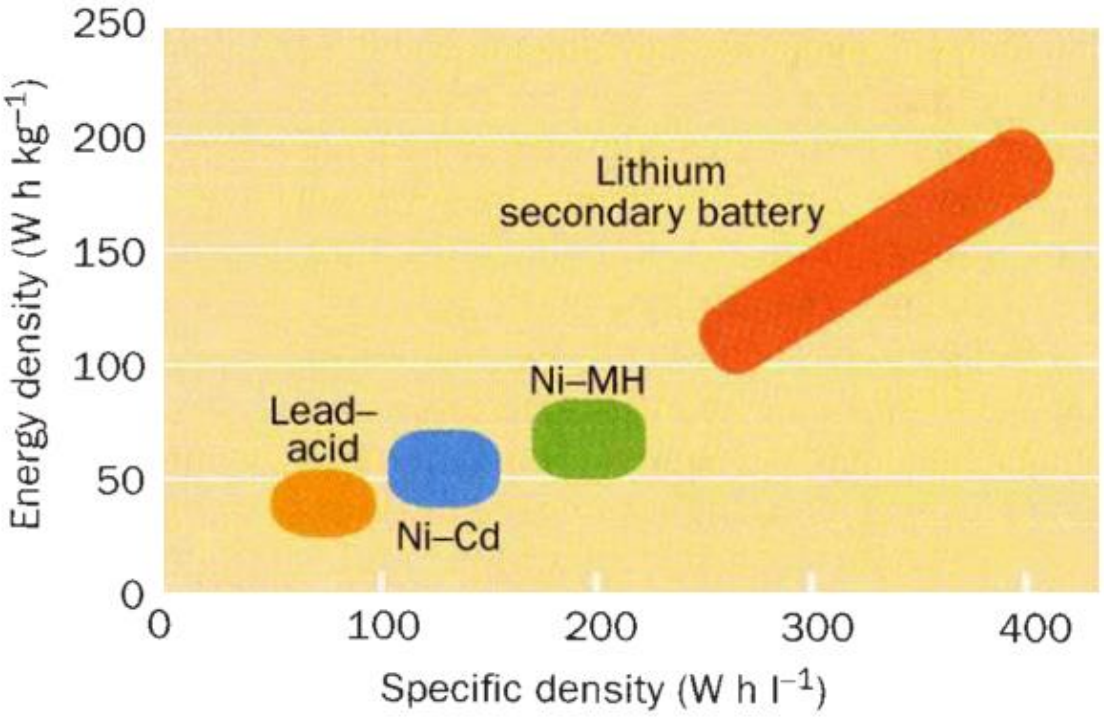

Figure 2.1. A comparison of the energy density and the specific density among lead acid (yellow), Ni-Cd (blue), Ni-Metal hybrid (green) and lithium secondary battery (red). Adapted with permission [26]. Copyright (1995), Nature Publishing Group.

However, this type of battery soon encountered the safety problem caused by dendritic lithium growth on the anode as mentioned in the previous section [15]. One proposed solution was to blend lithium and aluminum to create an alloy anode. Unfortunately the alloy anode has its own problem, which is the uncontrollable volume expansion during cycles [33, 34]. Since then many methods, such as the adoption of polymer electrolyte [16, 35, 36] have been proposed to solve the dendrite problem in lithium metal batteries, but none have achieved ultimate success [37]. The application of lithium metal batteries was thus strictly limited by their short lifetime and potential safety problems.

A successful compromise solution to the dendrite problem appears late in 1980s. Instead of using metallic lithium, another electrode matrix for lithium intercalation was introduced as the anode. Thus the lithium exists in the form of intercalated ion instead of metal when the battery is in its fully charged status. It is the Li^+ ion that move reversibly between two intercalation electrodes through the electrolyte. This type of battery, which is firstly proposed by Murphy et al [38], Scrosati et al [39], and Yoshino et al [15], avoids uneven dendritic lithium electrodeposits and is known as lithium ion battery (LIBs). However, the development of LIBs still continues well into the next decade. Eventually after the struggling to find stable anode intercalation materials and correspondingly compatible electrolyte, carbon/$LiCoO_2$ lithium ion battery emerged as a probably successful configuration and was commercialized by Sony in 1991 [40]. Since then the market of LIBs flourished and better materials for LIBs with high capacity, fast charging rate and stable performance have been continuously discovered and prepared [24, 37, 41]. Afterwards the LIBs have become one of the most important and popular rechargeable power sources.

Modern LIBs generally take the form as shown in **Figure** 2.2, in which two electrodes are capable of accommodating lithium ions and connecting with an external circuit through an electronically conducting current collector, while the electrolyte plays as the ionic conductive pathway allowing reversible movement of solvated lithium ion [7]. Electrolyte as well as the cathode and anodes are regarded as the two most critical components in a LIB and great efforts have been devoted to design and improve their performance. In the following section a brief introduction of these components are presented. We are not targeting comprehensiveness considering the vast number of existing works in the literature, and a few influential reviews have been published for readers' information.

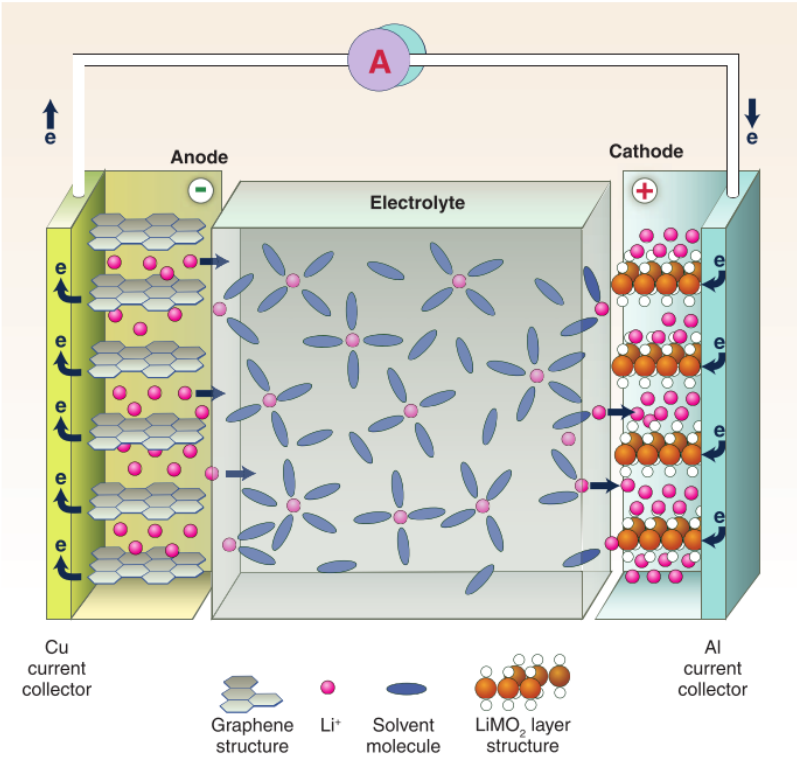

Figure 2.2. A schematic description of the general structure of lithium ion battery. Adapted with permission [7]. Copyright (2011) AAAS Publishing

2.2 Electrolyte

A good electrolyte is required to effectively shuttle lithium ions but to block electron flows. It should also remain thermally and electrochemically stable under various conditions for a long period of time. Although generally it is regarded that electrolyte refers to a lithium-salt-doped organic solution, in a general perspective, the electrolyte for lithium battery can be any lithium conductive substance. Currently the most widely studied electrolytes can be roughly divided into four categories: liquid, polymer and ceramic electrolyte, as well as any combinations among the three.

Liquid electrolytes are studied probably the earliest and the most [42]. The common compositions of liquid electrolytes, including ethylene carbonate (EC), propylene carbonate (PC) dimethyl carbonate (DMC),diethyl carbonate (DEC), etc. doped with lithium salt ($LiPF_6$, LiTFSI, Li(triflate), etc.), are able to offer high ionic conductivity (usually 10^{-3} S/cm), good ion disassociation and low interfacial impedance [43]. Some other chemical species known as electrolyte additives sometimes are blended with electrolytes to enhance performance. However, these electrolytes are flammable, volatile, leaky, thermally unstable and show narrow voltage stability window, which greatly impede their large-scale deployment in batteries [43]. Some non-flammable solvents have been regarded as candidate to substitute aprotic organic esters. The list includes TEGDME in combine with LiTFSI which shows great potential as the electrolyte for high energy Li/S battery [44, 45], a number of ionic liquid with great thermal and electrochemical stability for those electrodes require high voltage [17, 46], and environmental friendly aqueous electrolyte that has achieved preliminary success in Li/O_2 batteries [47].

More recently the appearance of solid state electrolytes offer additional options to prepare electrolyte with stable performance, reduced flammability and no potential leakage [48, 49]. The

representatives are lithium conductive polymers and ceramics. Polymer electrolytes are usually composed of conductive polymer (such as PEO) and lithium salt. Studies show that the transport of lithium ions in polymer electrolyte occurs by ion hoping among the active sites as well as by polymer backbone movement [50]. The polymer electrolytes are promising to serve as both electrolyte and separator in lithium metal batteries due to their solid nature may provide enough good mechanical property to prevent dendritic lithium growth. However, there is a trade-off between the high modulus and high conductivity due to the crystallinity of the polymer, which means a highly amorphous polymer may favor ion transport ability, but undermine the mechanical property and vice versa. A smart solution to this dilemma is the application of block polymers (for example, PS-PEO block copolymer) with two polymer species that provide strength and conductivity separately. Some studies show that cross-linked version of such polymer can also provide satisfactory dual properties required for battery electrolytes [51, 52].

Ceramic electrolytes are attractive among solid electrolytes by far for extreme thermal stability as well as very high modulus up to 100 GPa, thus they are preferable in high-temperature batteries and for dendrite prevention purposes [53, 54]. The conduction of ceramic electrolyte originates from the movement of lithium defects, which is sensitively temperature dependent and crystal structure dependent. A number of lithium phosphate, oxide and sulfide show attractive conductivity larger than 10^{-3} S cm^{-1} at room temperature, but most of their practical applications as electrolyte are limited by the incompatibility with electrodes typically used in batteries [43, 53]. Surprisingly LIPON, a lithium phosphate based compound which exhibits room temperature conductivity of 10^{-5} S cm^{-1}, has received wide application as high-modulus ceramic electrolyte [55, 56]. This interest stems from the fact that the LIPON thin film shows reduced impedance when the number of grain boundary decreases. A more serious challenge with ceramic

electrolyte is their brittle nature. The easily breakable ceramic electrolyte seems unfeasible for batteries used in mobile devices especially for HEV, where high compressive stress during manufacturing and deployment are typical.

Thus, either liquid electrolyte or solid state electrolyte shows respective shortcomings, but those can be covered by creating solid/liquid composite electrolyte. It is well known that the swelling property of polymers, especially cross-linked or high molecular weight ones, allows polymer to store considerable amount of liquid and form a gel. The same principle applies when a polymer is soaked with liquid electrolyte, which can provide liquid-like high ionic conductive even though the polymer is not lithium conductive intrinsically [57-60]. A famous example is the PVDF/EC-DMC based gel-like electrolyte firstly developed by Bellcore Corp, which provides high ionic conductivity at room temperature, sufficient for LIB application [61]. Gel-electrolytes offer advantages from both liquid (high conductivity) and polymer (robustness), which at one point allowed them to be considered as the potential electrolyte for stopping dendritic lithium growth. However, it soon turned out that they still suffer from flammability, volatility and insufficient mechanical strength [62, 63]. Another type of gel-like electrolyte, known as soggy sand, is a composite of liquid electrolyte and ceramic. When the doping level of ceramic particles in the liquid electrolyte reaches a percolation threshold, the whole system shows gel-like behavior [64, 65]. Soggy sands show comparable conductivity as liquid electrolytes and also receive potential benefits from the functionable high surface area particles they include. However their structure and behaviors still require more fundamental investigation. More recently, a type of novel polymer/ceramic hybrid materials appears to be a promising candidate for the electrolytes [66]. The configuration of such hybrid materials involves homogeneous distribution of one phase in another by a number of chemistry approaches, which shows much

better miscibility compared with traditional polymer/ceramic filler composites prepared by simple blending. Our group has proposed and synthesized an inorganic/organic hybrid materials by modifying the surface of ceramic nanoparticles with polymer chains or charged chemical species [67, 68]. The formed self-suspension nanoparticles systems exhibit satisfactory ionic conductivity, high lithium transference number, and great chemistry flexibility.

2.3 Cathode

Since the first success of $LiCoO_2$, a number of materials have been researched to explore their feasibility as lithium battery cathode. Two famous examples regarded as the potential substitutes for $LiCoO_2$ cathode are the families of $LiMn_2O_4$ [69] and $LiFePO_4$ [70]. The spinel $LiMn_2O_4$ offers very high potential from Mn^{4+}/Mn^{3+} redox pair and a more successful attempts involves substituting partial Mn with Cr which provides even higher oxidation state (Cr^{3+} to Cr^{6+}). $LiFePO_4$ type electrodes benefits from its unique structure with Fe(or Ti, V, Nb) O_6 octahedral and P (or S, As, Mo, W) O_4 tetrahedral which are able to well accommodate lithium ions [8], which also exhibits outstanding stability and low cost. After the poor conductivity of $LiFePO_4$ was overcome by creating nanostructure or carbon coating, the family of $LiFePO_4$ is seriously considered as the one of the most promising electrode materials for HEV application [71]. More recently a family of compounds formed by lithium, nickel, manganese, and cobalt, known as NMC cathode were discovered. They are capable of providing very high potential, close to 5V, as well as stable cycling performance with negligible capacity fading [72].

Although the research on the above mentioned cathode materials have achieved promising results, they all have insufficient capacity lower than 300 mAh/g which cannot satisfy the constantly increasing energy requirement for most devices (**Figure** 2.3). The limited capacity of

those chemical species arises from the fact that only one electron is transferred between the redox state, thus it is preferable to have materials that are able to reversibly change in states by two or more electron units. For example, vanadium based electrodes represent a family of cathodes with large redox/oxidation valence gap from V^{5+} to $V^{3.5+}$ or less. The similar principle is also valid in W, Wo and Nb based oxides, but their specific capacity are not significantly enlarged due to the presence of heavy metals. Chances for the next generation of cathode materials exist in the chemical species such as sulfur and oxygen [73, 74], which are not only able to provide multiple electrons for reversible reaction, but also exhibit very low molecular weight that two together largely enhance the specific capacity by more than ten-fold compared with the state-of-art LIBs. Meanwhile the abundance and the economic accessibility of these elementary substances allow potential large-scale production of high energy batteries in an environment friendly way. More recently the concept of using CO_2 as cathode for rechargeable lithium battery has been raised [75]. This innovation connects the field of high energy generation and carbon capture, providing interdisciplinary opportunities towards the next generation of clean and sustainable energy sources.

One should note that the research on Li-S and Li-air batteries are still at the preliminary stage. The challenges mainly lie in the materials incompatibility as well as lacking understanding of the reaction mechanism. Sulfur is known to be able to reversibly combine with lithium, but its

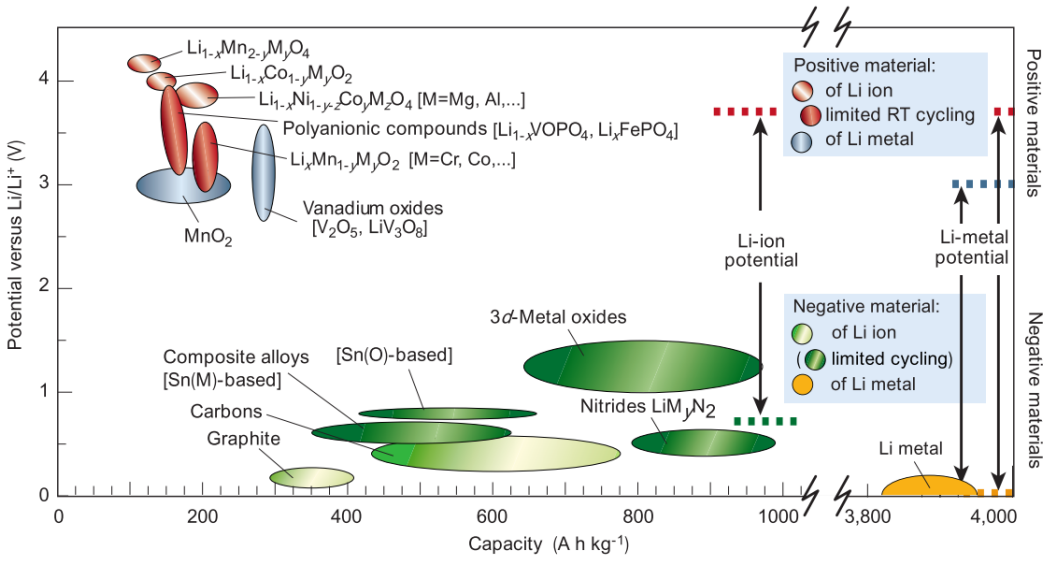

Figure 2.3. Potential and capacity of various cathode and anode materials. Adapted with permission [8]. Copyright (2001) Nature Publishing Group

application as rechargeable lithium batteries are impeded due to quickly capacity fading caused by the formation of undissolvable low ordered Li_xS_y precipitates [11]. Li-air batteries although have been extensively studied in the past decade, a number of fundamental mechanism still remain unrevealed [76]. It's clear that massive energy are required to be continuously invested to develop high energy cathode through the next several decades.

2.4 Anode

As the counter electrode against cathode, preferably anode materials should be able to offer low potential and balanced specific capacity as cathodes to achieve considerable total energy storage ability. The first successful lithium intercalation material used on the anode side, Graphite, has been gradually replaced by a number of carbon anode with higher capacity. These carbonaceous anodes are achieved by either chemical modification or fine tuning of carbon structure/morphology [77]. But carbon based anodes are not considered as the most ideal anode for LIBs, due to their intercalation voltage for lithium ion only show slight difference compared with the potential for Li^+/Li transformation. That means a serious safety concern that the lithium ions could deposit on carbon substrate and thus form a LMB with high risk to short circuit [8]. As the options to substitute carbon anode, lithium metal oxides [78], chalcogenides [79], and nitrides [80] have been extensively study for lithium batteries application. A family of Li_xMVO_4 (with M can be Ni, Co, Cd, Zn, etc.) compounds and $LiMN_x$ (for example $Li_xCo_yN_z$) have been discovered with high specific capacity, but their poor cycling stability compromise their battery performance. $Li_4Ti_5O_{12}$ as electrode materials [81, 82] can achieve stable electrochemical cycling at a wide range of rates but the low capacity around 175 mAh/g cannot be considered

attractive. Contrast to the inorganic materials, some conductive polymers including polythiophene, polyacetylene, and polyphenylene have been invested as lithium storage materials. Although polymer anodes exhibit advantage on the flexibility and cost, they only show moderate specific capacity and conductivity, as well as poor stability.

In parallel, vast attentions have been given on a completely different approach towards high energy anode by creating lithium/metal alloy [83-86]. Early attempts involves blending lithium with other metals such as aluminum, which enhances the specific capacity and avoids potential safety issue. But soon it shows that the Li/Al alloy undergoes complicated structure deformation and even phase transformation during battery operation, which causes a fatal volume expansion over 200% [87]. Efforts have been placed on alleviating the great volume expansion by either tuning the metallurgical structure (such as grain size) of Li alloys, or more intuitively by introducing an inactive component as the buffer matrix to accommodate deformation and expansion [88]. Even though these approaches moderately enhance the battery lifetime, they significantly downgrade the capacity with respect to the total weight of the electrode. A commercial example of alloy anode appears at the end of the 20^{th} century by Fujifilm Celltech. They have prepared a type of cell with tin oxides based composite as the anode known as Stalion, in which Sn^{2+} center is considered as lithium active sites while the rest components including B^{3+}, Al^{3+} etc. play as the stabilizing network [89]. Unfortunately Stalion cell did not achieve great commercial success, likely due to irreversible huge capacity loss and unsatisfactory cycling performance.

Although all above mentioned studies on anode have achieved more or less improvements on either specific capacity or electrode stability, the future of anode materials is still facing challenge. The dilemma for all present anode materials for LIBs is that they show much less

capacity than the next generation cathodes (sulfur, oxygen, etc.). A simple solution will be using metallic lithium as anode, which provides the most negative potential as well as 10 time higher capacity than carbon based anodes. As stated previously, the core limitation for LMBs relates to the metallic dendrite growth and resultant short circuit. Thus the future of high energy lithium batteries highly depends on the overcome of dendrite growth. In fact, dendrite related study remains topical for thirty years. The mechanism of dendrite formation and proliferation have been extensively investigated. Those as well as the efforts to prevent dendrite growth are introduced in the next section.

2.5 Lithium dendrite characterization and mechanism

In the last forty years or so, scientists have devoted great energy into investigating the behavior of lithium dendrite growth by using a number of characterization methods. These methods can be roughly divided into two categories: methods to observe the lithium surface morphology and to study the surface chemical composition [18]. These methods together have provided valuable information for understanding the dendrite growth mechanism.

Surface morphology

Probably the simplest and the most direct tool to observe the lithium surface is optical microscopy (OM). OM provides sufficient resolution (micro-level) to identify dendrites (usually larger than 10 micros) and also can be used as the in situ tool to study the dendrite behavior on live [16, 90, 91]. In most studies OM is combined with a video camera to record dendrite growing process. A designed device with OM and CCD camera for in situ observation of dendrite growth is shown in **Figure** 2.4. The microscopy with camera is placed vertically in between two electrodes in a sealed electrochemical cell. Such device is able to conveniently

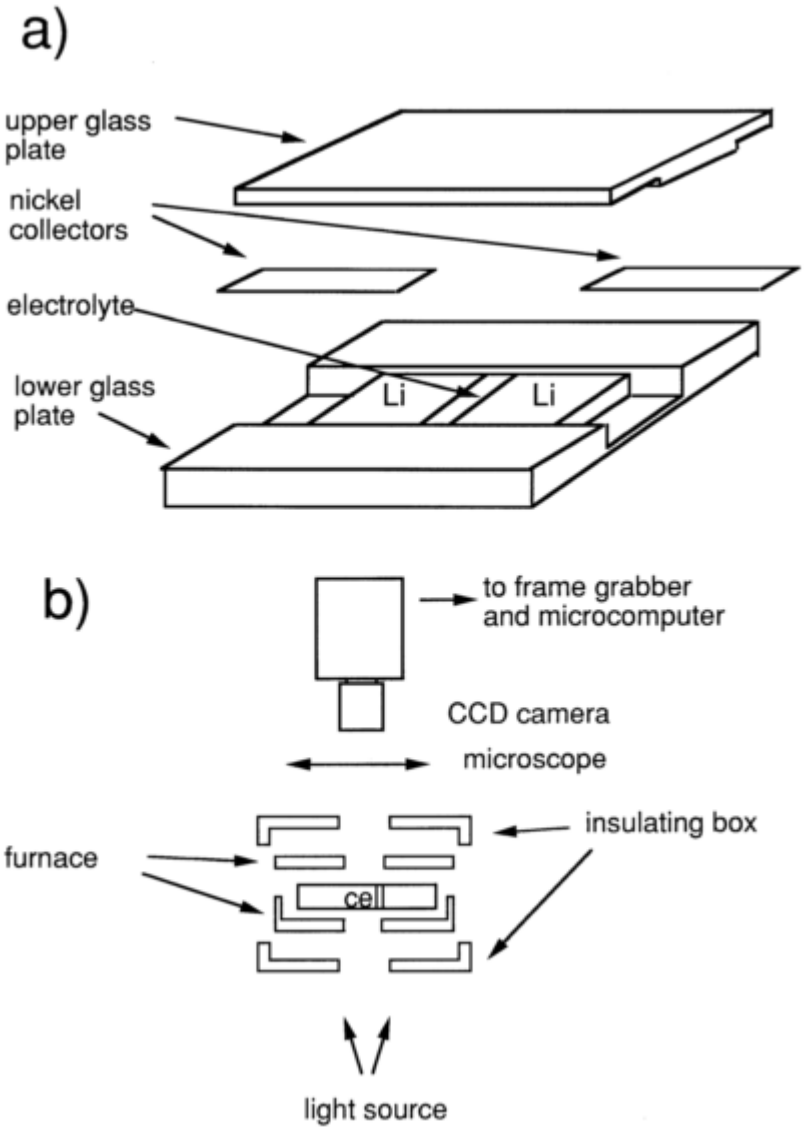

Figure 2.4 Schematic representation of a set of OM equipment for dendrite observation. Adapted with permission [16]. Copyright (1998) Elsevier Science Ltd.

gather information including dendrite growing velocity, dendrite size and shape under different current density, electrolyte species and SEI additives. Those information are particularly important for constructing mathematical model to describe dendrite behavior. However, the resolution of OM is not high enough to clearly observe the lithium surface details. Thus OM is not ideal for fine dendrite studies, such as the research on the initial dendrite formation whose nucleation process takes place at a small length scale.

Scanning Electron Microscopy (SEM) and Transmission Electron Microscopy (TEM) offer much higher resolution than OM thus they are capable of providing images of more detailed pattern and morphology on the lithium surface. SEM and TEM have been extensively used for lithium surface observation in post-mortem studies [92-95]. **Figure** 2.5 shows some SEM pictures of lithium surface and cross-section, in which the local dendrite morphology is clearly revealed. Unfortunately, the high vacuum requirements of electron microscopies downgrade the convenience of in situ dendrite observation as OM. It is also concerned the high vapor pressure of liquid electrolytes on the lithium electrode can be detrimental to the machines. Thanks to the advance of microscopy technology, recently in situ TEM and air-SEM are available for live dendrite studies. In future electron microscopies will still be the main tool for dendrite morphology characterization.

Atomic Force Microscopy (AFM) is another useful tool for dendrite visualization. It provides high resolution as well as the ability to generate unique 3-dimension graph for the sample [96, 97]. Thus more deeply buried surface information such as grain boundaries, local bumps and valley, etc. can be observed and studied. Another attraction of AFM for dendrite study is that by comparing the contact force and penetration depth, the local mechanical property on the surface can be measured. Aubach et al proposed a ‘surface breakdown and repair’ empirical theory

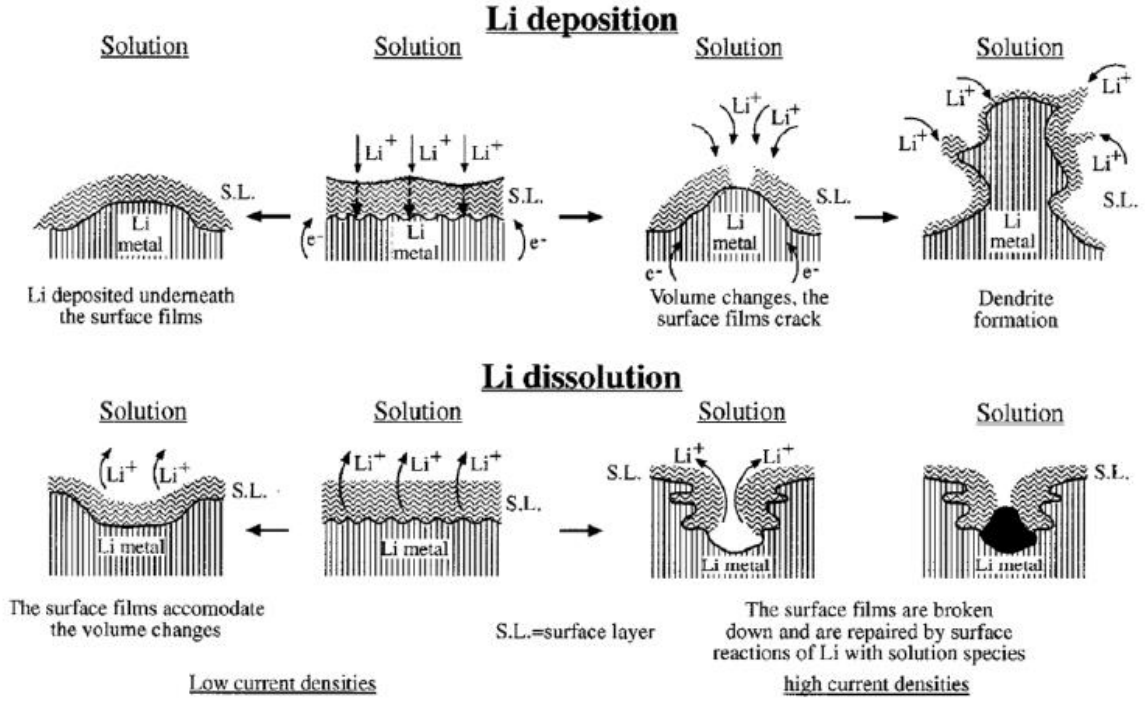

Figure 2.6. The SEI 'breakdown' theory based on in situ AFM study. Adapted with permission [97]. Copyright (2000) American Chemistry Society.

based on AFM study on lithium surface [97, 98]. They claim that the repeated process between SEI layer formation and decomposition motivates the proliferation of dendrites, which is illustrated in **Figure** 2.6.

Chemistry analysis

The chemistry analysis of lithium surface is critical to study the effect of electrolyte on lithium surface deposition as well as the battery performance. It has long been realized that a solid insoluble interface will be formed between the lithium and electrolyte, known as solid electrolyte interface or SEI layer during the initial stage of the battery operation [99]. SEI layer is composed of the electrolyte as well as its degradation product by reacting with active lithium. The layer, although being only several nanometers thick, passives the lithium surface from further reaction with electrolyte while still allowing ion transport [100]. The composition of SEI layer strongly influence the lithium deposition and dendrite behavior, as well as the interfacial resistance and lithium ion diffusivity. Thus, careful scrutiny of lithium surface chemistry are highly imperative.

In principle, any analytical techniques can be used to investigate lithium surface, but the challenge comes from the reactivity of lithium metal. It is preferable for the analytical technique to be sensitive, easy to operate and compatible with the lithium sample. FTIR and XPS are the most commonly used examine tools for metallic lithium anode surface [96, 101-103], for both can provide fine chemical composition information in a non-destructive way. Advanced FTIR is extremely sensitive to organic bond thus it is useful for identifying chemical species from electrolyte. XPS can work as a supplement for detecting inorganic components with satisfying accuracy by scanning the binding energy. With the help of ion sputtering technique, XPS can even reveal the chemical composition of each layer on lithium surface at different depth. (**Figure**

2.7). By combining these FTIR and XPS, the majority of chemicals, including lithium oxide, lithium hydroxide, lithium carbonate, etc. on lithium have been identified. Other techniques including AES, Raman, Total reflection X-ray, etc. [104-106] have also been employed for lithium surface characterization, and new technologies are emerging for better and more accurate study.

Models

Based on the information obtained from above mentioned techniques, scientists are able to analyze and model the mechanism of dendrite formation theoretically. In fact, metallic dendrite formation is not limited to lithium, but is common in many other metals such as silver and zinc [107, 108]. The very first model of dendritic metal growth is on silver dendrite proposed by Barton and Bockris in 1962 [108], which predicts the relationship between the dendrite growth rate and the dendrite tip radius. An improvement was made by Diggle et al. on zinc dendrites by introducing kinetic expression in the equation [109]. The formation of cooper dendrite is also investigated and the influence of several additives on dendrite morphology are studied [110]. Although fruitful models and mechanisms on dendrite formation are proposed and experimentally studied, this field is still not completely understood. For example, a long puzzled phenomenon is that magnesium will hardly form dendritic structure during electrodeposition [111]. Apparently more investigations need to be conducted to develop more general and convincing model.

The research on mechanism of lithium dendrite formation and growth arise rapidly due to its importance for lithium battery industry. Chazaviel et al [112] proposed that the growth of metallic dendrite is motivated by the electric field from the space charge region which is formed

due to anion depletion near cathode. Thus, the growth velocity of the dendrite is closely related to the velocity of anions. $v_a = -\mu_a E_0$, which is the velocity of the anions, determined by anion mobility μ_a and the electric field E_0.

This theory was proved by Brissot et al [16] using an in situ dendrite observation device, but the experiment condition was far from the true battery. They also pointed out that Chazaviel's model needed to take ion mobility, diffusion parameter and ion concentration into account. Brissot et al [63, 113] also studied the effect of current density on the onset time of dendrite growth in a Li/polymer-salt system. They proposed a cross-over current density which divides two situations in which the anion concentration will and will not deplete, respectively. Below this cross-over current density J*, the anion concentration will not go to zero at negative electrode thus the electrochemical cells show stable behavior. On the contrary, if the current density is larger than J*, anion will deplete and the cell potential starts to diverge at the Sand's time, which is the time the anion concentration goes to zero:

$$\tau = \pi D\left(\frac{C_0 e}{2 J t_a}\right)^2 \text{ with } t_a = \frac{\mu_a}{\mu_a + \mu_c}$$

t_a is the anionic transport number.

The equation of Sand's time reveals that a high cation transference number can delay the onset of dendrite growth, which becomes the fundament of many research on single-ion conductors for lithium battery recently.

One should note that Chazaviel's model only considers the simplest 1D scenario. Uncertainty in Chazaviel's model is that experiment shows that even at low current density, the dendrite will still form. This might be because of the uneven pristine lithium surface or passivation SEI layer.

Other lithium plating/striping test also reveals the strong influence of surface morphology on dendrite formation and proliferation.

More recently Monroe and Newman [23, 107, 114] proposed a simulation model to describe dendrite growth verified by the data from Li/oxymethylene-linked polyethylene oxide/LiTFSI system at high temperature. They constructed concentration profiles, potential profiles and equations expressing dendrite proliferation velocity. It is shown that with time goes on, the concentration gradient enlarges and so does space charge potential. The dendrite growth always accelerates during the galvanostatic polarization, and it's strongly related to the applied voltage. The improvement of their model compared with Barton and Bockris theory is that the thermodynamic factors are considered to correct dendrite growth kinetics. The dendrite behaviors fit Newman's and Chazaviel's theories are both experimentally observed [115].

Next Monroe et al published two other following papers introducing the influence of mechanical force into their original theory [23, 114]. The new theory assumes that the small amplitude perturbation on the lithium surface provides seed for dendrite formation. According to their simulation, the current density at the 'peak' of the surface is higher than the 'valley', leading to the accumulation of deposited lithium on the 'peak' so that the dendrite proliferates. Further they introduced the stability parameter which is contributed from three parts: the compressive force, the deformation stress and the surface tension on lithium surface. The stability parameter is shown strong relation against shear modulus of the electrolyte and a negative stability parameter indicates the stable electrodespoition meaning the dendrite growth can be controlled. **Figure** 2.7 reports the value of stability parameter against normalized modulus and it can be seen that surface tension contributes to the electrode stability while the deformation stress contributes to the instability. The compressive force contributes to the electrode stability with the modulus

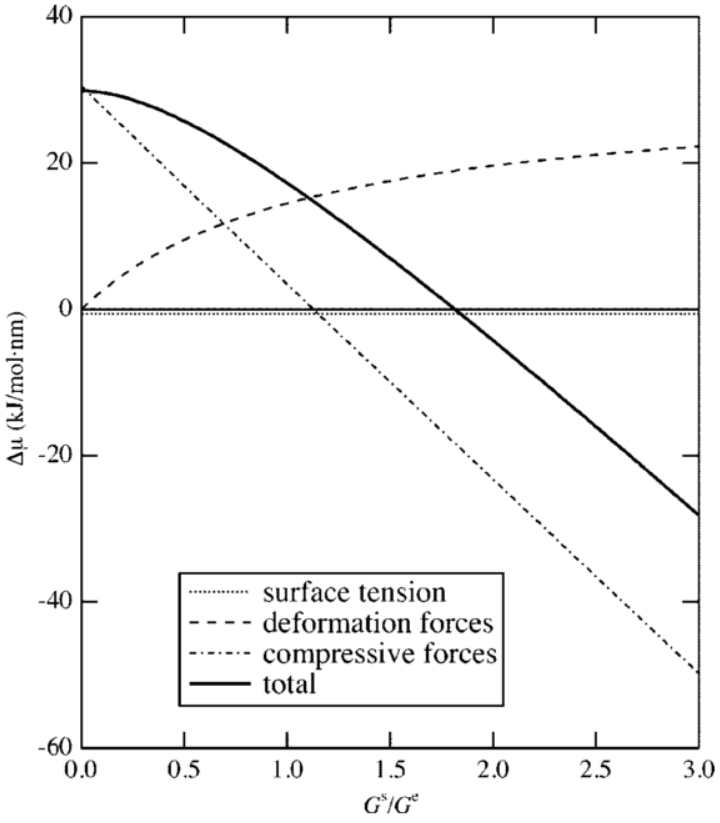

Figure 2.7. The variation of stability parameter and its three components with the change of the separator modulus. Adapted with permission [23]. Copyright (2005) The Electrochemical Society, Inc.

increase. The total value of stability parameter falls below zero when the shear modulus of the electrolyte is twice as large as that of lithium metal, indicating no dendrite growth.

Dendrite prevention approaches

For decades people explore many approaches to prevent dendrite growth in lithium metal battery. At first it is found that blending lithium with other metals such as aluminum or magnesium to form an alloy anode is effective on dendrite formation [87, 116], but this type of alloy suffers from fatal volume expansion during battery operation. Scientists further investigated ex-situ method to form homogeneous passivation layer on lithium by surface treatment with TEOS, silane ligand, cross-linked polymer etc.[117, 118], which suppress the dendrite growth. Introducing so-called SEI additives into electrolyte, including various lithium salt, hydrocarbonate, and even CO_2 are proved to be useful in forming more uniform SEI layer [119-121], which is capable of facilitating stable deposition of lithium. Besides the improvement on the electrode and electrolyte, optimizing battery working condition can also diminish the appearance of dendrite [122]. For example, the application of external pressure on lithium anode is able to flatten the interface between electrode and electrolyte [123].

Based on Newman's theories previously described, introducing high modulus solid-like electrolyte to mechanically block the dendrite growth is regarded as a promising method. Bellcore Corp has for example developed PVDF-HFP gel-like electrolyte made by phase separation of the polymer and then soaking with liquid electrolyte [61]. The resultant lithium conductive gel shows comparable conductivity as liquid electrolyte while maintain solid form. Cross-linked PEG is also widely investigated as solid-like electrolyte for lithium battery due to

the fact that lithium is able to hopping among the PEG chains to transport [124]. Block polymers cast new light on polymer electrolyte research due to their ability to combine the benefits of several polymers together, as well as that they can easily form some nanopattern which may direct dendrite behavior [125]. Recently a PE based block polymer electrolyte with special nanostructure, known as DryLyte R, has been developed for lithium battery. This polymer has lithium conductive nanochannels distributed in the bulk while still maintains high shear modulus, which allows lithium ion to pass by but block the dendrite if it is formed. While various polymers and their derivatives show promising future for lithium battery, their application are limited by the low ionic conductivity at room temperature, making polymer electrolytes only suitable for stationary power supplies with heating facilities instead of mobile applications. Other than polymers, lithium conductive ceramics, such as LiPON or LISCON [56, 126], receive more attentions these days due to their extremely high modulus which are usually several orders of magnitude higher than polymers. However, their conductivity rarely reach the requirement for normal battery operation, which greatly limit their application at room temperature. Meanwhile their brittleness nature makes the battery assembly difficult and may cause unexpected breaking down during battery operation, especially for the battery used in transporting applications.

In Chazaviel's model, the dendrite growth rapidly if the anion depletes and the space charge region forms and the onset time of dendrite is inversely proportional to the cation transference number. Thus it's preferable to avoid dramatic ion concentration gradient or to enhance lithium transference number. For example, self-suspended suspensions of polyethylene glycol (PEG) functionalized nanoparticles have been shown to undergo a jamming transition, leading to the formation of a nanoporous network of a lithium conductive PEG phase which is also mechanically reinforced by a silica nanoparticle network [67]. Further study shows that the

particle network can even been chemically cross-linked to enhance mechanical property. While the confinement of PEG in the nanopores leads to moderate enhancements in Li transference number, its conductivities at the room temperature are not high. By blending similar silica nanoparticles tethered with an ionic liquid (IL) in a conventional propylene carbonate (PC) - lithium bis(trifluoromethanesulfonyl)imide (LiTFSI) electrolyte, It is showed that high ionic conductivities compared to liquid electrolyte can be achieved in such hybrids at room temperature. And, when used as the electrolytes in LMBs, the IL-nanoparticle hybrid electrolytes lead to as much as a ten-fold increase in cell lifetime. Specifically, it was argued that because the anion (TFSI) is the same for both the nanoparticle-tethered IL and for the IL in the electrolyte salt, the IL-tethered particles provide a reservoir of TFSI throughout the electrolyte that reduces the anion concentration gradient and thus diminish the space charge region. More recently a self-healing approach has been proposed for dendrite prevention through mixing small amounts of Cesium salt with a lithium salt-based electrolyte [127]. This method has so far shown promising ability to prevent lithium dendrite formation in electrochemical deposition of lithium electrodes, but it has been insufficiently studied to determine its applicability to LMBs cycled at moderate and high current densities.

Reference

1. Sims, R.E.H., H.H. Rogner, and K. Gregory, *Carbon emission and mitigation cost comparisons between fossil fuel, nuclear and renewable energy resources for electricity generation.* Energy Policy, 2003. **31**(13): p. 1315-1326.
2. Inaba, M., *Rechargeable Batteries as Innovative Energy Storage Devices.* Electrochemistry, 2010. **78**(5): p. 318-318.

3. Bruce, P.G., *Energy storage beyond the horizon: Rechargeable lithium batteries.* Solid State Ionics, 2008. **179**(21-26): p. 752-760.

4. Franger, S., C. Benoit, and R. Saint-Martin, *The electrochemical energy storage: contribution of the rechargeable lithium-ion batteries.* Actualite Chimique, 2008(325): p. 41-44.

5. Soloveichik, G.L., *Battery Technologies for Large-Scale Stationary Energy Storage.* Annual Review of Chemical and Biomolecular Engineering, Vol 2, 2011. **2**: p. 503-527.

6. Goodenough, J.B., *Evolution of Strategies for Modern Rechargeable Batteries.* Accounts of Chemical Research, 2013. **46**(5): p. 1053-1061.

7. Dunn, B., H. Kamath, and J.M. Tarascon, *Electrical Energy Storage for the Grid: A Battery of Choices.* Science, 2011. **334**(6058): p. 928-935.

8. Tarascon, J.M. and M. Armand, *Issues and challenges facing rechargeable lithium batteries.* Nature, 2001. **414**(6861): p. 359-367.

9. Chiang, Y.M., *Building a Better Battery.* Science, 2010. **330**(6010): p. 1485-1486.

10. Choi, N.S., et al., *Challenges Facing Lithium Batteries and Electrical Double-Layer Capacitors.* Angewandte Chemie-International Edition, 2012. **51**(40): p. 9994-10024.

11. Barghamadi, M., A. Kapoor, and C. Wen, *A Review on Li-S Batteries as a High Efficiency Rechargeable Lithium Battery.* Journal of the Electrochemical Society, 2013. **160**(8): p. A1256-A1263.

12. Christensen, J., et al., *A Critical Review of Li/Air Batteries.* Journal of the Electrochemical Society, 2012. **159**(2): p. R1-R30.

13. Megahed, S. and B. Scrosati, *Lithium-Ion Rechargeable Batteries.* Journal of Power Sources, 1994. **51**(1-2): p. 79-104.

14. Simon, G.K. and T. Goswami, *Improving Anodes for Lithium Ion Batteries.* Metallurgical and Materials Transactions a-Physical Metallurgy and Materials Science, 2011. **42A**(1): p. 231-238.

15. Yoshino, A., *The Birth of the Lithium-Ion Battery.* Angewandte Chemie-International Edition, 2012. **51**(24): p. 5798-5800.

16. Brissot, C., et al., *In situ study of dendritic growth in lithium/PEO-salt/lithium cells.* Electrochimica Acta, 1998. **43**(10-11): p. 1569-1574.

17. Lu, Y.Y., et al., *Ionic Liquid-Nanoparticle Hybrid Electrolytes and their Application in Secondary Lithium-Metal Batteries.* Advanced Materials, 2012. **24**(32): p. 4430-4435.

18. Xu, W., et al., *Lithium metal anodes for rechargeable batteries.* Energy & Environmental Science, 2014. **7**(2): p. 513-537.

19. Eweka, E., J.R. Owen, and A. Ritchie, *Electrolytes and additives for high efficiency lithium cycling.* Journal of Power Sources, 1997. **65**(1-2): p. 247-251.

20. Umeda, G.A., et al., *Protection of lithium metal surfaces using tetraethoxysilane.* Journal of Materials Chemistry, 2011. **21**(5): p. 1593-1599.

21. Gireaud, L., et al., *Lithium metal stripping/plating mechanisms studies: A metallurgical approach.* Electrochemistry communications, 2006. **8**(10): p. 1639-1649.

22. Kalnaus, S., et al., *Design of composite polymer electrolytes for Li ion batteries based on mechanical stability criteria.* Journal of Power Sources, 2012. **201**: p. 280-287.

23. Monroe, C. and J. Newman, *The impact of elastic deformation on deposition kinetics at lithium/polymer interfaces.* Journal of the Electrochemical Society, 2005. **152**(2): p. A396-A404.

24. Agrawal, R.C. and G.P. Pandey, *Solid polymer electrolytes: materials designing and all-solid-state battery applications: an overview.* Journal of Physics D-Applied Physics, 2008. **41**(22).

25. Hayashi, A., *Development of new glassy materials for all-solid-state lithium secondary batteries: a review.* Glass Technology-European Journal of Glass Science and Technology Part A, 2008. **49**(5): p. 213-220.

26. Scrosati, B., *Battery Technology - Challenge of Portable Power.* Nature, 1995. **373**(6515): p. 557-558.

27. Whittingham, M.S., *History, Evolution, and Future Status of Energy Storage.* Proceedings of the Ieee, 2012. **100**: p. 1518-1534.

28. Scrosati, B. and J. Garche, *Lithium batteries: Status, prospects and future.* Journal of Power Sources, 2010. **195**(9): p. 2419-2430.

29. Levi, M.D. and D. Aurbach, *The mechanism of lithium intercalation in graphite film electrodes in aprotic media .1. High resolution slow scan rate cyclic voltammetric studies and modeling.* Journal of Electroanalytical Chemistry, 1997. **421**(1-2): p. 79-88.

30. Reddy, A.L.M., et al., *Hybrid Nanostructures for Energy Storage Applications.* Advanced Materials, 2012. **24**(37): p. 5045-5064.

31. Whittingham, M.S., *Lithium batteries and cathode materials.* Chemical Reviews, 2004. **104**(10): p. 4271-4301.

32. Whittingham, M.S., *Electrical Energy-Storage and Intercalation Chemistry.* Science, 1976. **192**(4244): p. 1126-1127.

33. Gay, E.C., et al., *Performance-Characteristics of Solid Lithium-Aluminum Alloy Electrodes.* Journal of the Electrochemical Society, 1976. **123**(11): p. 1591-1596.

34. Kumagai, N., Y. Kikuchi, and K. Tanno, *Cycling Behavior of Lithium Aluminum-Alloys Formed on Various Aluminum Substrates as Negative Electrodes in Secondary Lithium Cells.* Journal of Applied Electrochemistry, 1992. **22**(7): p. 620-627.

35. Duval, M., et al., *Development of Ion-Conducting Polymer Electrolytes for Use in High-Energy Lithium Rechargeable Batteries.* Makromolekulare Chemie-Macromolecular Symposia, 1989. **24**: p. 151-162.

36. Fauteux, D., et al., *Lithium Polymer Electrolyte Rechargeable Battery.* Electrochimica Acta, 1995. **40**(13-14): p. 2185-2190.

37. Doughty, D.H., *Materials issues in lithium ion rechargeable battery technology.* Sampe Journal, 1996. **32**(2): p. 75-81.

38. Murphy, D.W., et al., *Topochemical Reactions of Rutile Related Structures with Lithium.* Materials Research Bulletin, 1978. **13**(12): p. 1395-1402.

39. Lazzari, M. and B. Scrosati, *Cyclable Lithium Organic Electrolyte Cell Based on 2 Intercalation Electrodes.* Journal of the Electrochemical Society, 1980. **127**(3): p. 773-774.

40. Nagaura, T.T., K., *Lithium ion rechargeable battery.* Prog. Batteries Solar Cells, 1990. **9**(209).

41. Kulova, T.L., *New electrode materials for lithium-ion batteries (Review).* Russian Journal of Electrochemistry, 2013. **49**(1): p. 1-25.

42. Xu, K., *Nonaqueous liquid electrolytes for lithium-based rechargeable batteries.* Chemical Reviews, 2004. **104**(10): p. 4303-4417.

43. Schaefer, J.L., et al., *Electrolytes for high-energy lithium batteries.* Applied Nanoscience, 2012. **2**(2): p. 91-109.

44. Ryu, H.S., et al., *Discharge behavior of lithium/sulfur cell with TEGDME based electrolyte at low temperature.* Journal of Power Sources, 2006. **163**(1): p. 201-206.

45. Chang, D.R., et al., *Binary electrolyte based on tetra(ethylene glycol) dimethyl ether and 1,3-dioxolane for lithium-sulfur battery.* Journal of Power Sources, 2002. **112**(2): p. 452-460.

46. Lu, Y.Y., et al., *Ionic-Liquid-Nanoparticle Hybrid Electrolytes: Applications in Lithium Metal Batteries.* Angewandte Chemie-International Edition, 2014. **53**(2): p. 488-492.

47. Zhang, D., et al., *Review on Lithium-Air Batteries.* Progress in Chemistry, 2012. **24**(12): p. 2472-2482.

48. Ahmad, S., *Polymer electrolytes: characteristics and peculiarities.* Ionics, 2009. **15**(3): p. 309-321.

49. Robertson, A.D., A.R. West, and A.G. Ritchie, *Review of crystalline lithium-ion conductors suitable for high temperature battery applications.* Solid State Ionics, 1997. **104**(1-2): p. 1-11.

50. Hallinan, D.T. and N.P. Balsara, *Polymer Electrolytes.* Annual Review of Materials Research, Vol 43, 2013. **43**: p. 503-+.

51. Stone, G.M., et al., *Resolution of the Modulus versus Adhesion Dilemma in Solid Polymer Electrolytes for Rechargeable Lithium Metal Batteries.* Journal of the Electrochemical Society, 2012. **159**(3): p. A222-A227.

52. Hallinan, D.T., et al., *Lithium Metal Stability in Batteries with Block Copolymer Electrolytes.* Journal of the Electrochemical Society, 2013. **160**(3): p. A464-A470.

53. Fergus, J.W., *Ceramic and polymeric solid electrolytes for lithium-ion batteries.* Journal of Power Sources, 2010. **195**(15): p. 4554-4569.

54. Patil, A., et al., *Issue and challenges facing rechargeable thin film lithium batteries.* Materials Research Bulletin, 2008. **43**(8-9): p. 1913-1942.

55. Liu, J., et al., *All-solid-state Lithium Ion Battery: Research and Industrial Prospects.* Acta Chimica Sinica, 2013. **71**(6): p. 869-878.

56. Herbert, E.G., et al., *Mechanical characterization of LiPON films using nanoindentation.* Thin Solid Films, 2011. **520**(1): p. 413-418.

57. Bhattacharyya, A.J., M. Patel, and S.K. Das, *Soft matter lithium salt electrolytes: ion conduction and application to rechargeable batteries.* Monatshefte Fur Chemie, 2009. **140**(9): p. 1001-1010.

58. Zhao, F., et al., *Advances in ionic conductive polymer electrolytes.* Progress in Chemistry, 2002. **14**(5): p. 374-383.

59. Young, W.S., W.F. Kuan, and T.H. Epps, *Block Copolymer Electrolytes for Rechargeable Lithium Batteries.* Journal of Polymer Science Part B-Polymer Physics, 2014. **52**(1): p. 1-16.

60. Giridhar, P., et al., *A review on lithium - Ion polymer electrolyte batteries.* Bulletin of Electrochemistry, 1999. **15**(9-10): p. 414-418.

61. Du Pasquier, A., et al., *Plastic PVDF-HFP electrolyte laminates prepared by a phase-inversion process.* Solid State Ionics, 2000. **135**(1): p. 249-257.

62. Brissot, C., et al., *In situ concentration cartography in the neighborhood of dendrites growing in lithium/polymer-electrolyte/lithium cells.* Journal of the Electrochemical Society, 1999. **146**(12): p. 4393-4400.

63. Brissot, C., et al., *Dendritic growth mechanisms in lithium/polymer cells.* Journal of Power Sources, 1999. **81**: p. 925-929.

64. Bhattacharyya, A.J., M. Dollé, and J. Maier, *Improved Li-battery electrolytes by heterogeneous doping of nonaqueous Li-salt solutions.* Electrochemical and solid-state letters, 2004. **7**(11): p. A432-A434.

65. Das, S.K. and A.J. Bhattacharyya, *Oxide particle surface chemistry and ion transport in "soggy sand" electrolytes.* The Journal of Physical Chemistry C, 2009. **113**(16): p. 6699-6705.

66. Kao, H.M. and C.L. Chen, *An Organic–Inorganic Hybrid Electrolyte Derived from Self-Assembly of a Poly (Ethylene Oxide)–Poly (Propylene Oxide)–Poly (Ethylene Oxide) Triblock Copolymer.* Angewandte Chemie, 2004. **116**(8): p. 998-1002.

67. Nugent, J.L., S.S. Moganty, and L.A. Archer, *Nanoscale organic hybrid electrolytes.* Advanced Materials, 2010. **22**(33): p. 3677-3680.

68. Agarwal, P., H. Qi, and L.A. Archer, *The ages in a self-suspended nanoparticle liquid.* Nano letters, 2009. **10**(1): p. 111-115.

69. Armstrong, A.R. and P.G. Bruce, *Synthesis of layered LiMnO2 as an electrode for rechargeable lithium batteries.* Nature, 1996. **381**(6582): p. 499-500.

70. Wang, Y.G., P. He, and H.S. Zhou, *Olivine LiFePO4: development and future.* Energy & Environmental Science, 2011. **4**(3): p. 805-817.

71. Chung, S.Y., J.T. Bloking, and Y.M. Chiang, *Electronically conductive phospho-olivines as lithium storage electrodes.* Nature Materials, 2002. **1**(2): p. 123-128.

72. Ban, C., et al., *Extremely Durable High-Rate Capability of a LiNi0. 4Mn0. 4Co0. 2O2 Cathode Enabled with Single-Walled Carbon Nanotubes.* Advanced Energy Materials, 2011. **1**(1): p. 58-62.

73. Bruce, P.G., et al., *Li-O-2 and Li-S batteries with high energy storage.* Nature Materials, 2012. **11**(1): p. 19-29.

74. Miao, L.X., et al., *Sulfur Composite Cathode for Lithium-Sulfur Batteries.* Progress in Chemistry, 2013. **25**(11): p. 1867-1875.

75. Xu, S., S.K. Das, and L.A. Archer, *The Li–CO 2 battery: a novel method for CO 2 capture and utilization.* RSC Advances, 2013. **3**(18): p. 6656-6660.

76. Park, M., et al., *Lithium-Air Batteries: Survey on the Current Status and Perspectives Towards Automotive Applications from a Battery Industry Standpoint.* Advanced Energy Materials, 2012. **2**(7): p. 780-800.

77. Winter, M., et al., *Insertion electrode materials for rechargeable lithium batteries.* Advanced Materials, 1998. **10**(10): p. 725-763.

78. Poizot, P., et al., *Nano-sized transition-metal oxides as negative-electrode materials for lithium-ion batteries.* Nature, 2000. **407**(6803): p. 496-499.

79. Murphy, D. and F. Trumbore, *Metal chalcogenides as reversible electrodes in nonaqueous lithium batteries.* Journal of Crystal Growth, 1977. **39**(1): p. 185-199.

80. Shodai, T., et al., *Study of Li< sub> 3− x</sub> M< sub> x</sub> N (M: Co, Ni or Cu) system for use as anode material in lithium rechargeable cells.* Solid State Ionics, 1996. **86**: p. 785-789.

81. Leonidov, I., et al., *Structure, ionic conduction, and phase transformations in lithium titanate Li4Ti5O12.* Physics of the Solid State, 2003. **45**(11): p. 2183-2188.

82. Bohnke, O., C. Bohnke, and J. Fourquet, *Mechanism of ionic conduction and electrochemical intercalation of lithium into the perovskite lanthanum lithium titanate.* Solid State Ionics, 1996. **91**(1): p. 21-31.

83. Chu, D.B., et al., *Tin-Based Alloy Anode Materials for Lithium Ion Batteries.* Progress in Chemistry, 2012. **24**(8): p. 1466-1476.

84. Kamali, A.R. and D.J. Fray, *Tin-Based Materials as Advanced Anode Materials for Lithium Ion Batteries: A Review.* Reviews on Advanced Materials Science, 2011. **27**(1): p. 14-24.

85. Wu, D.H. and Z. Zhou, *Recent progress of computational investigation on anode materials in Li ion batteries.* Frontiers of Physics, 2011. **6**(2): p. 197-203.

86. Shi, Z., et al., *Electrochemical properties of Li-Mg alloy electrodes for lithium batteries.* Journal of Power Sources, 2001. **92**(1-2): p. 70-80.

87. Bang, H.J., S. Kim, and J. Prakash, *Electrochemical investigations of lithium-aluminum alloy anode in Li/polymer cells.* Journal of Power Sources, 2001. **92**(1-2): p. 45-49.

88. Anani, A., S. Crouch-Baker, and R. Huggins, *Kinetic and thermodynamic parameters of several binary lithium alloy negative electrode materials at ambient temperature.* Journal of the Electrochemical Society, 1987. **134**(12): p. 3098-3102.

89. Idota, Y., et al., *Tin-based amorphous oxide: a high-capacity lithium-ion-storage material.* Science, 1997. **276**(5317): p. 1395-1397.

90. Sano, H., H. Sakaebe, and H. Matsumoto, *Observation of electrodeposited lithium by optical microscope in room temperature ionic liquid-based electrolyte.* Journal of Power Sources, 2011. **196**(16): p. 6663-6669.

91. Howlett, P.C., D.R. MacFarlane, and A.F. Hollenkamp, *High lithium metal cycling efficiency in a room-temperature ionic liquid.* Electrochemical and Solid State Letters, 2004. **7**(5): p. A97-A101.

92. Orsini, F., et al., *In situ Scanning Electron Microscopy (SEM) observation of interfaces within plastic lithium batteries.* Journal of Power Sources, 1998. **76**(1): p. 19-29.

93. Dolle, M., et al., *Live scanning electron microscope observations of dendritic growth in lithium/polymer cells.* Electrochemical and Solid State Letters, 2002. **5**(12): p. A286-A289.

94. Orsini, F., et al., *Scanning and transmission electron microscopy contributions to the improvement of electrode materials and interfaces in the design of better batteries.* International Journal of Inorganic Materials, 2000. **2**(6): p. 701-715.

95. Orsini, F., et al., *In situ SEM study of the interfaces in plastic lithium cells.* Journal of Power Sources, 1999. **81**: p. 918-921.

96. Morigaki, K. and A. Ohta, *Analysis of the surface of lithium in organic electrolyte by atomic force microscopy, Fourier transform infrared spectroscopy and scanning auger electron microscopy.* Journal of Power Sources, 1998. **76**(2): p. 159-166.

97. Cohen, Y.S., Y. Cohen, and D. Aurbach, *Micromorphological studies of lithium electrodes in alkyl carbonate solutions using in situ atomic force microscopy.* Journal of Physical Chemistry B, 2000. **104**(51): p. 12282-12291.

98. Aurbach, D., et al., *New insights into the interactions between electrode materials and electrolyte solutions for advanced nonaqueous batteries.* Journal of Power Sources, 1999. **81**: p. 95-111.

99. Zhang, S.S., *A review on electrolyte additives for lithium-ion batteries.* Journal of Power Sources, 2006. **162**(2): p. 1379-1394.

100. Teyssot, A., et al., *Evolution of the electrode-electrolyte interface in a lithium-polymer battery.* Solid State Ionics, 2006. **177**(1-2): p. 141-143.

101. Li, J.T., et al., *Interfacial Processes of Lithium Ion Batteries by FTIR Spectroscopy.* Progress in Chemistry, 2011. **23**(2-3): p. 349-356.

102. Kanamura, K., et al., *Xps Analysis for the Lithium Surface Immersed in Gamma-Butyrolactone Containing Various Salts.* Electrochimica Acta, 1995. **40**(7): p. 913-921.

103. Verma, P., P. Maire, and P. Novak, *A review of the features and analyses of the solid electrolyte interphase in Li-ion batteries.* Electrochimica Acta, 2010. **55**(22): p. 6332-6341.

104. Stancovski, V. and S. Badilescu, *In situ Raman spectroscopic-electrochemical studies of lithium-ion battery materials: a historical overview.* Journal of Applied Electrochemistry, 2014. **44**(1): p. 23-43.

105. Takamatsu, D., et al., *First In Situ Observation of the LiCoO2 Electrode/Electrolyte Interface by Total-Reflection X-ray Absorption Spectroscopy.* Angewandte Chemie-International Edition, 2012. **51**(46): p. 11597-11601.

106. Ota, H., et al., *Characterization of lithium electrode in lithium imides/ethylene carbonate and cyclic ether electrolytes - II. Surface chemistry.* Journal of the Electrochemical Society, 2004. **151**(3): p. A437-A446.

107. Monroe, C. and J. Newman, *Dendrite growth in lithium/polymer systems - A propagation model for liquid electrolytes under galvanostatic conditions.* Journal of the Electrochemical Society, 2003. **150**(10): p. A1377-A1384.

108. Kan, J.Q., H.G. Xue, and S.L. Mu, *Effect of inhibitors on Zn-dendrite formation for zinc-polyaniline secondary battery.* Journal of Power Sources, 1998. **74**(1): p. 113-116.

109. Diggle, J., A. Despic, and J.M. Bockris, *The mechanism of the dendritic electrocrystallization of zinc.* Journal of The Electrochemical Society, 1969. **116**(11): p. 1503-1514.

110. Zhang, X.J., et al., *Copper dendrites: Synthesis, mechanism discussion, and application in determination of L-tyrosine.* Crystal Growth & Design, 2008. **8**(4): p. 1430-1434.

111. Matsui, M., *Study on electrochemically deposited Mg metal.* Journal of Power Sources, 2011. **196**(16): p. 7048-7055.

112. Chazalviel, J.N., *Electrochemical Aspects of the Generation of Ramified Metallic Electrodeposits.* Physical Review A, 1990. **42**(12): p. 7355-7367.

113. Rosso, M., et al., *Dendrite short-circuit and fuse effect on Li/polymer/Li cells.* Electrochimica Acta, 2006. **51**(25): p. 5334-5340.

114. Monroe, C. and J. Newman, *The effect of interfacial deformation on electrodeposition kinetics.* Journal of the Electrochemical Society, 2004. **151**(6): p. A880-A886.

115. Gonzalez, G., M. Rosso, and E. Chassaing, *Transition between two dendritic growth mechanisms in electrodeposition.* Physical Review E, 2008. **78**(1).

116. Vissers, D.R., K.E. Anderson, and F.C. Mrazek, *Effects of Metal Additives on Performance-Characteristics of Lithium-Aluminum Alloy Electrodes.* Journal of the Electrochemical Society, 1977. **124**(3): p. C136-C136.

117. Marchioni, F., et al., *Protection of lithium metal surfaces using chlorosilanes.* Langmuir, 2007. **23**(23): p. 11597-11602.

118. Lee, Y.M., et al., *Electrochemical performance of lithium/sulfur batteries with protected Li anodes.* Journal of Power Sources, 2003. **119**: p. 964-972.

119. Hughes, M., N.A. Hampson, and S.A.G.R. Karunathilaka, *A Review of Cells Based on Lithium Negative Electrodes (Anodes).* Journal of Power Sources, 1984. **12**(2): p. 83-144.

120. Aurbach, D., et al., *Correlation between Surface-Chemistry, Morphology, Cycling Efficiency and Interfacial Properties of Li Electrodes in Solutions Containing Different Li Salts.* Electrochimica Acta, 1994. **39**(1): p. 51-71.

121. Shiraishi, S., K. Kanamura, and Z. Takehara, *Surface condition changes in lithium metal deposited in nonaqueous electrolyte containing HF by dissolution-deposition cycles.* Journal of the Electrochemical Society, 1999. **146**(5): p. 1633-1639.

122. Chen, L., et al., *Bipolar pulse current charge method for inhibiting the formation of lithium dendrite.* Acta Physico-Chimica Sinica, 2006. **22**(9): p. 1155-1158.

123. Gireaud, L., et al., *Lithium metal stripping/plating mechanisms studies: A metallurgical approach.* Electrochemistry Communications, 2006. **8**(10): p. 1639-1649.

124. Borghini, M.C., M. Mastragostino, and A. Zanelli, *Reliability of lithium batteries with crosslinked polymer electrolytes.* Electrochimica Acta, 1996. **41**(15): p. 2369-2373.

125. Singh, M., et al., *Effect of molecular weight on the mechanical and electrical properties of block copolymer electrolytes.* Macromolecules, 2007. **40**(13): p. 4578-4585.

126. Puech, L., et al., *Elaboration and characterization of a free standing LiSICON membrane for aqueous lithium-air battery.* Journal of Power Sources, 2012. **214**: p. 330-336.

127. Ding, F., et al., *Dendrite-Free Lithium Deposition via Self-Healing Electrostatic Shield Mechanism.* Journal of the American Chemical Society, 2013. **135**(11): p. 4450-4456.

Chapter 3

NANOPOROUS ALUMINA/POLYMER LAMINATES AS SEPARATOR/ELECTROLYTE FOR LTIHIUM METAL BATTERIRES

Reproduced from Tu. et al. Advanced Energy Materials, 4(2), 2014

3.1 Introduction

In the previous chapter, it is shown that polymer and ceramic electrolyte suffer from either poor mechanical property or low room-temperature conductivity. Efforts have been made to combine polymer with inorganic fillers, such as silica nanoparticles to achieve composite benefits, but such strategy is limited by the inhomogeneous distribution of the filler particles in the polymer matrix. At first we have attempted a process involving preparing PEG attached SiO_2 nanoparticles/PVDF-HFP composite membrane. The hairy PEG-SiO2 are expected to strength the polymer while the attached PEG chains might facilitate uniform particle dispersion. However, the experiment results show that severe phase separation occurs between ceramic particles and the polymer phase, which deteriorates the structure and property of the composite membrane.

We further propose a ceramic/polymer composite electrolyte that offer both high modulus and high conductivity at room temperature after being soaked in liquid electrolyte. The composite is prepared by laminating nanoporous gamma Al_2O_3 membrane with macroporous poly(vinylidene fluoride-co-hexafluoropropylene) (PVDF-HFP) to form a sandwich-type layered structure, which imbibes liquid electrolyte based on 1M LiTFSI/PC. The resultant electrolyte/separators exhibits room temperature ionic conductivity above 10^{-3} S/cm and storage modulus larger than 0.5 GPa.

Nanoporous gamma Al2O3 is prepared by anodic oxidation of metallic aluminum with controllable pore size and interpore distance [1]. Al_2O_3 matrix itself provides good mechanical property while its open porous structure allows ions to pass by but not enough for dendrite to penetrate through. Macroporous PVDF-HFP polymer is conveniently prepared from water-induced phase separation. It has been proved to be able to hold large amount of electrolyte which

offers great conductivity [2]. By combining these two elements, our nanoporous ceramic/polymer composite electrolyte show an attractive combination of good mechanical property and conductivity.

3.2 Experiment Section

Herein we attempted two types of ceramic/polymer composites, the PEG functionalized SiO_2 nanoparticles/PVDF-HFP, and nanoporous Al_2O_3/PVDF-HFP laminated composite.

PEG-SiO_2/PVDF-HFP

PEG functionalized SiO_2 nanoparticles were synthesized based on previously described methods [3]. Briefly, Ludox 30 (supplied by Sigma) was heated to 100 ^oC. Silane was added drop by drop at the molar ratio of 2:1. The reaction was kept at 100 ^oC for 12 hours. The resultant solution was dried in vacuum oven to complete silane reaction, and then the nanoparticles were rigorously washed with chloroform and hexane to remove free PEG chains. The well dispersed PEG-SiO_2 in chloroform was blended with DMF and then evaporated in a rotary evaporator to remove chloroform. To prepare the PVDF-HFP/PEG-SiO_2 solution, a predetermined amount of PVDF-HFP in pellets form was added in the PEG-SiO_2/DMF solution under rigorous stirring. The formed transparent solution was casted on a clan glass slide and the surface flatness and thickness was controlled by a doctor blade technique. Two approaches were adopted to prepare solid membranes: solvent evaporation and phase separation. The former involves evaporating DMF in vacuum oven at 70^oC overnight. The latter requires the solution covered glass plate to be immersed in a water bath at room temperature. To prepare the electrolyte-separator, the composite separator was soaked in 1M lithium bis(trifluoromethanesulfonyl)imide (LiTFSI)/ propylene carbonate (PC) solution for at least 24 hours.

Nanoporous Al_2O_3/PVDF-HFP

Polyvinylidene fluoride hexafluropropylene (PVDF-HFP, supplied by Sigma Aldrich.) was dissolved in N, N-dimethylformamide (DMF, supplied by Sigma Aldrich) at 10 wt% concentration. The viscous solution was poured onto a clean glass plate, covered by nanoporous Al_2O_3 membrane (Whatman Anodisc® 25 with 20 nm, 100 nm, and 200 nm pore sizes, supplied by Fisher). Again, both solvent evaporation and phase separation were used to prepare the composite membranes. The formed solid composite separator was completely dehydrated in vacuum. The same approach was taken to soak the composite separator with liquid electrolyte.

Coin cell assembly

The symmetric lithium coin cells and the Li/LTO coin cells (both 2032 type) were prepared under argon protection (glove box, MBraun. Labmaster). The symmetric lithium/lithium coin cells have Li/(PVDF-HFP/Al_2O_3/LiTFSI/PC)/Li structure, while the Li/LTO coin cells have Li/(PVDF-HFP/Al_2O_3/LiTFSI/PC)/LTO structure. The LTO electrode is composed of 10% PVDF binder, 10% carbon black, and 80% LTO. The LTO electrode was prepared by two methods: solvent casting and mechanical compressing.

Electrode prepared by solvent casting: A small amount of N-methylpyrrolidone (NMP) was used as solvent for homogenizing all components. The resultant slurry was coated on a copper plate and rigorously dried. Because the laminated electrolyte-separators hosts large amounts of liquid electrolyte that wets LTO well, it is assumed that activation of the LTO electrode occurs almost immediately after contacting with the electrolyte-separator and none of the usual electrochemical activation processes were used in the current experiments.

Electrode prepared by mechanical compressing: A predetermined amount of active materials, carbon black and binder were thou roughly mixed in a mortar and then in a ball mill. The

resultant homogeneous black powder was compressed using a hydraulic compressive machine under the pressure of 20000 psi. The formed solid black electrode generally shows the weight of 100-150 mg.

Characterization methods

A thermogravimetric analyzer (TGA) was used to study the thermal stability of PVDF-HFP/100 nm Al_2O_3/LiTFSI/PC and PVDF-HFP/100 nm Al_2O_3/LiTFSI/PEG. Scanning electron microscopy (LEO-1550-FESEM) was used to characterize the laminated structure in the composite separator. The separator was cut in liquid nitrogen to achieve clean edges. The sample was placed vertically on a SEM stub for cross-section observation. The SEM images were obtained under 3 kV voltages with aperture size of 30 μm. Mechanical properties of the separator/electrolyte materials were characterized using dynamic mechanical analysis (DMA-Q800) in the temperature range from -130 ^oC to 150 ^oC. A heating rate of 10 ^oC min-1 and frequency of 1 Hz were employed for these measurements. Atomic force microscopy (AFM, Asylum-MFP-3D-Bio-AFM) was used to indirectly measure the modulus of the unlaminated Al_2O_3 film. The force mode was chosen to obtain the force plot against the indent depth. Conductivity and impedance were measured against frequency using a Novocontrol N40 broadband dielectric spectroscopy at different temperature from -5 ^oC to 100 ^oC. The lithium plate/strip experiment and galvanostatic charge/discharge experiment were performed on a Neware CT-3008 battery tester. The plate-strip experiment was performed with symmetric lithium coin cells under different current density (0.02, 0.05, 0.1, and 0.2 mA cm^{-2}). The coin cells harvested after the plate-strip experiment were taken apart in a glove box and the separator/electrolytes dried in the vacuum chamber of the glove box and stored for SEM

analysis. The galvanostatic experiment was performed under different charging/discharging rate (0.315, 0.630, and 1.575 mA cm^{-2}, which corresponds to 1C, 2C and 5C, respectively).

3.3 Result and discussion

Firstly we observed the surface morphology of PEG-SiO_2/PVDF-HFP membrane and nanoprous Al_2O_3/PVDF-HFP membranes, as shown in **Figure** 3.1. PEG-SiO_2/PVDF-HFP made by solvent evaporation and Al_2O_3/PVDF-HFP made by both solvent evaporation and phase separation method show smooth surface (**Figure** 3.1a, b, c). However, The PEG-SiO_2/PVDF-HFP membranes prepared by phase separation present uneven and rough surface pattern (**Figure** 3.1d), which might be due to the coagulation of nanoparticles during the formation of the membranes. It is also highly likely that the nanoparticles might migrate freely during water bath which creates voids in the PVDF-HFP. After being immersed in 1M LiTFSI/PC, the AC conductivity of all four types of composite membranes with various compositions are measured from -5^{o}C to 100^{o}C (**Figure** 3.2). The DC conductivity is determined from AC measurements by fitting into the power law proposed by Jonscher [4]. A typical AC conductivity vs. frequency profile is provided as **Figure** 3.4c in which the plateau regions roughly represent the DC ionic conductivity. The conductivity versus temperature are shown in figure xxx and the solid lines are the fitting based on Arrehnius equation. It is clear that the membranes prepared by phase separation methods provide the highest DC ionic conductivity (**Table** 3.1). Considering the strong nanoparticles coagulation happens in PVDF-HFP and the potential nanoparticle loss during the preparation process. We have decided that the nanoporous Al_2O_3/PVDF-HFP membranes are better candidates as separators for LMBs.

a)  b)  c) 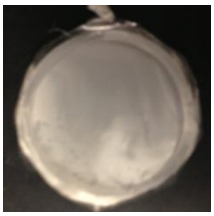 d) 

Figure 3.1 The surface morphology of a) PEG-SiO_2/PVDF-HFP made by solvent evaporation; b) PEG-SiO_2/PVDF-HFP made by water induced phase separation; c) Al_2O_3/PVDF-HFP made by solvent evaporation; d) Al_2O_3/PVDF-HFP made by water induced phase separation.

#	Description	Liquid uptake	Ea(eV)	Conductivity @ 25℃
1	20% Nanoparticles-PVDF evaporation	104%	0.27	3.25E-5 S/cm
2	20% Nanoparticles-PVDF phase separation	754%	0.17	1.93E-3 S/cm
3	30% Nanoparticles-PVDF evaporation	131%	0.28	9.74E-5 S/cm
4	50% Nanoparticles-PVDF evaporation	98%	0.28	9.21E-5 S/cm
5	20% PEG-lithium(50/50) NP PVDF evaporation	53%	0.35	2.35E-5 S/cm
6	PVDF-Al2O3 20nm evaporation	67%	0.38	2.02E-5 S/cm
7	PVDF-glycerol Al2O3 20nm evaporation	97%	0.19	1.05E-4 S/cm
8	PVDF-glycerol-Al2O3-PEG 20nm evaporation	106%	0.23	2.66E-4 S/cm
9	PVDF-glycerol-Al2O3-PEG 100nm evaporation	84%	0.20	2.90E-4 S/cm
10	PVDF-HFP-Al2O3-PEG 20nm evaporation	109%	0.24	9.60E-5 S/cm
11	PVDF-HFP-Al2O3 100nm phase separation	489%	0.25	1.51E-3 S/cm
12	1M LiTFSI/PC	N/A	0.14	5.68E-3 S/cm

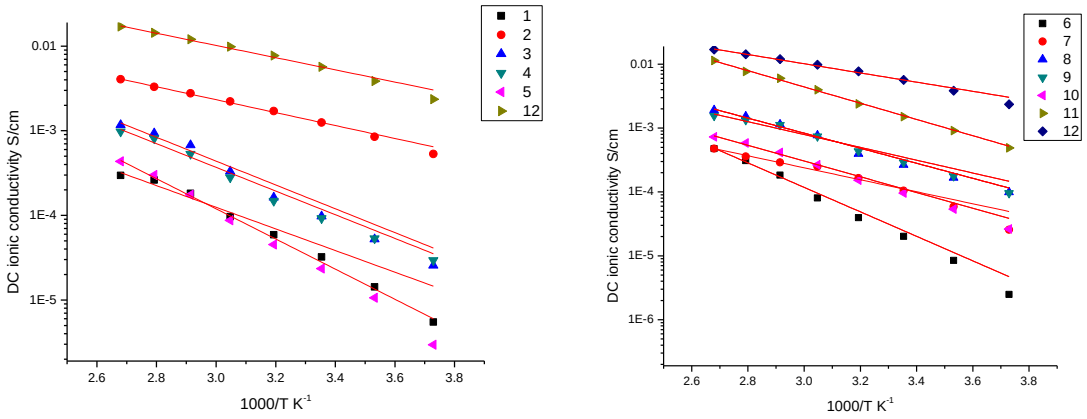

Table 3.1. DC ionic conductivity of various combinations of ceramic/polymer separator electrolyte. **Figure** 3.2. DC ionic conductivity of those at a range of temperature from -5 ºC to 100ºC. The solid lines represent Arrhenius fit.

The surface morphology of pristine Al_2O_3 with different pore sizes ranging from 20 nm to 200 nm was observed by SEM as shown in **Figure** 3.3a. The pores present regular size and uniform distribution. Such structure is further confirmed by AFM (**Figure** 3.3b). High porosity fulfills the Al_2O_3 membranes with great ion transport ability, but strongly jeopardizes its roughness which makes them as brittle as glass slides. After lamination, the materials possess a tri-layer structure with Al_2O_3 membrane in the middle and two PVDF-HFP layers on the top and at the bottom respectively, which is shown in the cross-section pictures as **Figure** 3.4. It is observed that the pores are still independent without being filled by polymers and the boundary between the ceramic and the polymer deforms the shape of pores near the edge. In contrary to the pristine Al_2O_3 membranes that are too brittle to handle, laminated composite shows a much better toughness provided by the macroporous PVDF-HFP formed after a phase separation process.

a)

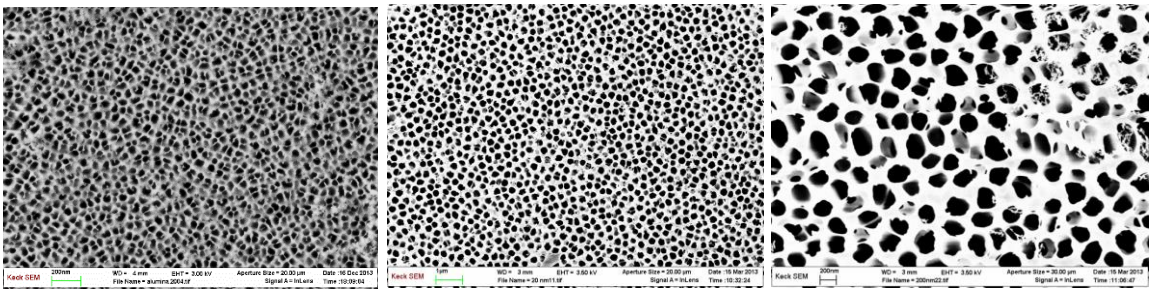

b)

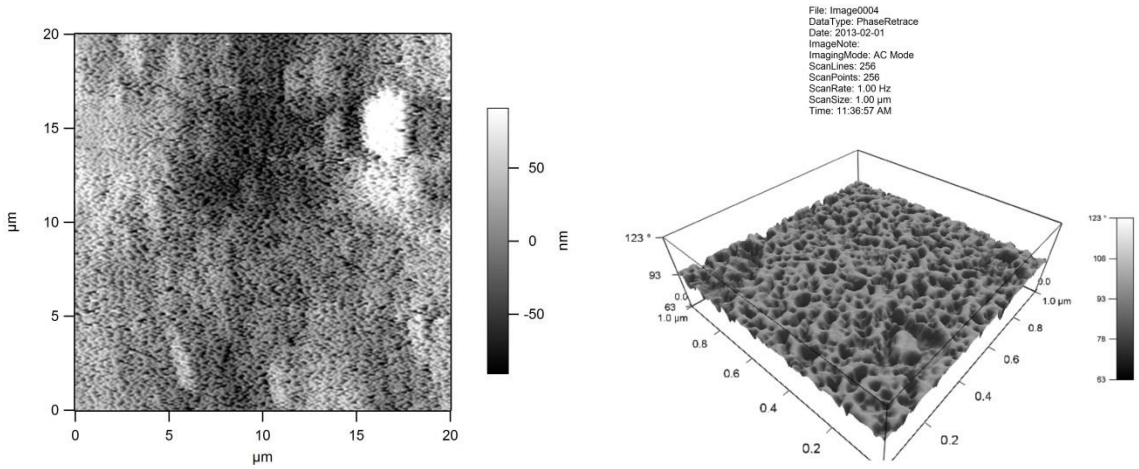

Figure 3.3 a) SEM pictures of nanoporous Al_2O_3 with 20nm (left), 100nm (middle), and 200nm (right); b) AFM surface topography of nanoporous Al_2O_3 with 20nm pores.

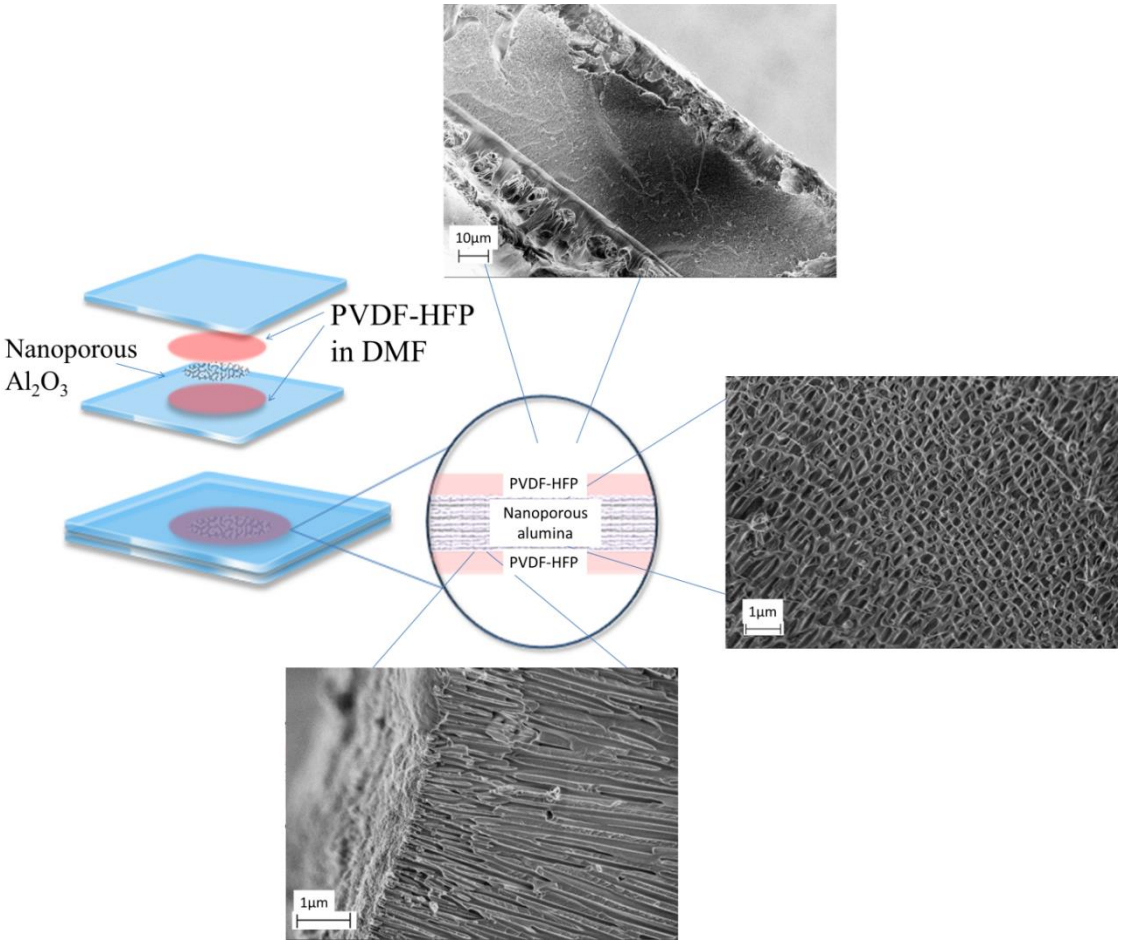

Figure 3.4 Middle and left: Schematic of the structure and preparation method of PVDF-HFP/Al_2O_3 separator. SEM pictures of the PVDF-HFP/Al_2O_3 with 100 nm nanopores: top, cross-section of the composite; right, cross-section of the internal alumina layer; bottom, boundary between alumina and polymer.

After immersing the composite membrane in 1M LiTFSI/PC overnight, the membrane saturates with large amount of liquid electrolyte and shows high ionic conductivity. **Figure** 3.5a shows the TGA data for PVDF-HFP/Al_2O_3/LiTFSI/PC and PVDF-HFP/Al_2O_3/LiTFSI/PEG electrolyte. The mass drop is mainly due to the decomposition of PC and PEG later, indicating that the composite separators are able to absorb lots of electrolyte. **Figure** 3.5b reports the DC ionic conductivity of PVDF-HFP/Al_2O_3/LiTFSI/PC electrolyte-separator with different nano-pore sizes at temperatures ranging from -5 ^oC to 100 ^oC. The conductivity of PVDF-HFP/Al_2O_3/LiTFSI/PC electrolytes with different pore sizes are close to 1×10^{-3} S cm^{-1} at room temperature, which is similar to that of the LiTFSI/PC liquid electrolyte. Such high conductivity is attributed to the unrestricted movement of LiTFSI in liquid PC hosted in the pores of the separator. The solid lines through the data are fitted using the Arrhenius equation $\sigma=Ae^{(-Ea/RT)}$. The deviations between fitting and experimental data in the low temperature region are attributed to the broad glass transition temperature of PVDF-HFP. The activation energy obtained from the fits is provided in **Table** 3.2. The activation energy values are evidently all close to consensus values for LiTFSI/PC, implying that for the pore dimensions studied, the pores are large enough for LiTFSI to transport without encountering great energy barriers.

a)

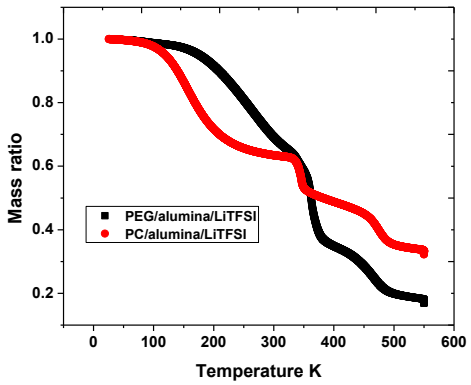

b)

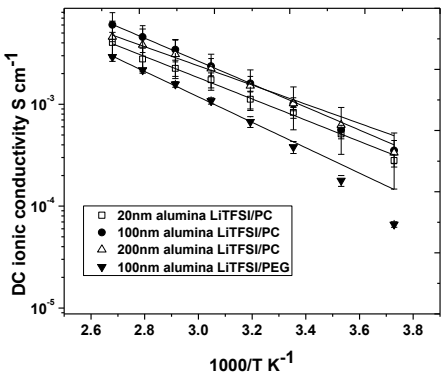

c)

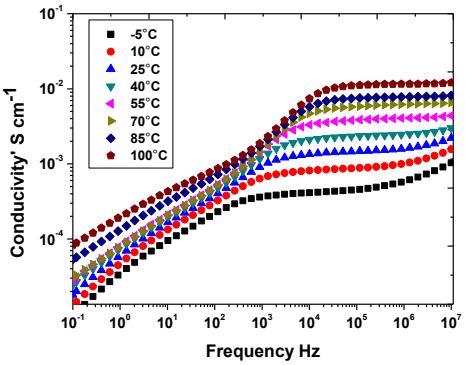

Sample description #	Conductivity at 25℃ [S cm^{-1}]	Activation Energy Ea [eV]
20 nm Al_2O_3/LiTFSI/PC	8.30E-4	0.20674 ± 0.00968
100 nm Al_2O_3/LiTFSI/PC	1.01E-3	0.22375 ± 0.00684
200 nm Al_2O_3/LiTFSI/PC	1.07E-3	0.18680 ± 0.00712
100 nm Al_2O_3/LiTFSI/PEG	3.80E-4	0.24762 ± 0.01585

Figure 3.5 a) TGA profiles for 100 nm Al_2O_3/LiTFSI/PC and 100nm Al_2O_3/LiTFSI/PEG from room temperature up to 550℃; b) DC ionic conductivity of PVDF-HFP/Al_2O_3 separators with various pore sizes after immersing in LiTFSI/PC and separators with 100 nm pores after immersion in LiTFSI/PEG; c) A typical plot of conductivity data against frequency at various temperatures; **Table** 3.2 DC ionic conductivity of each system in Figure S5 at room temperature, and activation energy derived from Arrhenius fits.

The shear mechanical modulus is both intuitively and based on theory considered an important physical property for assessing the ability of an electrolyte/separator to impede lithium dendrite growth in a LMB. Because of its brittleness, the mechanical modulus of the unlaminated nanoporous Al_2O_3 cannot be characterized using normal mechanical testing methods. We instead employ an atomic force microscopy (AFM) approach to first obtain a load-displacement curve, and by applying Oliver and Pharr's method [5], subsequently deduce the reduced elastic modulus to be around 500 MPa (**Figure** 3.6b, c). This value is substantially lower than the theoretical modulus for bulk Al_2O_3 and somewhat lower than expected even if one factors in the nanoporous nature of the material [6]. It suggests that even the very small strains applied in the AFM measurement may cause some amount of brittle failure of the unlaminated material. This situation is quite different for the PVDF-HFP/Al_2O_3 composite film, which can be subjected to orders of magnitude larger mechanical deformations without showing any evidence of mechanical failure. **Figure** 3.6a reports the elastic/storage modulus of PVDF-HFP/Al_2O_3 separator film measured using dynamical mechanical analysis of a bulk specimen over a broad range of temperature (-130 ^oC to 150 ^oC). The pore size of the Al_2O_3 is varied from 20 nm to 200 nm and the figure also presents data for the macroporous PVDF-HFP copolymer film without the nanoporous Al_2O_3 interlayer, for comparison. It is apparent that irrespective of the measurement temperature, the elastic modulus for the PVDF-HFP/Al_2O_3 is about one order of magnitude higher than that of the PVDF-HFP and exhibits at most a weak dependence on the nanopore dimensions. At room temperature, the elastic modulus is close to 0.4 GPa for the composite material with the largest Al2O3 pore dimension. In every case, the elastic modulus decreases gradually with increasing temperature, which is attributed to the broad glass transition region for the highly random PVDF-HFP copolymer [7]. After soaking the PVDF-HFP/Al_2O_3 separators in

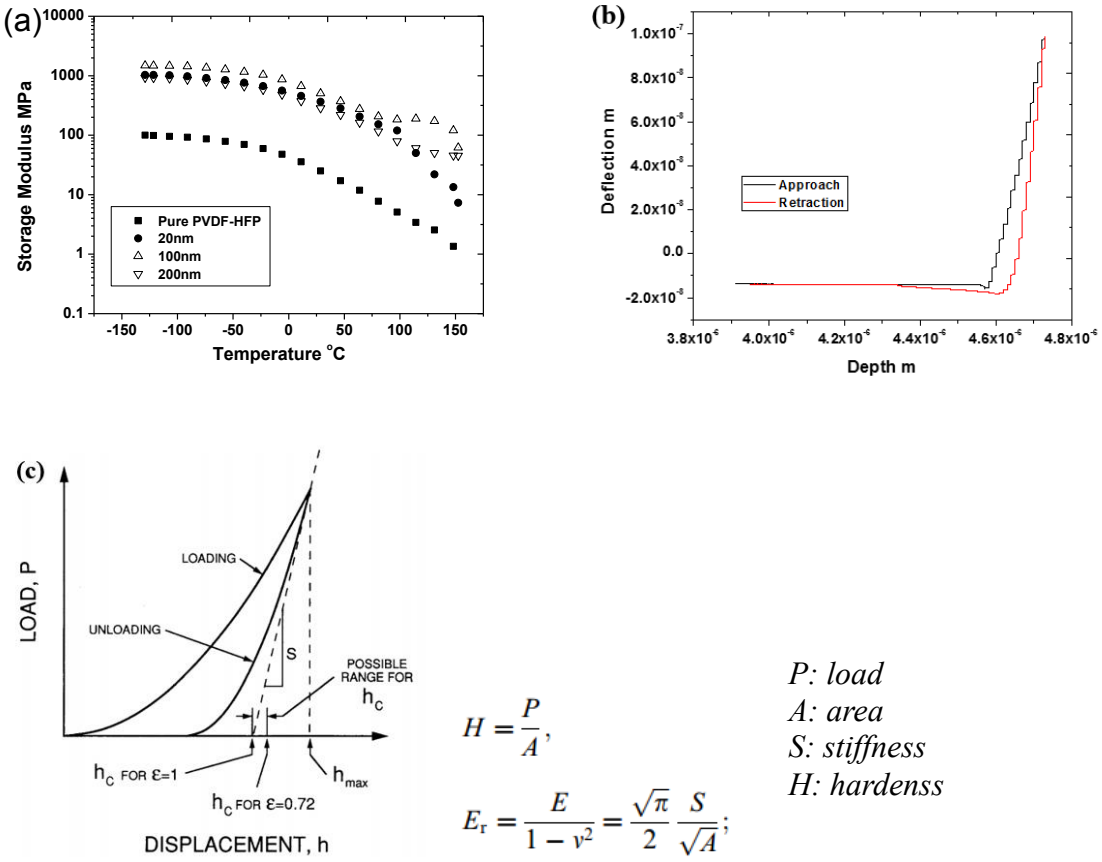

$$H = \frac{P}{A},$$

$$E_r = \frac{E}{1-\nu^2} = \frac{\sqrt{\pi}}{2}\frac{S}{\sqrt{A}};$$

P: load
A: area
S: stiffness
H: hardenss

Figure 3.6 a) Storage modulus of PVDF-HFP/Al_2O_3 separators with various pore sizes and pure PVDF-HFP as a function of temperature. b) A typical load-depth plot measured by AFM. c) Method used for calculating reduced elastic modulus. Adapted with permisson [5] Copyright (1992), Materials Science Society.

a 1M LiTFSI/PC electrolyte the materials become even tougher, but slippery, which makes it difficult to measure their mechanical modulus. Based on several repeat experiments we conclude that the storage modulus of a composite film based on Al_2O_3 is at least 0.15 GPa.

In addition to facilitating good ion transport in bulk, a suitable electrolyte for a LMB must also present low barriers for injection and removal of Li ions at the electrode/electrolyte interface. **Figure** 3.7(left) reports impedance spectra of a PVDF-HFP/Al_2O_3/LiTFSI/PC material based on Al_2O_3 with 100 nm nanopores measured in a symmetric lithium coin cell as a function of temperature. By fitting the results to the equivalent circuit model depicted in the inset to **Figure** 3.7(right), both the bulk and interfacial resistance can be obtained (Table S2). It is apparent that both the interfacial and bulk resistances at 25 ^oC are low (48.8 Ω and 31.9 Ω, respectively) and as expected decrease with increasing temperature. The higher interfacial resistance compared with the bulk resistance shows that the main obstacle for ion conduction is the interfacial diffusion. The corresponding room-temperature bulk and interfacial resistances for the electrolyte-separators based on Al_2O_3 with 20 nm and 200 nm nanopores are, respectively, 9.5 Ω, 51.2 Ω, 60.6 Ω and 82.0 Ω. (see **Figure** 3.7 and **Table** 3.3). It means that for the range of pore dimensions studied, the materials are good candidates for application in batteries.

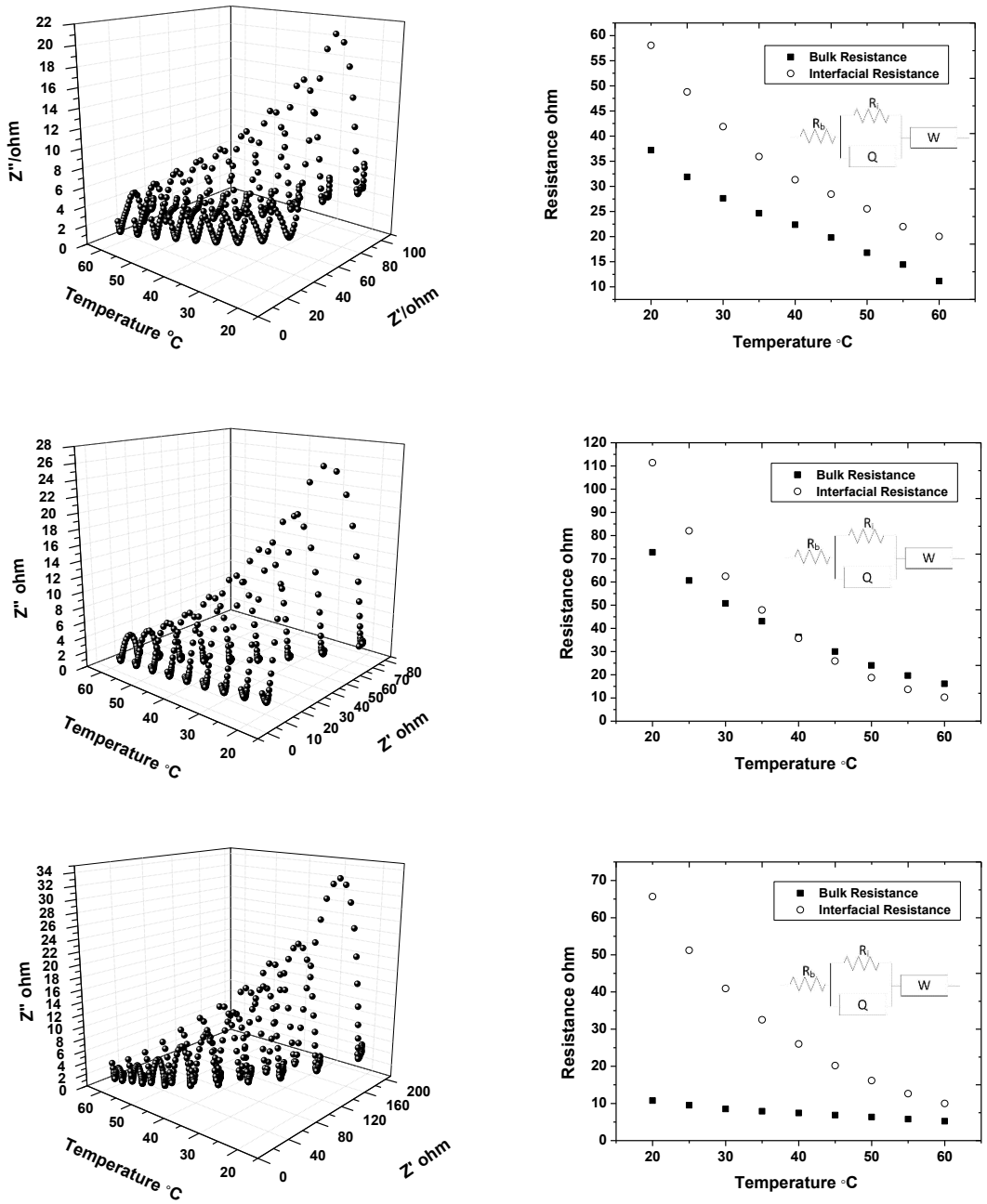

Figure 3.7 Left: Impedance spectra of PVDF-HFP/Al_2O_3/LiTFSI/PC against temperature. The pore sizes of alumina are 100, 20, 200 nm respectively. Right: Bulk resistance and interfacial resistance of the composite in 'left' against temperature, analyzed using the equivalent circuit as inset.

Temperature ℃	Bulk Resistance	Interfacial Resistance	Bulk Resistance	Interfacial Resistance	Bulk Resistance	Interfacial Resistance
	20 nm [ohm]		100 nm [ohm]		200 nm [ohm]	
20	10.77 ±0.28	65.69 ±1.85	37.20 ±0.75	58.03 ±1.46	72.78 ±0.83	111.40 ±1.34
25	9.49 ±0.24	51.20 ±1.38	31.88 ±0.69	48.78 ±1.29	60.60 ±0.66	82.00 ±0.92
30	8.52 ±0.20	40.94 ±1.05	27.63 ±0.57	41.86 ±1.02	50.77 ±0.49	62.40 ±0.68
35	7.91 ±0.18	32.52 ±0.79	24.64 ±0.50	35.93 ±0.83	43.09 ±0.40	47.90 ±0.54
40	7.41 ±0.15	26.01 ±0.60	22.35 ±0.45	31.32 ±0.72	36.28 ±0.39	35.70 ±0.50
45	6.87 ±0.13	20.18 ±0.45	19.83 ±0.50	28.43 ±0.74	30.00 ±0.39	25.93 ±0.46
50	6.32 ±0.12	16.14 ±0.36	16.79 ±1.82	25.52 ±2.24	24.05 ±0.21	18.75 ±0.27
55	5.75 ±0.11	12.65 ±0.28	14.44 ±0.92	21.99 ±1.14	19.64 ±0.18	13.69 ±0.22
60	5.21 ±0.10	10.00 ±0.22	11.17 ±1.41	20.04 ±1.60	16.11 ±0.16	10.29 ±0.20

Table 3.3 Bulk and interfacial resistance for composites with various pore diameters.

To assess the stability of our PVDF-HFP/Al_2O_3/LiTFSI/PC electrolyte-separators in batteries employing metallic lithium anodes, we performed electrochemical cycling of a Li/$Li_4Ti_5O_{12}$(LTO) cell utilizing a laminated material based on Al_2O_3 with 100 nm pores as both the separator and electrolyte. This cell configuration was chosen because of the well-known, stable electrochemical cycling of Li/LTO cells in conventional electrolytes at both low and high rates. It therefore allows the new separator/electrolyte materials to be evaluated at high current densities and over large numbers of charge-discharge cycles to establish their performance limits [8].

Figure 3.8a and 3.8b report the capacity and Coulombic efficiency as a function of cycle number at a fixed current density of 0.315 mA cm^{-2} (1C) and 1.575 mA cm^{-2} (5C). The experiment is also taken at 0.630 mA cm^{-2} (2C) (Figure S9). It is apparent from this figure that apart from a small amount of capacity fading over the first few cycles, the cells exhibit stable, high-efficiency cycling over at least 1100 charge/discharge cycles, with no evidence of short circuiting and with a capacity approaching the theoretical maximum (175 mAh g^{-1}) for LTO. Scrutiny of **Figure** 3.8a and 3.8b shows that the initial capacity fading is accompanied by as rapid a decrease of the Columbic efficiency from above 100% to stable values close to 100% for more than 1000 cycles. We therefore attribute the initial fading and the excess discharge to electrolyte decomposition and formation of the solid electrolyte interface during the first few cycles, as well as to unwanted side reactions, which further cause electrolyte decomposition [9]. **Figure** 3.8c and 3.8d report the galvanostatic charge-discharge profiles after the 1st, 100th, and 1000th cycles at a fixed current density of 0.315 mA cm^{-2} (1C) and 1.575 mA cm^{-2} (5C). It is apparent that the voltage plateau, round-trip efficiency, and capacity retention are all quite high.

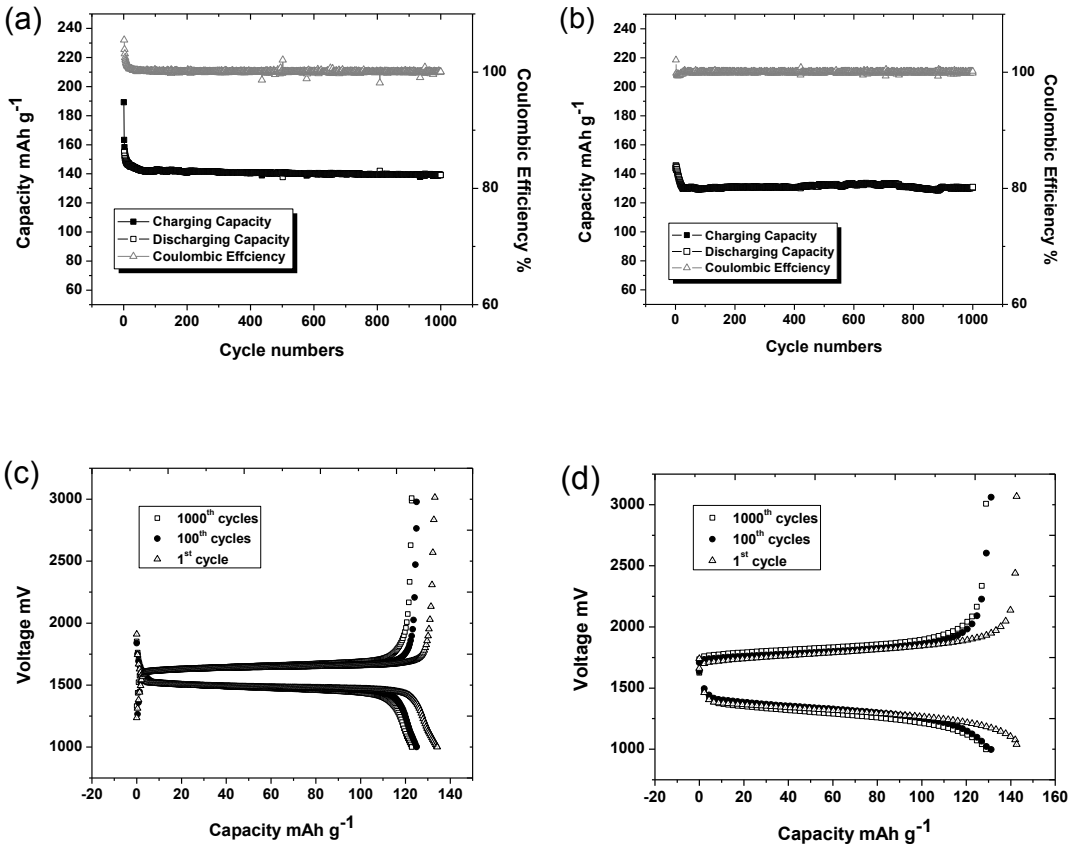

Figure 3.8. Galvanostatic charging/discharging plots for Li/(PVDF-HFP/100 nm Al_2O_3/LiTFSI/PC)/LTO cells under: (a) 0.315 mA cm^{-2} (1C) and (b) 1.575 mA cm^{-2} (5C). Discharge and charge voltage profiles versus capacity for 1st, 100th, and 1000th cycle for (c) 0.315 mA cm^{-2} (1C); (d) 1.575 mA cm^{-2} (5C).

To further evaluate the performance of the PVDF-HFP/Al_2O_3/LiTFSI/PC electrolyte in LMBs, we employed a cyclic lithium plate/strip electrochemical procedure in a symmetric lithium cell to characterize performance over extended periods of time. Because the capacity of the cathode/anode is not limited by the finite capacity of the LTO host used for the experiments reported in **Figure** 3.9, much larger amounts of lithium can be moved between electrodes within each cycle, which increases the chances of cell failure by dendrite-induced short circuits. In the present experiments a fixed protocol was used wherein cells were periodically charged for 3 hours and discharged for 3 hours at a range of current densities. Formation of a short circuit in this configuration produces an internal path for current flow in the electrolyte, which lowers the internal resistance and causes the measured voltage to drop. Thus, by monitoring the voltage versus time during these strip/plate cyclic experiments, it is possible to identify the onset of short-circuiting from the voltage drop. **Figure** 3.9a depicts the time-dependent voltage profile for a cell based on the electrolyte-separators containing Al_2O_3 with 100 nm pores, cycled for up to 1000 hours under a constant current density of 0.2 mA cm^{-2}. **Figure** 3.9b reports results from similar measurements, except without the nanoporous Al_2O_3 layer in the separator. The sudden drop observed in the peak-to-peak voltage amplitude in Figure 4b is attributed to cell failure by dendrite-induced short circuits. A variety of hypotheses have been presented in the literature for why these dendrites form [10-14], and proliferate to the point that they lead to cell failure [15, 16]. Although these results shed no new light on the dendrite nucleation processes, they clearly show that the pore configuration and mechanics of the electrolytes-separators employed are important impediments to dendrite proliferation. In particular, it is seen that while cells based on

the PVDF-HFP/LiTFSI/PC fail by short circuiting after as little as 60 hours of operation at 0.2 mA cm^{-2}, cells based on the PVDF-HFP/Al_2O_3/LiTFSI/PC electrolyte exhibit stable voltage profiles even after 1000 hours of operation. Considering the modulus of PVDF-HFP/Al_2O_3 is almost ten times higher than that of PVDF-HFP itself, this result is consistent with Monroe and Newman's analysis. Results from similar measurements using PVDF-HFP/Al_2O_3/LiTFSI/PC electrolyte-separators at both lower and higher current densities are provided in the supporting materials section (**Figure** 3.9c, d). It is apparent from these experiments that the materials are quite effective in stabilizing the cells against failure by short circuiting.

We further have conducted a long term electrodeposition experiment using LTO/Li battery to confirm the dendrite prevention ability of Al_2O_3/PVDF-HFP separator-electrolyte. A thick LTO electrode (100-150 mg) prepared by mechanical compressing was used as cathode and such large weight ensure the electrodeposition of lithium can last for several days even at high current density. The assembled coin cells have been cycled from 1V to 3V under the current density of 0.2 mA/cm2. The voltage profiles of the experiments are shown in figure xxx, in which over 1000 hours the battery operation is considered stable and no short circuit is recognized. It proves that the Al_2O_3/PVDF-HFP separator-electrolyte not only effectively avoid dendrite caused short circuit in symmetric modeling coin cells, but also in a real functional battery as LTO/Li battery.

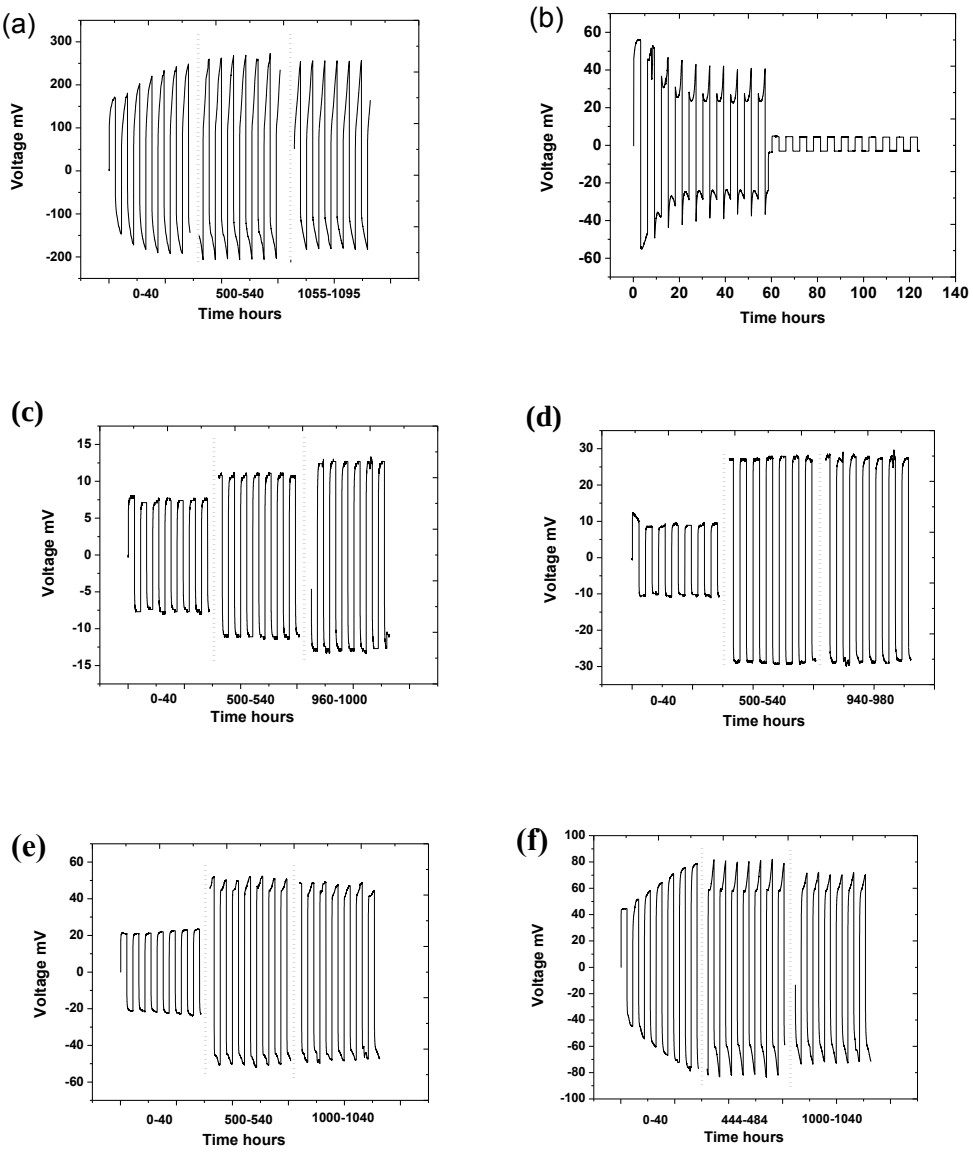

Figure 3.9 Voltage profiles for lithium plating/striping experiment as a function of time for symmetric lithium coin cell cycled at a fixed current density of 0.2 mA cm^{-2} using: (a) PVDF-HFP/100 nm Al_2O_3/LITFSI/PC and (b) PVDF-HFP/LiTFSI/PC as separators/electrolytes. Voltage profiles for lithium plating/striping experiment as a function of time for symmetric lithium coin cell with PVDF-HFP/100 nm Al_2O_3/LiTFSI/PC under (c) 0.02 mA cm^{-2}; (d) 0.05 mA cm^{-2}; (e) 0.1 mA cm^{-2}; (f) 0.2 mA cm^{-2}

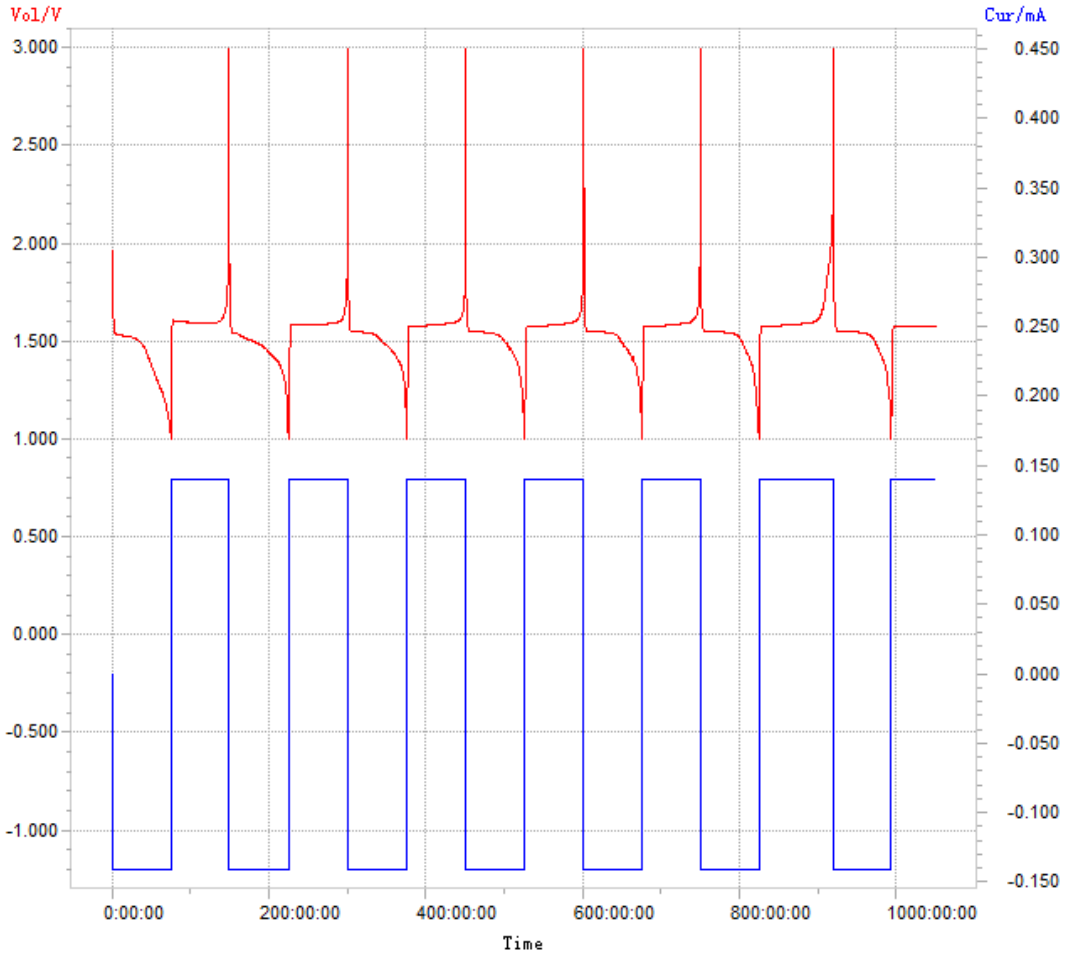

Figure 3.10. Voltage profile of thick LTO/Li battery with PVDF-HFP/100 nm Al_2O_3/LITFSI/PC separator electrolyte charged/discharged at 0.2 mA cm^{-2} from 1V to 3V

After running the lithium plating/striping experiment for over 1000 hours, some of the coin cells have been disassembled in the glove box and rigorously dried in the affiliate vacuum chamber. **Figure** 3.11 shows the SEM images of the separator-electrolyte after lithium plating/striping experiment. And figure S12 reports the following X-ray diffraction (XRD) study of the previously described separator-electrolyte and pristine Al_2O_3.

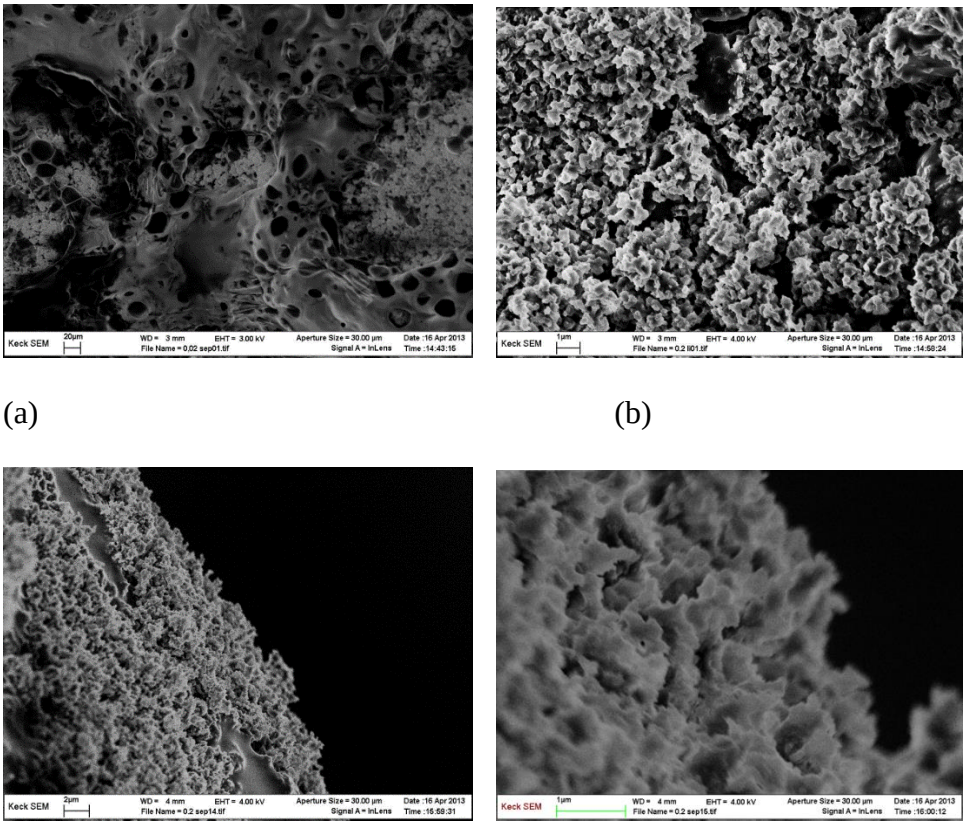

(a) (b)

(c) (d)

Figure 3.11. (a) and (b) SEM images of the center of the separator after lithium plating/striping experiment. The lithium dendrite covers the surface of separator while not penetrates it. (c) and (d) SEM images of the edge of the separator, showing that some dendrite might grow passing the edge of the separator.

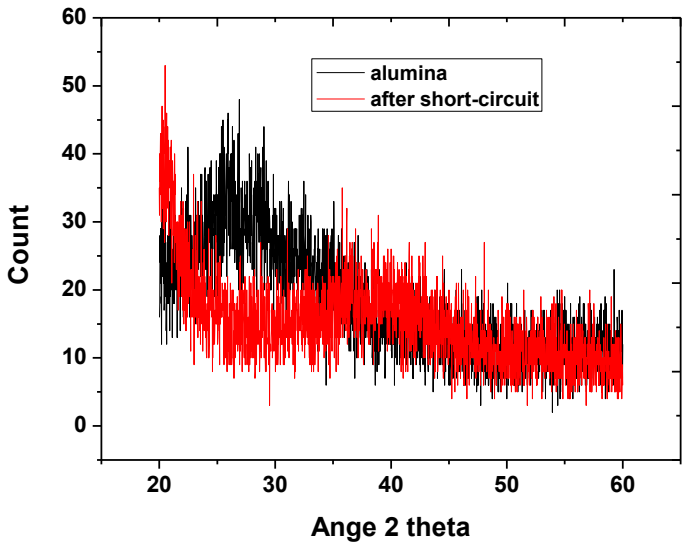

Figure S12. XRD curve of PVDF-HFP/100 nm Al_2O_3/LiTFSI/PC after lithium plating/striping experiment and pristine 100 nm Al_2O_3. However, due to the noise caused by amorphous polymer and Al2O3, no recognizable signals can be observed.

Reference

1. Diggle, J.W., T.C. Downie, and C.W. Goulding, *Anodic Oxide Films on Aluminum.* Chemical Reviews, 1969. **69**(3): p. 365-&.

2. Du Pasquier, A., et al., *Plastic PVDF-HFP electrolyte laminates prepared by a phase-inversion process.* Solid State Ionics, 2000. **135**(1): p. 249-257.

3. Nugent, J.L., S.S. Moganty, and L.A. Archer, *Nanoscale organic hybrid electrolytes.* Advanced Materials, 2010. **22**(33): p. 3677-3680.

4. Ngai, K.L., A.K. Jonscher, and C.T. White, *Origin of the Universal Dielectric Response in Condensed Matter.* Nature, 1979. **277**(5693): p. 185-189.

5. Oliver, W.C. and G.M. Pharr, *An Improved Technique for Determining Hardness and Elastic-Modulus Using Load and Displacement Sensing Indentation Experiments.* Journal of Materials Research, 1992. **7**(6): p. 1564-1583.

6. Xia, Z., et al., *Mechanical properties of highly ordered nanoporous anodic alumina membranes.* Reviews on Advanced Materials Science, 2004. **6**(2): p. 131-139.

7. Abbrent, S., et al., *Crystallinity and morphology of PVdF–HFP-based gel electrolytes.* Polymer, 2001. **42**(4): p. 1407-1416.

8. Armstrong, G., et al., *TiO2(B) nanowires as an improved anode material for lithium-ion batteries containing LiFePO4 or LiNi0.5Mn1.5O4 cathodes and a polymer electrolyte.* Advanced Materials, 2006. **18**(19): p. 2597-+.

9. Arora, P., R.E. White, and M. Doyle, *Capacity Fade Mechanisms and Side Reactions in Lithium-Ion Batteries.* Journal of the Electrochemical Society, 1998. **145**(10): p. 3647-3667.

10. Brissot, C., et al., *In situ study of dendritic growth in lithium/PEO-salt/lithium cells.* Electrochimica Acta, 1998. **43**(10-11): p. 1569-1574.

11. Chazalviel, J.N., *Electrochemical Aspects of the Generation of Ramified Metallic Electrodeposits.* Physical Review A, 1990. **42**(12): p. 7355-7367.

12. Rosso, M., et al., *Dendrite short-circuit and fuse effect on Li/polymer/Li cells.* Electrochimica Acta, 2006. **51**(25): p. 5334-5340.

13. Dolle, M., et al., *Live scanning electron microscope observations of dendritic growth in lithium/polymer cells.* Electrochemical and Solid State Letters, 2002. **5**(12): p. A286-A289.

14. Stone, G.M., et al., *Resolution of the Modulus versus Adhesion Dilemma in Solid Polymer Electrolytes for Rechargeable Lithium Metal Batteries.* Journal of the Electrochemical Society, 2012. **159**(3): p. A222-A227.

15. Monroe, C. and J. Newman, *The impact of elastic deformation on deposition kinetics at lithium/polymer interfaces.* Journal of the Electrochemical Society, 2005. **152**(2): p. A396-A404.

16. Brissot, C., et al., *Dendritic growth mechanisms in lithium/polymer cells.* Journal of Power Sources, 1999. **81**: p. 925-929.

Chapter 4

OTHER CERAMICS/POLYMER LAMINATES AS SEPARATOR/ELECTROLYTE FOR LTIHIUM METAL BATTERIRES

4.1 Introduction

The success of nanoporous alumina based laminated separator/electrolyte inspires us to study other ceramics as electrolyte/separator with high conductivity and high modulus. However, as introduced in chapter 2, most applicable ceramic electrolytes show insufficient conductivity at room temperature. Thus we consider to laminate lithium conductive ceramics with liquid-electrolyte-soaked polymer, expecting the composite to exhibit educed interfacial impedance and thus an improved overall conductivity. In parallel, it is realized that nano-porosity is the key factor for high conductivity of laminated ceramic/polymer composites. We have investigated the electrochemical properties of nanoporous silica based electrolyte that shows open structure akin to nanoporous alumina.

We receive lithium conductive glass (brand name LICGC) from Ohara Inc. LICGC material exhibits chemical composition of $Li_{1+x+y}Al_x(Ti,Ge)_{2-x}Si_yP_{3-y}O_{12}$ and a crystal structure similar to the NASICON. It shows an ionic conductivity of 10^{-4} S/cm at room temperature. Nanoporous silica membranes are generously provided by Corning Corp. They are prepared by sintering silica nanoparticles near the melting temperature, at which the surface of nanoparticle is partially melted and then the particles fuse to form a solid membrane after cooling to lower temperature. The resultant membrane exhibits interconnected porosity as well as satisfactory toughness. The advantages of nanoporous silica membranes are three-folded: 1) the preparation process is simple and economic; 2) it exhibits good mechanical properties; 3) the silica shows great chemical flexibility to be functionalized with various ligands. In this section we report preliminary study of the

lithium conductive ceramic and nanoporous silica membrane as separator/electrolyte in LMB.

4.2 Experimental Section

The LICGC conductive ceramic and silica membranes were used as received. They were laminated with PVDF-HFP using the same preparation and characterization methods presented in Chapter 3. The symmetric lithium coin cell and lithium half cells were assembled for conductivity/impedance measurements, polarization test, lithium plating striping test and galvanostatic cycling test. Cells were disassembled after the tests and the lithium metal electrodes were harvested for SEM and EDAX analysis.

Since the silica membranes are thicker than the alumina ones shown in Chapter 3, which will be incompatible with the size of CR2032 coin cells, we used lithium foils that are only 0.35 mm thick instead of the 0.7 mm lithium foil used previously. Even though the thickness of lithium decreases, the number of lithium ions are still sufficient for most of our electrochemical experiments, meaning lithium starvation is unlikely. We have improved the cell configuration by using two lithium foils with different sizes as electrodes in symmetric lithium batteries, which is shown in **Figure** 4.1. Such a cell configuration avoids the potential breaking of silica membranes that could happen during cell assembly, especially when a crimper is employed to close the cell which applies large compressive stress , that may damage the brittle ceramics on edge, compromising its uniformity.

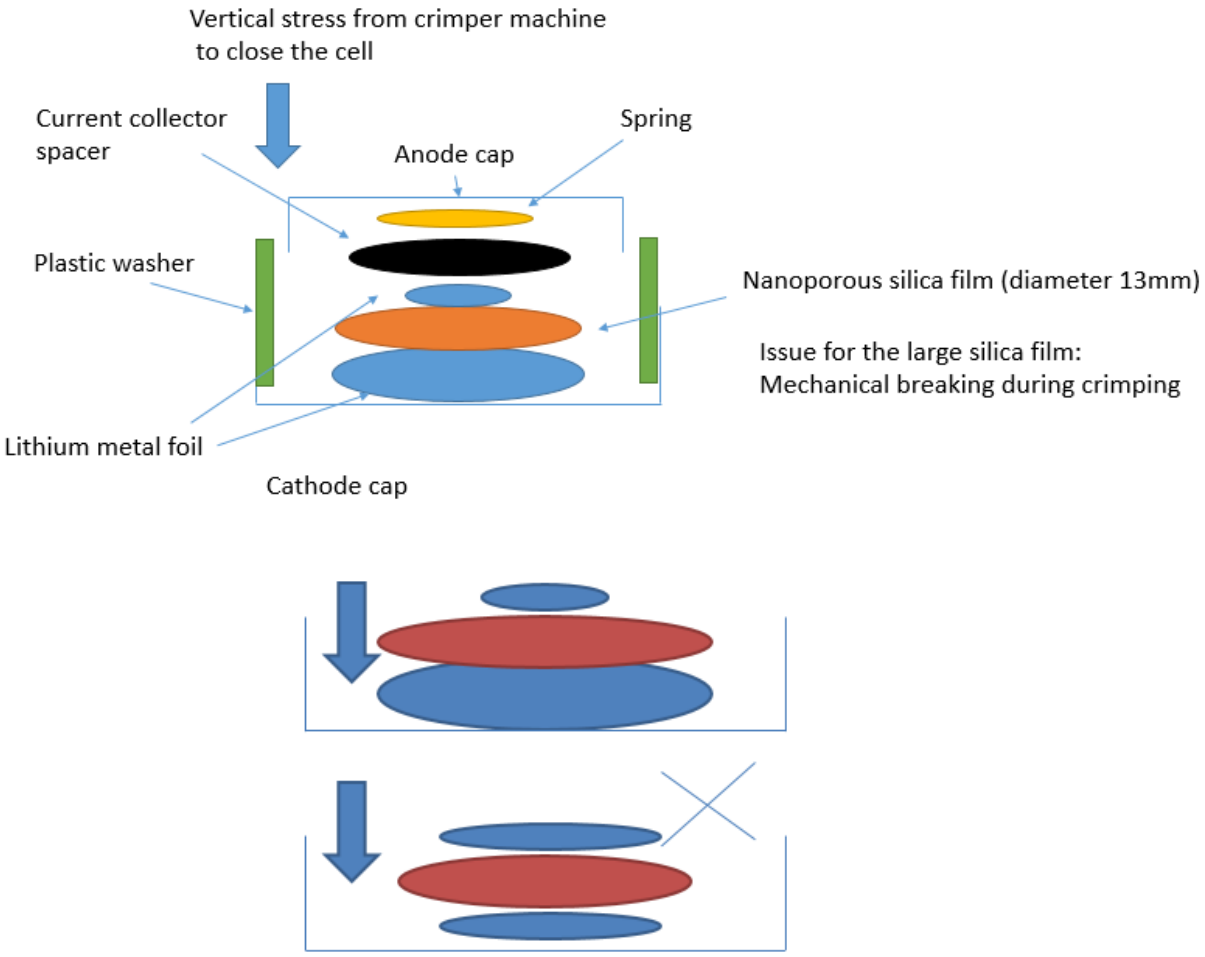

Figure 4.1. The schematic description of coin cell configuration

4.3 Result and discussion

Lithium conductive ceramic LIC-GC based electrolyte

Figure 4.2a shows the DC ionic conductivity of LICGC membrane against temperature compared with other lithium conductive ceramics. The data is provided by Ohara. It is clear that LIC-GC membranes outperform the majority of applicable lithium conductive ceramics, especially exhibiting high conductivity of 10^{-4} S cm^{-1} at room temperature. **Figure** 4.2b reports the impedance spectra of LICGC membrane, which presents a bulk resistance of the membrane around 100 ohm and an interfacial resistance close to 300 ohms. A straight line after 58 kHz indicates a diffusion controlled behavior at low frequency.

We have attempted to laminate LICGC membrane with PVDF-HFP based on the phase separation approach described in chapter 3. Considering that the LICGC is lithium conductive, the membranes are soaked with pure PC instead of LiTFSI/PC. The resultant membranes have been used as separators in symmetric lithium batteries. **Figure** 4.3b presents the extrapolated DC ionic conductivity versus temperature of the LICGC/PVDF-HFP/PC. At room temperature, the LICGC/PVDF-HFP/PC shows a high frequency conductivity at 10^{-4} S cm^{-1}, and a DC ionic conductivity at 2×10^{-5} S cm^{-1}. Two conductivity plateaus can be observed at low temperature when the frequency is below 10^5 Hz, whose appearance is likely due to the formation of two interfaces. The two plateaus gradually immerge into one with the increasing temperature.

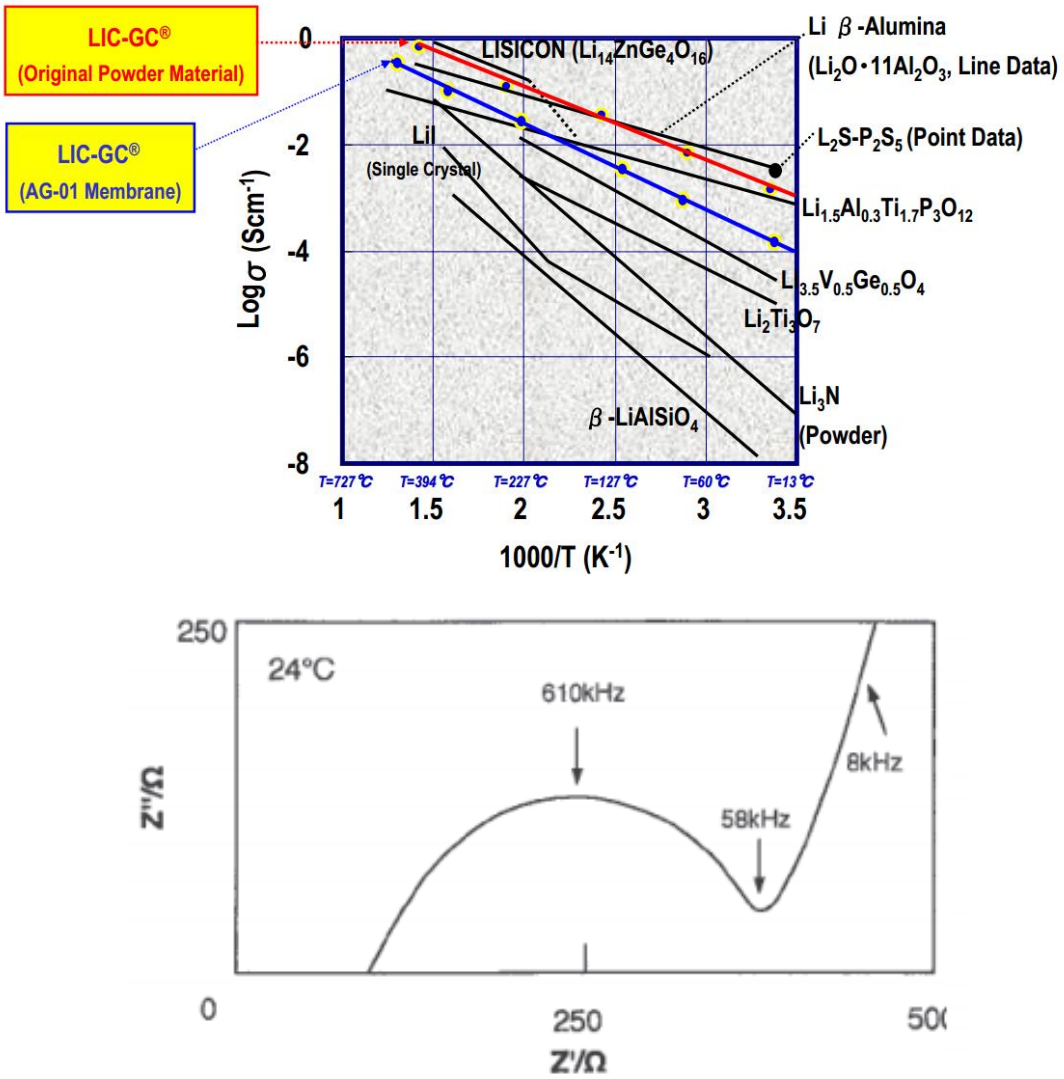

Figure 4.2. a) The ionic conductivity of LICGC lithium conductive ceramic compared with other ceramics; b) impedance spectra of LCIGC membrane. Data provided by Ohara Corp.

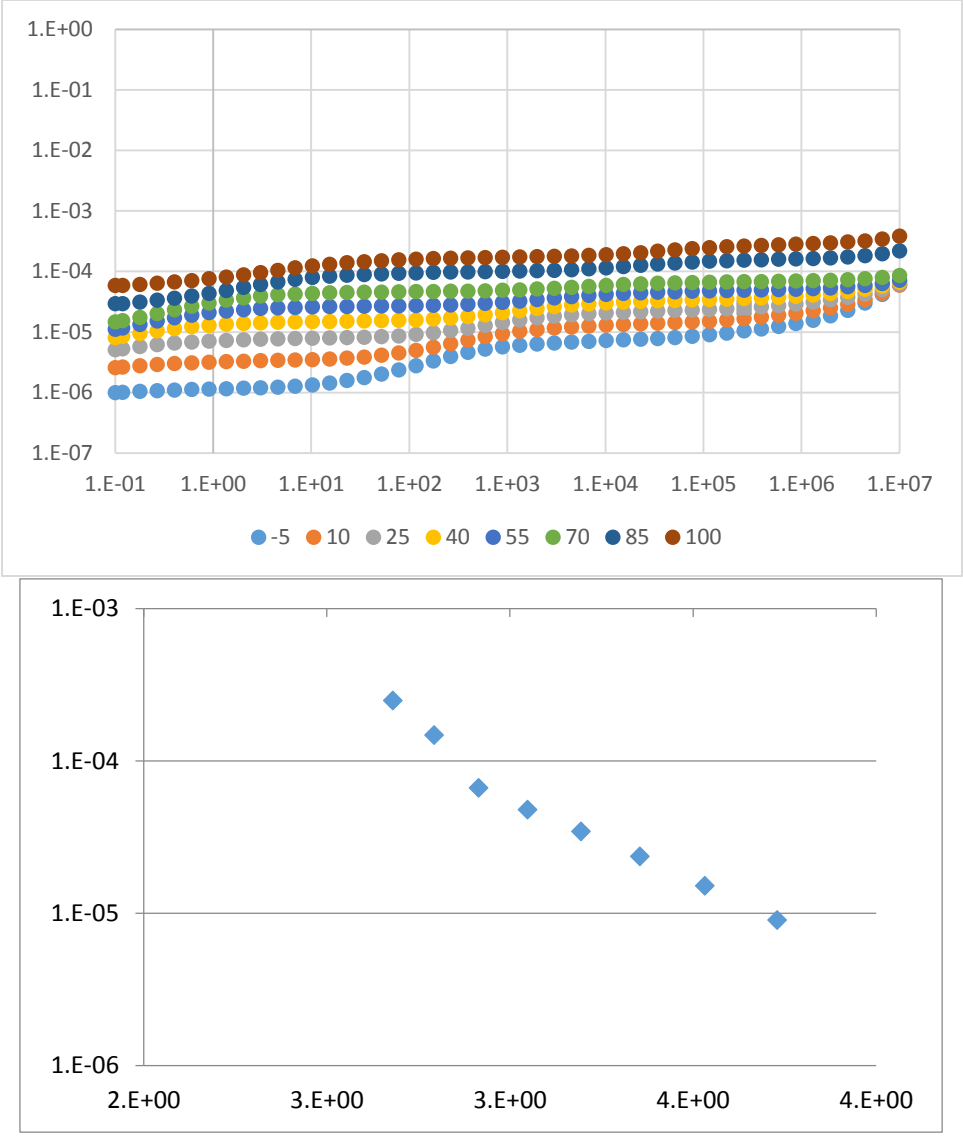

Figure 4.3. top: The AC ionic conductivity of PVDF-HFP/LICGC/PC composite membrane at a temperature range from -5 to 100 ^{o}C; bottom: The extrapolated DC ionic conductivity of the same.

The temperature-dependent impedance spectra of PVDF-HFP/LICGC/PC confirm the existence of two interfaces as shown in **Figure** 4.4. Clearly two semicircles on the complex plane are observed which usually indicates two interfaces or double layers. After fitting the spectra based on the equivalent circuit R(RC)(RC)W, the values of bulk resistance as well as the two interfacial resistance can be obtained (**Figure** 4.5). As expected, all resistance decrease with the increase of temperature. The bulk resistance is lower than 20 ohms at all temperatures, indicating the LICGC/PVDF-HFP/PC shows good lithium transport ability in bulk. However, two large interfacial resistance become the major obstacle for lithium ion movement at the boundary. Compared with the impedance spectra provided from Ohara Corp, R3 is attributed to the ceramic/liquid interface while the R2 could be related to ceramic/polymer interface.

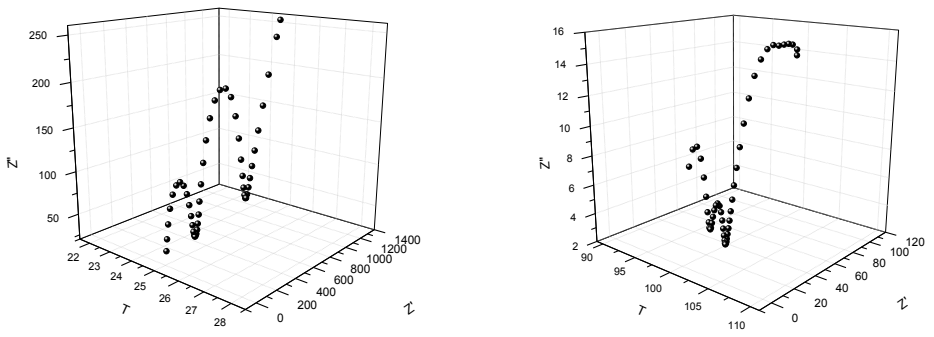

Figure 4.4 the impedance spectra of PVDF-HFP/LICGC/PC at 25^{o}C (left) and 100^{o}C (right)

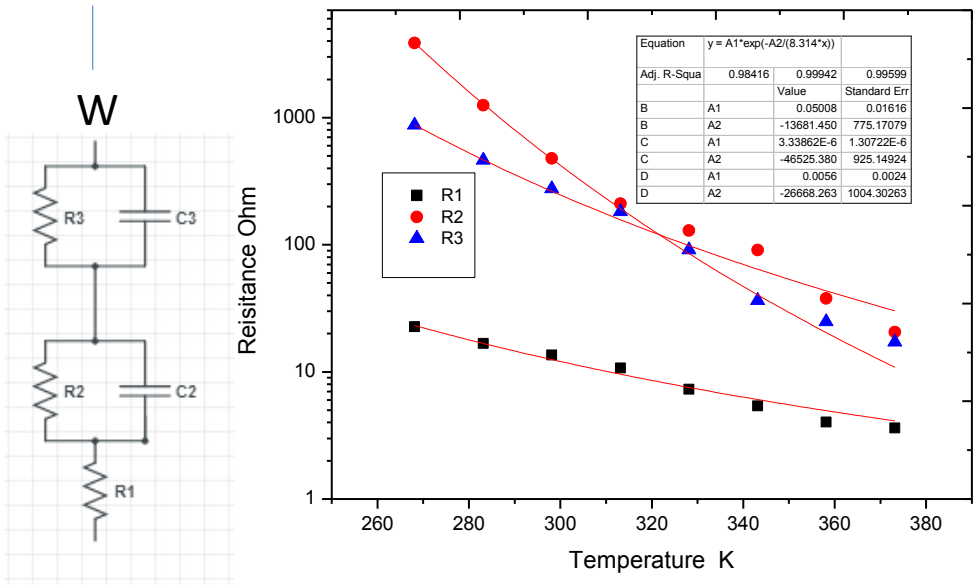

Figure 4.5. The fitted bulk resistance (R1) and two interfacial resistances (R2) based on the equivalent circuit R(RC)(RC)W.

To investigate the dendrite prevention ability of LICGC/PVDF-HFP/PC electrolyte, we have performed the polarization test on the symmetric lithium coin cells with such electrolyte separator. The voltage profile shows that the battery cannot perform stably and will fail in a short period of time. Such short lifetime may be due to the insufficient conductivity and high interfacial resistance of the LICGC/PVDF-HFP/PC. We have planned to test the lifetime of battery at different current density and temperature. But the overly high price of the LICGC membranes limits the further research. Thus, we cast light on another high modulus ceramic materials-nanoporous silica, which is discussed in the next section.

Nanoporous silica based electrolyte

The as-received silica membranes exhibit a diameter of 13mm and a thickness of 0.24 mm. **Figure 4.6** reports the surface of morphology of silica membranes, which clearly shows the coagulation of nanoparticles while the vacant among the nanoparticles form the pores with 100 nm diameter.

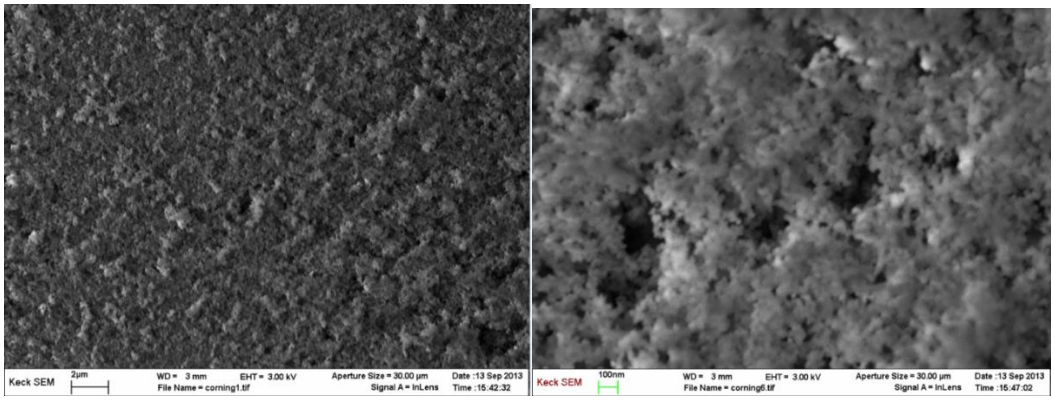

Figure 4.6. Surface morphology of pristine nanoporous silica observed by SEM.

Next step we soaked the pristine nanoporous silica membranes with 1M LiTFSI/PC, following the same procedure as alumina membranes. After being immersed in solvents, such as water or PC, the opaque membranes transfer into a translucent state. The resultant silica separator/electrolyte show a high DC ionic conductivity as we expect, meaning they are capable of holding enough liquid electrolyte and their porosity offer the pathway for ion transportation. **Figure 4.7** presents the AC measurements of conductivity as well as the DC ionic conductivity that are extrapolated based on the same method mentioned in last chapter. The solid line shows the non-linear fitting of the data using Arrehnius equation, and for comparison the conductivity data with fitting of

alumina/PVDF-HFP/LiTFSI/PC separator/electrolyte is also presented. The inset in **figure 4.7** reports the value of the activation energy deduced from Arrehnius fitting, which can be concluded that the bare silica membranes show an even lower energy barrier for lithium ion movement than the alumina separators.

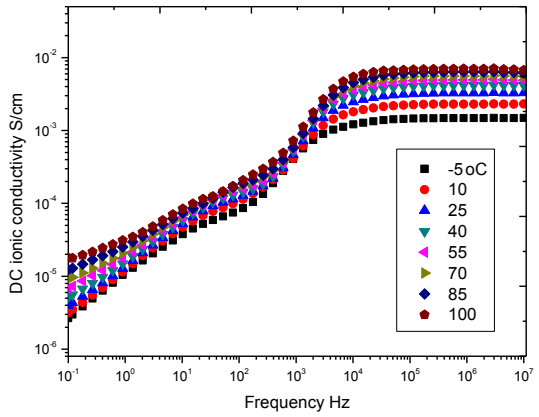

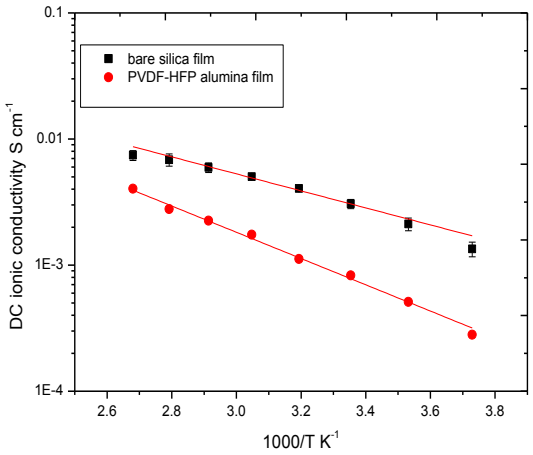

Equation	y=-A*exp(-Ea*x/8.314)		
Adj. R-Square	0.96644	0.99198	
		Value	Standard Error
B	A	-0.55852	0.21633
B	Ea	12.91149	1.04023
D	A	-2.42707	0.77614
D	Ea	19.93846	0.95949

Figure 4.7. AC ionic conductivity of silica/PVDF-HFP/LiTFSI/PC (top) and the extrapolated DC ionic conductivity with Arrehnius fitting (fitting parameters shown in the table).

The impedance spectra of nanoporous alumina/LiTFSI/PC assembled in a symmetric coin cell are measured against temperature in the range from -5 ^{o}C to 100^{o}C, as shown in **Figure** 4.8a. The bulk and interfacial resistance are extrapolated based on the model circuit shown in the inset of **Figure** 4.8b. As expected, both bulk and interfacial resistances decrease with the increase of the temperature. It can be observed that the bulk resistance remain lower than 30 ohms at all temperature, meaning a low ionic transport barrier inside the separator electrolyte. The high interfacial resistance at low temperature indicates that the ions encounter diffusion obstacle at solid/liquid boundary. However, the interfacial resistance decrease to 65 ohms at room temperature 25 ^{o}C.

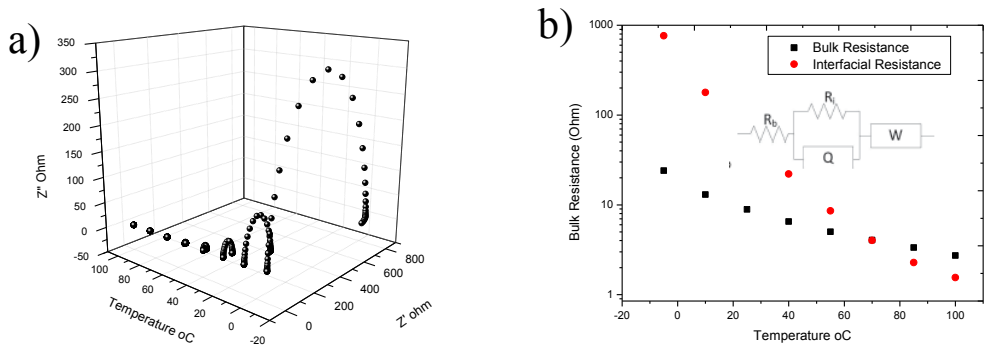

Figure 4.8. a) Impedance spectra of silica/PVDF-HFP/LiTFSI/PC from -5 ^{o}C to 100^{o}C; b) the extrapolated bulk and interfacial resistance based on the equivalent circuit as inset.

In order to evaluate the performance of nanoporous silica/LiTFSI/PC in LMBs, we have applied them in LTO/lithium coin cells as separator/electrolyte to perform galvanostatic cycling test. **Figure** 4.9 reports the Coulombic efficiency and specific capacity of the battery tested at 1C for over 1000 cycles. It can be observed that the average Coulombic

efficiency is close to unity which indicates the stable rechargebility of the battery. The specific capacity loss is small even after 1000 cycles.

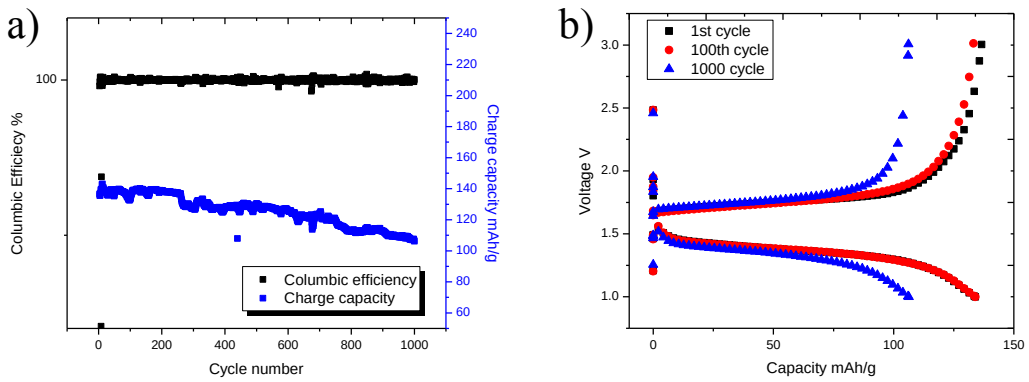

Figure 4.9. Galvanostatic cycling test of LTO/silica/PVDF-HFP/Li battery at 1C (0.44 mA cm^{-2}) a) efficiency and charge capacity and b) the voltage versus capacity at the first cycle, 100^{th} cycle, 1000^{th} cycle, respectively.

We again have performed lithium plating/striping tests on silica based electrolyte/separator in symmetric coin cells (**Figure** 4.10). The nanoporous silica is able to maintain a stable voltage profile for over 1000 hours with no sign of short circuit. The voltage peak at the initial stage is attributed to the SEI formation after which the lithium ion movement enters steady state. The remarkable battery lifetime indicates that the silica membrane offers great dendrite prevention ability, akin to the alumina membranes discussed previously.

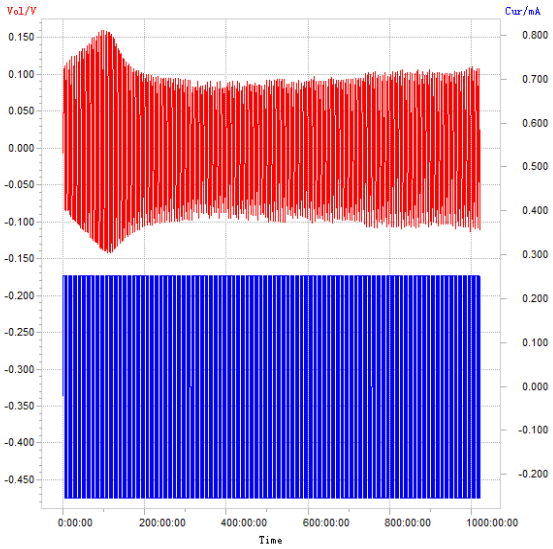

Figure 4.10. Lithium plating/stripping test of Li/silica/PDF-HFP/Li cell at current density of 0.2 mA cm^{-2}.

Comparison between nanoporous silica and alumina in terms of dendrite prevention

We have further employed polarization test on the symmetric coin cells with nanoporous silica/LITFSI/PC separator/electrolyte to assess their ability to retard dendrite under extreme conditions. Unlike lithium plating/striping test, polarization test only allows the lithium ions to move in one direction at constant current density, which results in continuous lithium plating on one electrode until short circuit. **Figure** 4.11 reports the typical voltage profile of polarization test on silica based separator electrolyte at 0.2 mA/cm2. It is surprised to see that although the batteries show remarkable lifetime in lithium plating/striping test, they only survives 120 hours in polarization test. A similar experiment has also been performed using 20 nm Al2O3/PVDF-HFP/LiTFSI/PC, which shows longer lifetime but still becomes short circuit after 300 hours. It can be concluded that in the polarization test, nanoporous alumina membranes which shows more uniform pores structure are able to retard dendrites longer than silica membranes that are randomly coagulated.

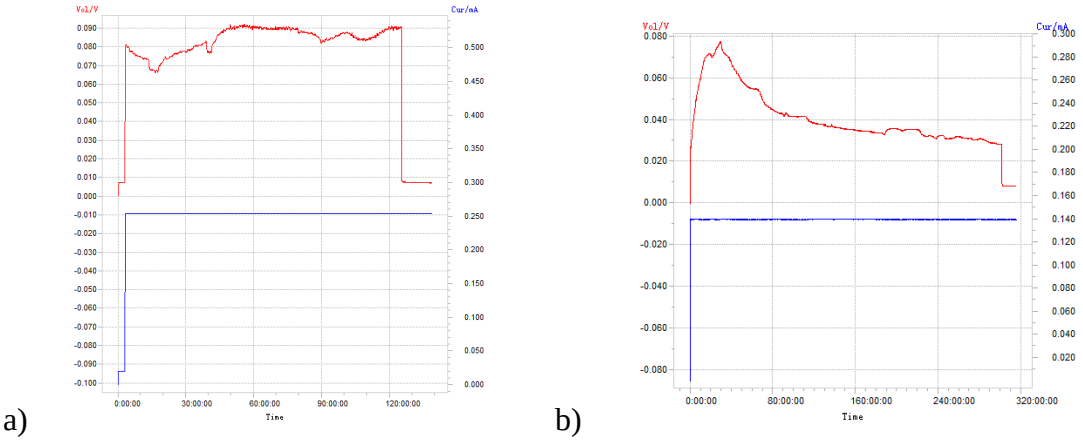

a) b)

Figure 4.11. Voltage profile of the polarization test on a) Li/silica/PDF-HFP/Li cell and b) Li/alumina/PDF-HFP/Li at current density of 0.2 mA cm^{-2}.

a) b)

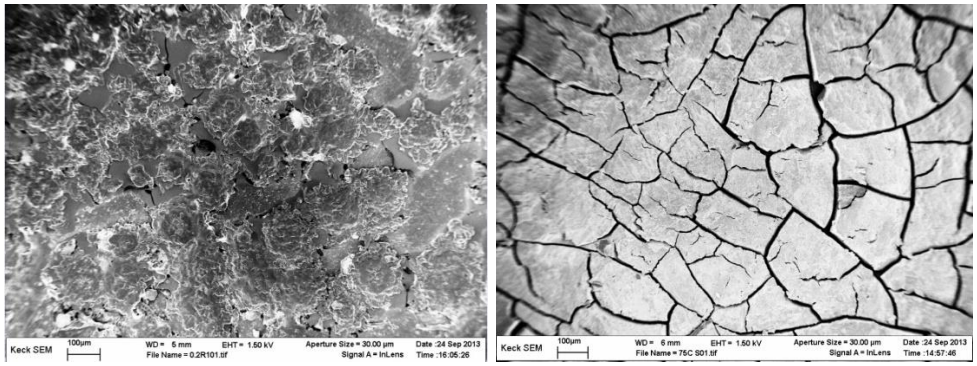

c) d)

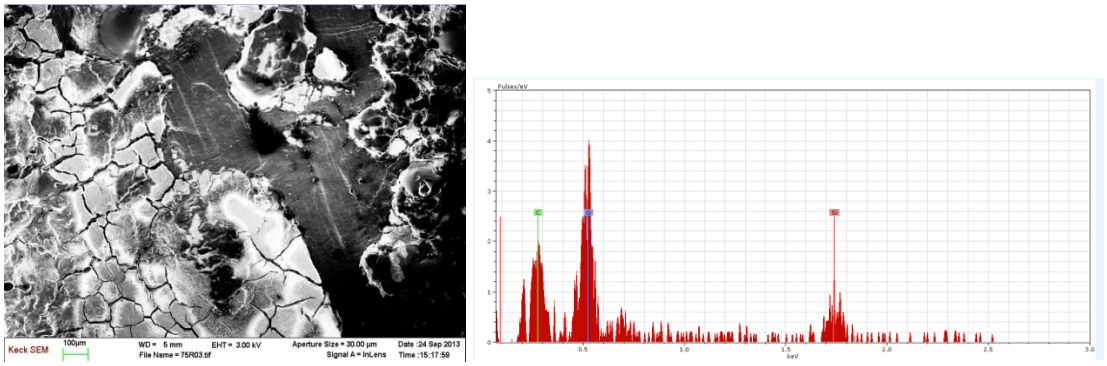

e) f)

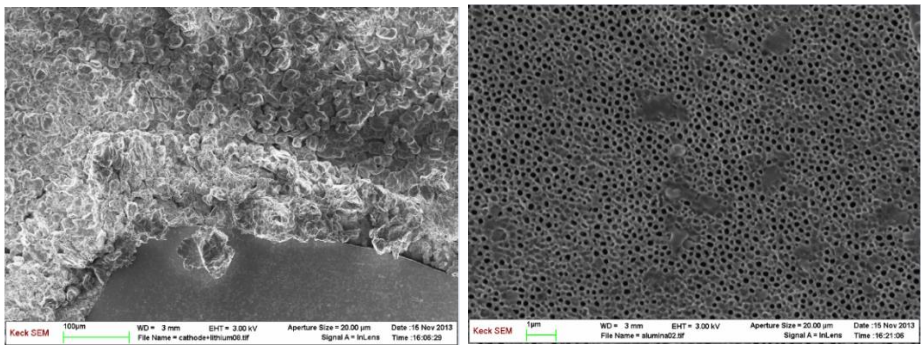

Figure 4.12. Voltage profile of the polarization test on a) Li/silica/PDF-HFP/Li cell and b) Li/alumina/PDF-HFP/Li at current density of 0.2 mA cm^{-2}.

In order to investigate the mechanism of dendrite growth and short circuit happened in polarization test on both silica and alumina separator/electrolyte, post-mortem studies have been conducted. Symmetric coin cells that have been short circuited are disassembled in the argon-filled glove box and are observed by SEM. **Figure** 4.12a and b show both the lithium anode surface and silica membrane surface. The surface of the lithium anode is covered by the mushroom-like dendrites whose size are at micrometer level. It is observed that at some certain region on the lithium surface are covered by the fragments that detach from the silica membrane, which is proved by EDAX analysis that reveals a strong silicon peak. The SEM picture of silica membrane surface also confirms that silica based separator/electrolyte has been damaged during experiment. The resultant micro-cracks could allow dendrite to penetrate through. Thus, the short lifetime of coin cells with silica based separator/electrolyte can be explained by the destruction of porous structure of silica membranes which no longer behave as a mechanical blocking to prevent dendrite proliferation. Careful post-mortem scrutiny have also been conducted on the alumina based separator/electrolyte, as shown in **Figure** 4.12e and f. It can be clearly observe that although lithium surface is electrodeposited to form dendrite structure, the surface of nanoporous alumina is neat and clean. A zoom-out picture focuses on the edge of alumina shows that dendrites are too large in size to travel through the nano-meter pores, but are able to climb over the edge of alumina which causes short circuit. Thus even though the high modulus alumina membranes prevent dendrite from penetrating, they are unable to stop dendrite to spread horizontally which finally spot the edge and cross. By analyzing the results from polarization tests and related post-mortem study, we

have concluded that ceramics membranes are able to retard dendrite prevention by mechanical blocking, but cannot fundamentally avoid dendrite formation.

Chapter 5

LITHIUM HALOGEN SALTS AS ELECTROLYTE ADDITIVE TO STABLIZE LITHIUM DEPOSITION

5.1 Introduction

From previous studies we have concluded that the nanoporous alumina show the best dendrite prevention ability among the materials that we have investigated. The advantage of nanoporous comes from its regular pore size, intact structure, satisfying mechanical property as well as the ability to hold large amount of liquid electrolyte. In chapter 3, the nanoporous alumina/PVDF-HFP composite has been proved to be effective as separator in LMBs. However, such configuration only provides a mechanical barrier to passively block dendrite traveling. In the last section of chapter 4, the disadvantage of such passive defense shows up in the polarization test. The post-mortem SEM study reveals the fact that even though dendrite are suppressed by the application of high modulus separator, they are still capable of growing in other directions. The speculation is that dendrite travel on the separator plane instead of penetrating through the separator. Eventually they spot a micro-crack or reach the edge of the separator and then short the battery.

A longstanding puzzle in the battery field is that secondary batteries based on some metals (e.g. Mg) show no evidence of electrode instability and dendrite formation under deposition conditions where dendrites form and proliferate in others, such as Li [1]. At low surface deposition rates, thermodynamic and surface forces determine whether electrodeposited atoms preferentially form low dimensionality fiber-like structures, which lead to dendrites, or whether they form higher dimensional crystalline phases. Whereas at the intermediate and high surface deposition rates common in batteries, the mobility of atoms at the interface determines whether smooth or rough electrodeposits are created. Density functional theoretical analysis of Mg and Li electrodeposits at a vacuum

metal interface reveal that Mg-Mg bonds are on average 0.18 eV stronger compared to a Li-Li [2]. This means that under the same deposition conditions, the probability of a lower dimension, fiber-like Mg deposit spontaneously transforming to a higher-dimension crystal is more than 1000 times higher than that for the corresponding transition in lithium. In electrolytes, these differences are only slightly altered by the interfacial tension, which is orders of magnitude lower, perhaps explaining why Li surfaces are more prone to nucleate dendrites. A surprising and heretofore unexplored prediction from recent joint density functional theoretical (JDFT) calculations by Arias and co-workers [3] is that the presence of halide ions, particularly fluorides, in an electrolyte produce as much as a 0.13 eV reduction in the activation energy barrier for Li diffusion at an electrolyte-lithium metal electrode interface. If correct, this means that it should be possible to increase the surface diffusivity by more than two orders of magnitude, which should lead to large improvements in the stability of Li electrodeposition and dendrite suppression in simple liquid electrolytes.

We herein report on the stability of lithium electrodeposition in common liquid electrolytes reinforced with halogenated lithium salts. Remarkably, we find that premature cell failure by dendrite growth and proliferation can be essentially eliminated in plate-strip type experiments even at high operating current densities. In more aggressive, high-rate polarization experiments, we find levels of dendrite suppression in room temperature liquid electrolytes that are superior to all previous reports from elevated temperature studies of polymers and other solid-state electrolytes. Experimental characterization of the interfacial tension and impedance at the electrolyte-lithium metal interface confirm that the interfacial mobility is a strong decreasing function of

halogenated lithium salt and is the source of the improved stability of Li electrodeposits in liquids.

5.2 Experiment Section

Pre-determined halogen lithium salt and LiTFSI ($LiPF_6$) was dissolved in PC (1:1 (v:v) EC:DEC). The total lithium salt concentration was kept to be 1 M. The mole fraction of LiF relative to total lithium salt was varied from 0.1-100%. To prepare the anhydrous solution, LiTFSI, $LiPF_6$, LiF, PC, EC and DEC were dried rigorously at the presence of molecule sieves and lithium metal.

Composite nanoporous alumina membranes were prepared based on previously reported approach in chapter 3. Briefly, nanoporous alumina membranes were soaked in Polyvinylidene fluoride hexafluropropylene (PVDF-HFP)/DMF solution. Then a phase separation approach was adopted to prepare sandwich-type alumina/PVDF-HFP membranes. These membranes were further immersed in previously described LiF+LiTFSI/PC electrolyte for at least 24 hours. The coin cell configuration for alumina membrane assembly is displayed in **Figure** 5.1.

Figure 5.1 Cartoon of the coin cell configuration for alumina membrane assembly. Two gray plates are lithium foils while the white one is the laminated membrane.

The thinner $Li_4Ti_5O_{12}$ (LTO) electrodes were composed of 80% of LTO, 10% of carbon black, and 10% of PVDF binder. A pre-determinated amount of N–methylpyrrolidone (NMP) was added as solvent and the resultant slurry was thoroughly mixed. Following procedure involves using a doctor blade to coat slurry on a clean copper sheet and it's rigorously dried in vacuum oven.

The thicker $Li_4Ti_5O_{12}$ (LTO) electrodes (64 microns of the active material) that used in this experiment were produced at the U.S. Department of Energy's (DOE) Cell Fabrication Facility, Argonne National Laboratory.

Symmetric lithium metal coin cells (2032 type, **Figure** 5.2) were used for dielectric spectroscopy, impedance spectroscopy, cycling voltammetry, galvanostatic polarization and cycling measurements. Ionic conductivities were measured by Novocontrol N40 broadband dielectric spectrometer. The galvanostatic polarization and cycling measurements were conducted using Neware CT-3008 battery tester. Impedance spectra were measured as a function of frequency by a step heating procedure using impedance spectrometer. Cells were disassembled and the lithium metal electrodes harvested and rinsed with PC before analyzed by scanning electron microscopy (SEM, LEO1550-FESEM).

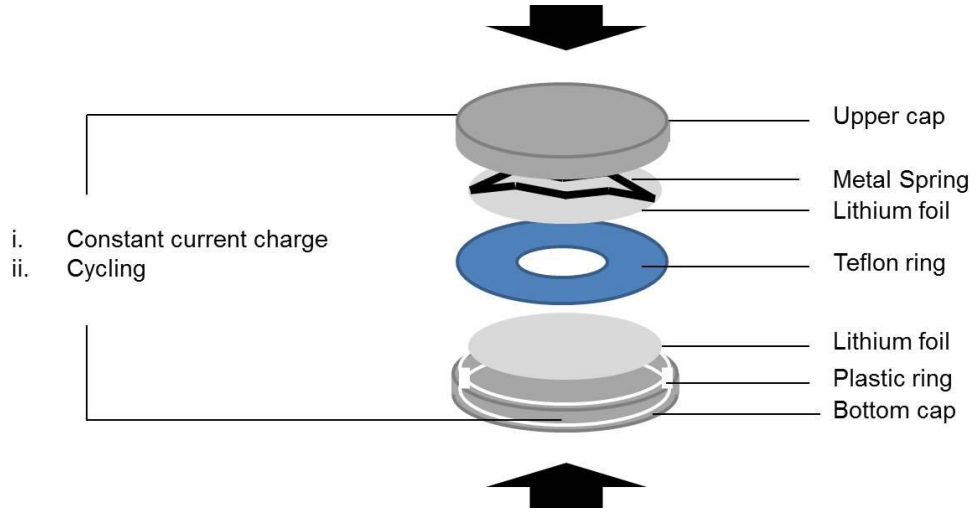

Figure 5.2. The configuration of symmetric lithium cells used in galvanostatic polarization and galvanostatic cycling measurements.

The contact angles were measured at room temperature by a goniometer (ram é-hart, Inc. Model 100-00-115). The lithium foil was placed in a transparent environmental chamber with rubber sealed on the top. A single drop of the test liquid was placed on the substrate via a microliter syringe though the rubber. The contact angle was determined six times at different positions on the material, and the average values were reported.

5.3 Result and discussion

Figure 5.3a reports the DC conductivity for LiF+LiTFSI/PC as a function of LiF mole fraction in the electrolytes. It is apparent that at low LiF concentrations, DC conductivities close to the measured values for a LiTFSI/PC liquid electrolyte control are found. At LiF concentrations above 3 mol percent, the conductivity falls with increasing

LiF content and the shape of the conductivity-versus-temperature profiles are seen to become flatter, but for all compositions studied, room-temperature conductivity well above 10^{-3} S cm^{-1} are observed. A lower bulk electrolyte ionic conductivity upon addition of LiF is consistent with expectations based on the reduced dissociation of the salt, relative to LiTFSI, and consequent lower population of mobile ions in solution. The inset to the figure shows the effect of LiF on the wettability/contact angle (right axis) and surface energy (left axis) of the electrolyte with a lithium metal surface (see supplemental information Figure S5.1 & Table S5.1). The measurements were performed using a home-built contact angle goniometer enclosed in an argon-filled chamber. It is apparent from the figure that addition of LiF causes a non-monotonic decrease in contact angle and a commensurate rise in interfacial energy. Later, we will show that electrodeposition of lithium metal in these electrolytes produce isolated mushroom-like structures of diameter around 40 μm. The increase in surface energy produced upon addition of LiF to the electrolytes are therefore many orders of magnitude lower than the differences in bonding energy between Mg-Mg and Li-Li atoms to significantly change the tendency of Li to form lower dimensional dendritic structures.

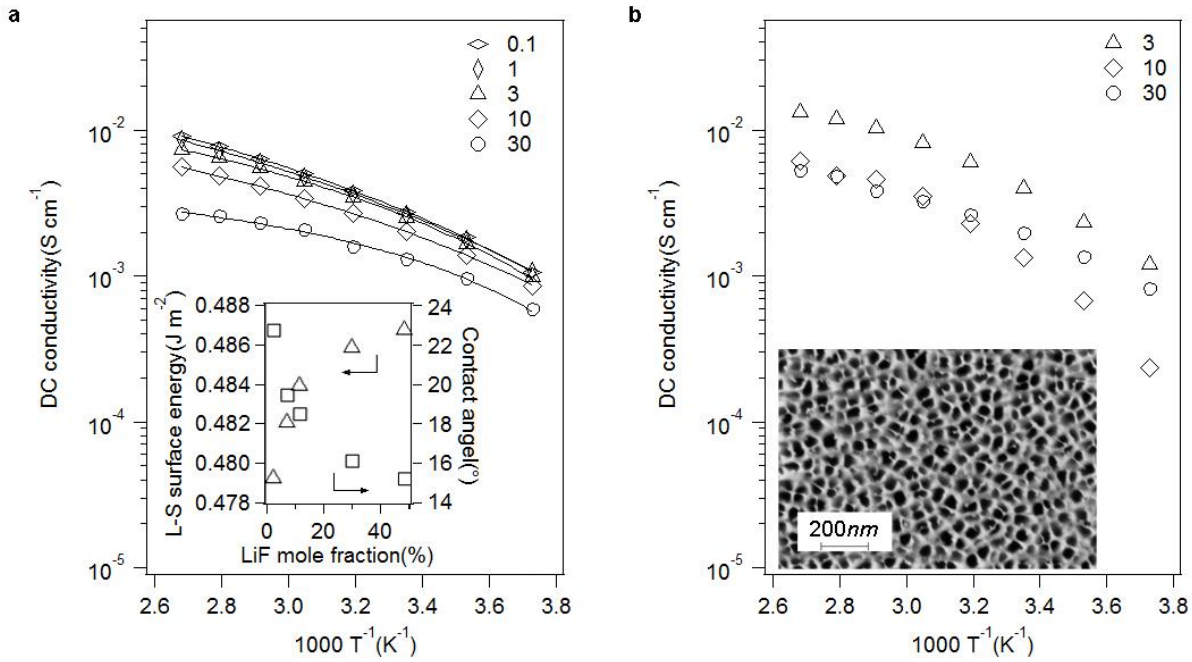

Figure 5.3 DC ionic conductivity of LiF+LiTFSI/PC with various LiF mole fractions as a function of temperature. a, Without alumina/PVDF membrane. The solid lines are Vogel-Fulcher-Tammann (VFT) fits for the temperature-dependent ionic conductivity. The parameters from the VFT fitting are shown in Table S5.2. The inset shows the liquid-solid surface energy and contact angle as a function of LiF mole fraction. b, With alumina/PVDF membrane. The SEM image shows the nanostructure of the alumina membrane with pore diameter around 40nm.

Figure 5.3b reports the DC conductivity for nanoporous solid electrolytes created by infusing LiF+LiTFSI/PC into nanoporous Al_2O_3/PVDF monoliths (see lower inset) with a nominal pore diameter of 40nm. The detailed preparation protocols for these electrolytes are provided in the supplementary materials section. It is apparent from **Figure** 5.1b that while the effect of LiF composition on conductivity is more complex, over the range of LiF compositions studied the electrolytes again exhibit room-

temperature conductivities above 10^{-3} S cm^{-1} underscoring their suitability as room-temperature electrolytes for lithium batteries. Electrochemical stability of the LiF-containing electrolyte was characterized by cyclic voltammetry and the results reported in (**Figure** S5.2). With 30mol% LiF, the width of electrochemical stability window is observed to increase noticeably. The peak in the voltammogram at around 4.1 V *vs.* Li/Li^+ in the first cycle is consistent with formation of a passivation film on the electrode that protects the electrolyte.

We investigated electrodeposition of Li in the liquid and nanoporous LiF+LiTFSI/PC based electrolytes using galvanostatic cycling of Li|LiF+LiTFSI/PC|Li symmetric lithium cells in which the lithium striping/plating process is cycled over three-hour charge and discharge intervals designed to mimic operation in a LMB. The cells are designed to ensure that during each three-hour period sufficient lithium is transported between electrodes to create a dendrite bridge in the inter-electrode space to short-circuit the cells. The cells also do not include a separator and, once formed, the only resistance to dendrites bridging the inter-electrode spacing is provided by the intervening liquid electrolyte.

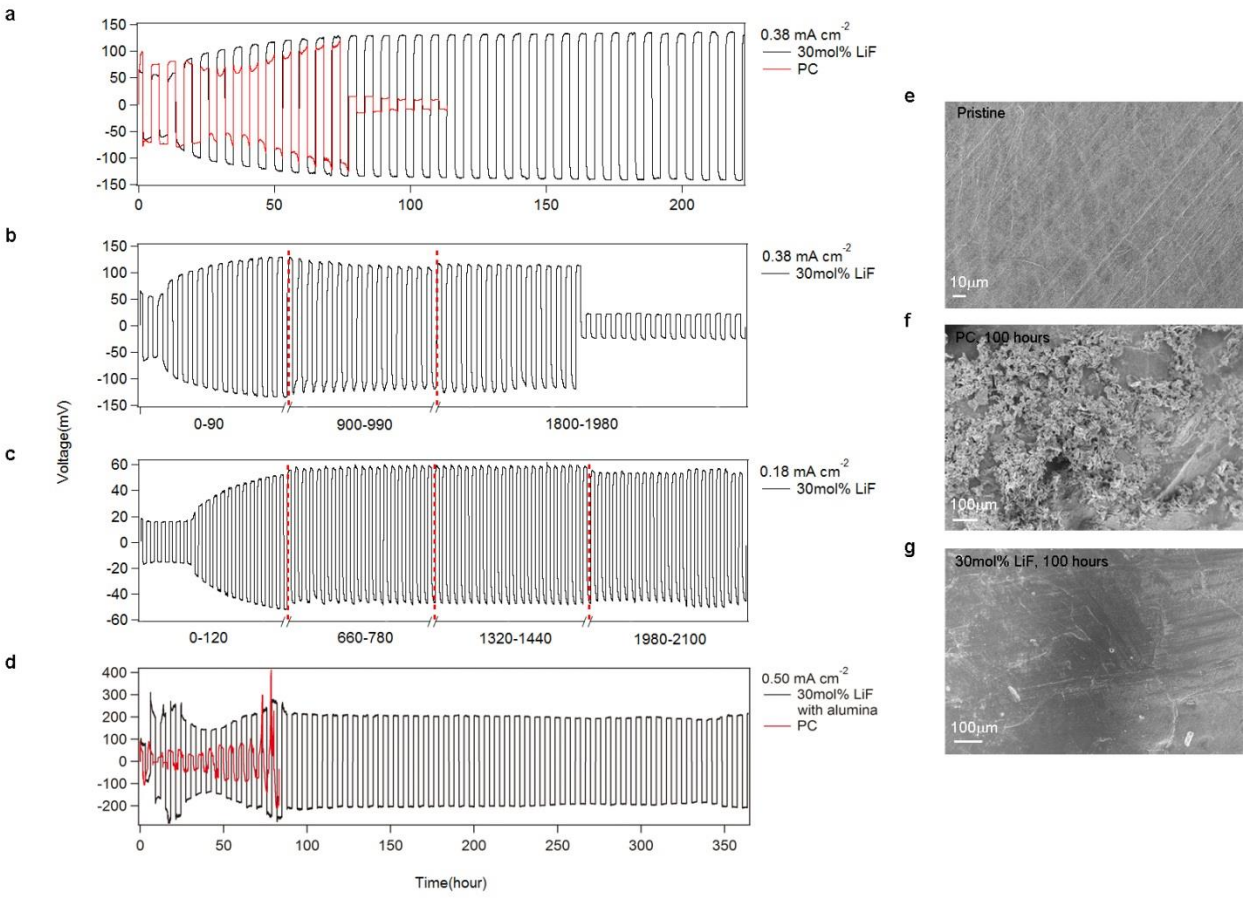

Figure 2 | Voltage versus time for a symmetric lithium cell with each half cycle lasts 3 hours. a, Initial voltage profiles of 30mol% LiF+LiTFSI/PC (black) and LiTFSI/PC (red) electrolytes at a current density of 0.38mA cm^{-2}. **b**, Voltage profile of 30mol% LiF+LiTFSI/PC electrolyte at a current density of 0.38mA cm^{-2} before observing cell short-circuits. **c**, Typical voltage profile for LiF+LiTFSI/PC electrolytes at lower current densities (less than 0.2mA cm^{-2}). **d,** Initial voltage profiles of 30mol% LiF+LiTFSI/PC (black) and LiTFSI/PC (red) electrolytes with alumina/PVDF membrane at a current density of 0.50mA cm^{-2}. The initial voltage disturbance is due to the electrolyte consumption and SEI layer formation. The voltage reaches a stable plateau after 80 hours and lasts for over 350 hours. Such stable performance at high current density originate from two factors: 1) the LiF additive stabilizes the lithium deposition and forms a flat surface, which are in favor of steady battery usage; 2) the high modulus of alumina separator prevents the dendrite proliferation and avoids the short-circuit. SEM analyses: **e**, Pristine lithium anode before galvanostatic cycling. **f**, Lithium anode in contact with LiTFSI/PC electrolyte after 100-hour cycling at 0.38mA cm^{-2}. **g**, Lithium anode in contact with 30mol% LiF+LiTFSI/PC electrolyte after 100-hour cycling at 0.38mA cm^{-2}. LiF at a fixed, high current density of 0.38 mA cm^{-2}.

Figure 5.2a compares the voltage profiles observed in symmetric cells containing electrolytes with and without LiF. The figure shows that cells that do not contain LiF in the electrolyte exhibit a large and irreversible drop in voltage consistent with catastrophic failure by a dendrite-induced short-circuit, in as little as 75 hours (i.e. less than 13 cycles of charge and discharge) of operation. In contrast, cells containing 30 mol% LiF in the electrolyte cycle stably for more than 1800 hours (300 cycles of charge and discharge) before succumbing to failure in the same manner. This nearly 25-fold enhancement in cell lifetime achieved upon addition of LiF to a liquid electrolyte is considerably higher than any previous report for cells in which solid polymers, composites and other mechanical agents are used to protect lithium metal electrodes against failure by dendrite-induced shorts. It is also significant that the current experiments are performed at substantially higher current densities and at room temperature. **Figure** 5.2c reports voltage profiles for cycling experiments performed at comparable current densities as in previous studies using polymers and other mechanical agents. Remarkably, even after 2100 hours of continuous operation, the cell shows no evidence of failure. **Figure** 5.2d reports a similar result for cells based on nanoporous membranes infused with liquid electrolytes, but cycled at a very high current density of 0.5 mA cm^{-2}(also see **Figure** S5.3). Again, while cells with the control LiTFSI/PC electrolyte are seen to quickly fail, those containing LiF in the electrolyte are seen to settle down over a period of around 75 hours and to cycle stably for more than 350 hours.

Figures 5.2e-g are scanning electron micrographs of the lithium metal electrode surface before cycling (e), after 100 hours of cycling in a LiTFSI/PC control electrolyte (f), and after 100 hours of cycling in a LiF+LiTFSI/PC electrolyte containing 30 mol% LiF (g). It

is evident from the figure that the improved lifetimes of the cells containing LiF coincides with the observation of virtually pristine Li metal electrodes after extended cycling.

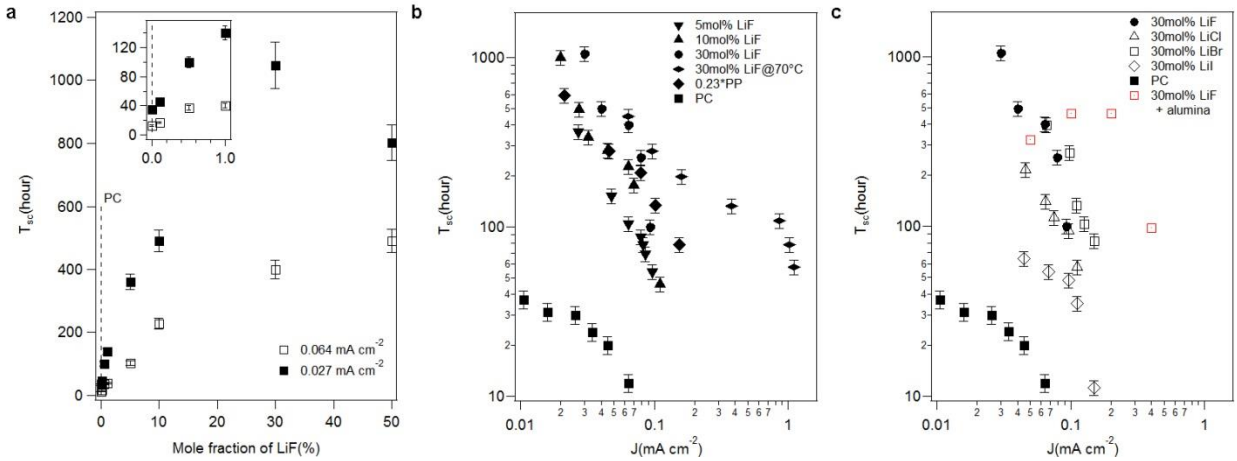

Figure 5.3 Short-circuit time T_{sc} from galvanostatic polarization measurements for symmetric lithium cells. a, T_{sc} as a function of LiF mole fraction at 0.027mA cm^{-2}, 0.064mA cm^{-2}. b, T_{sc} as a function of current density *J* for various LiF concentrations and for PP-TFSI. c, T_{sc} as a function of current density J for different lithium halides with 30mol % of the halide. The red markers are used to represent results for cells based on nanoporous alumina/PVDF membranes infused with LiF+LiTFSI/PC electrolytes, which show no evidence of short circuits at any of the current densities studied. Measurements were conducted at room temperature unless indicated.

Unidirectional galvanostatic polarization of symmetric lithium cells provides a convenient, accelerated-testing scheme for assessing the stability of lithium metal electrodes during electrodeposition. In this approach, lithium is continuously striped from one electrode and plated on the other until short-circuit occurs. A constant current density is applied to the cell and the corresponding voltage profile is obtained as a function of time (**Figure** 5.4a). The time (T_{sc}) at which a sharp drop-off in the potential is observed provides an estimate for its lifetime. Because there is no pause in the deposition, as occurs when the direction of the current is reversed in the cyclic plate-strip experiment discussed in the last section, there is no opportunity for defects produced by instability in one deposition cycle to heal before they nucleate dendrites that ultimately short circuit the cell. Consequently, cell failure by dendrite-induced short circuits are observed on timescales as much as one order of magnitude lower than for the plate-strip cycling measurements [4].

Figure 5.3a reports measured T_{sc} values as a function of LiF concentration in the electrolyte at two current densities. Consistent with the observations reported in the previous section, the figure shows that addition of LiF to a LiTFSI/PC electrolyte produces large increases in cell lifetime. The top inset shows that addition of as little as 1mol% LiF produces more than a three-fold enhancement in cell lifetime at both low (0.027 mA cm^{-2}) and moderate (0.064 mA cm^{-2}) current densities. The figure further shows that at a higher LiF contents the relationship between T_{sc} and LiF composition in the electrolyte is nonlinear. At 30 mol % LiF, it is seen that more than a 30-fold enhancement in cell lifetime is achieved at either current density, confirming the earlier observations based on cyclic plate-strip experiments. The ability of LIF salt to extend cell

lifetime seems to reach its maximum level at around 30mol% LiF. For higher LiF mole fraction (50mol% LiF), there is a decrease of T_{sc}, which might be attributed to the low DC conductivity or low mobile ion concentration. It is also difficult to polarize the cell at relatively high current density for the same reason.

Figure 5.3b studies the effect of current density, J, and temperature on T_{sc} for electrolytes containing varying concentrations of LiF, including an PC electrolyte containing 23 vol% of the ionic-liquid methy-3-propylpiperidinium (PP) TFSI known for its exceptional ability to facilitate stable electrodeposition of lithium. It is clear from the figure that both in terms of the variation of T_{sc} with J and the enhancements in lifetime achieved relative to the electrolyte without additives, the LiF-based electrolytes with around 30 mol % LiF perform at least as well as those containing PP TFSI. As previously reported for electrolytes containing PP TFSI, T_{sc} exhibits a power-law dependence on J , $T_{sc} \sim J^{-m}$, over a wide range of current densities. Power law exponents m obtained from the data are provided in **Table** S5.2 and show no noticeable dependence on LiF composition. It is also apparent from the figure that at 70 ^{o}C electrolytes containing LiF exhibit T_{sc} values with little sensitivity to J over a range of current densities, allowing these electrolytes to achieve 100-fold or more enhancements in cell lifetime, relative to the control electrolyte at 25 ^{o}C. **Figure** 5.3c nicely shows that LiF is not unique and that other halogenated lithium salts, especially LiBr, are able to significantly extend lifetime of lithium metal electrodes. **Figure** 5.3c further shows that T_{sc} values measured using nanoporous electrolytes (also see **Figure** S5.4) containing LiF are virtually insensitive to J even at high current densities. And, remarkably show no evidence of short circuiting at high current densities normally inaccessible in galvanostatic polarization experiments in

symmetric Li cells. The potential profiles and post-mortem SEM analysis for these cells are provided as supplementary **Figures** S5.5 and S5.6.

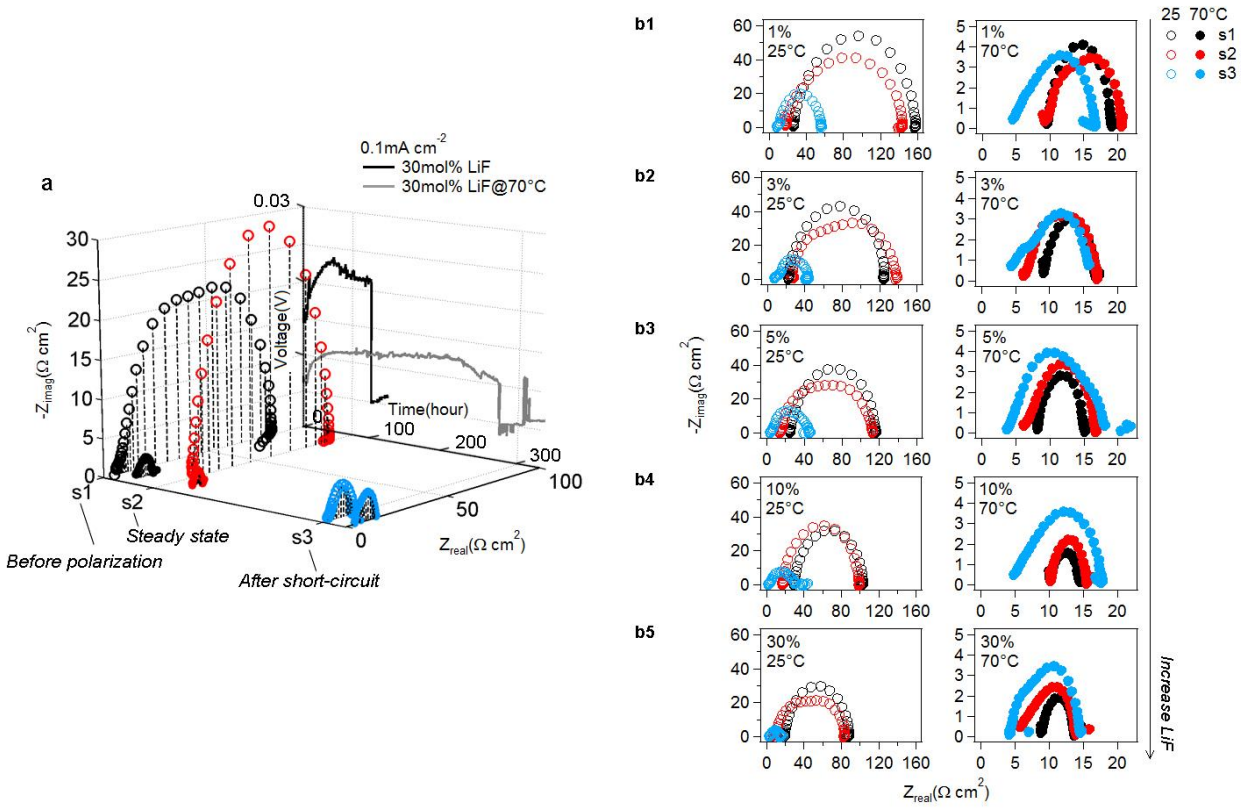

Figure 5.4 Voltage profile at a fixed current density, impedance spectra of the three stages (s1: before polarization, s2: steady state, s3: after short-circuit) at 25 ℃ and 70 ℃. a, Voltage profiles and impedance spectra at 0.1mA cm^{-2} for 30mol% LiF+LiTFSI/PC electrolyte. b, Impedance spectra for 1mol%, 3mol%, 5mol%, 10mol% and 30mol% LiF+LiTFSI/PC electrolytes. The impedance spectra with alumina/PVDF separator are shown in Figure S5.7.

Analysis of the electrode-electrolyte interface at different stages of polarization provides additional insight into the role played by LiF. Impedance spectra before polarization, at steady state, and after cell failure were collected and typical results reported in **Figures** 5.4a,b. Measurements were performed at 25 ℃ and 70 ℃ to characterize the effect of temperature. It is readily apparent from the figure that the interfacial impedance (related to the width of the curves) drops noticeably at the point of short-circuiting. Note that it is not possible to fit the impedance spectra by an equivalent circuit model because the surface is no longer uniform once the dendrite starts to form. **Figure** 5.4a compares the impedances of the three stages for 30mol% LiF+LiTFSI/PC electrolyte at 25 ℃ and 70 ℃. Both the bulk (related to the lower intercept of the spectra) and interfacial impedances decrease sharply with only a 45 ℃ temperature increase.

Figure 5.4b displays the impedance spectra for 1mol%, 3mol%, 5mol%, and 10mol% and 30mol% LiF + LiTFSI/PC electrolytes individually. At 25 ℃, the bulk and interfacial impedances is seen to change slightly after the onset of polarization, but as already noted drops substantially after the cell short-circuits. Electrolytes with higher LiF mole fraction have comparable bulk, but measurably lower interfacial impedances at all stages. It suggests that LiF has the ability to enhance the lithium ion diffusion primarily at the electrode/electrolyte interface. When operating at 70 ℃, spectra at all three stages exhibit similar bulk and interfacial impedances between 5 and 15 Ω cm^2 with negligible dependence of electrolyte composition. It indicates that the impedance is so small that the magnitude is almost similar to that of the short-circuited cell, which consistent with expectations based on the JDFT calculation, leads to much larger enhancements in cell lifetime. In general, the lowered impedance created by LiF leads to the extension of the

cell lifetime, and the sharply reduced impedance by temperature explains the tremendous enhancement of cell lifetime at high temperature because lithium ions can easily migrate and plate on the negative electrode.

To further evaluate the suitability of LiF-added electrolytes in LMBs, more commonly used electrolytes comprised 1:1 (v:v) EC:DEC with and without LiF were investigated at room temperature using $Li/Li_4Ti_5O_{12}$ (LTO) half-cell. LTO is a no-strain material commercially utilized in electric vehicles and is capable of cycling at both low and high rates for consecutive charge and discharges. In practice, even commercial LTO spinel powder yields a well-defined discharge plateau at 1.55V in carbonate electrolytes, and a discharge capacity close to the theoretical capacities (175 mAh g^{-1}) when accommodating lithium and negligible round-trip IR losses [5]. To characterize the effect of LiF on performance of Li/LTO half-cell, thin LTO (15 microns of active material) and thick LTO (64 microns of the active material) were studied in an accelerated procedure employing a very high current density of 2.0 mA cm^{-2} (1C). For cells based on the thick LTO electrode, an activation process at 0.1C for 10 cycles was employed prior to the higher current density experiments. A two-hour charge/discharge protocol allows enough lithium to be transported during each cycle to create dendrites that are large enough to short-circuit the cells based on the thick electrode, whereas those based on the more common thin electrodes do not allow sufficient lithium transport to create a dendrite that spans the inter-electrode space.

Figure 5.5(a1-b1) show the voltage profiles obtained using the thin electrodes with and without LiF additive. It is apparent that addition of LiF to the electrolytes increases the discharge capacity, but otherwise does not alter the cycling performance of the cells. The

blow-up charge and discharge curves in **Figures** 5.5(a2) and **Figures** 5.5(b2) show that the round-trip IR losses in both cells are quite minimal. The corresponding results for the thick electrodes are reported in **Figures** 5.5c,d. It is apparent from the voltage profiles in Figure 5(c1) and Figure 5(d1) that whereas little change in voltage amplitude occurs in cells with/without LiF, the electrolytes increased the discharge capacity for both LTO electrodes.

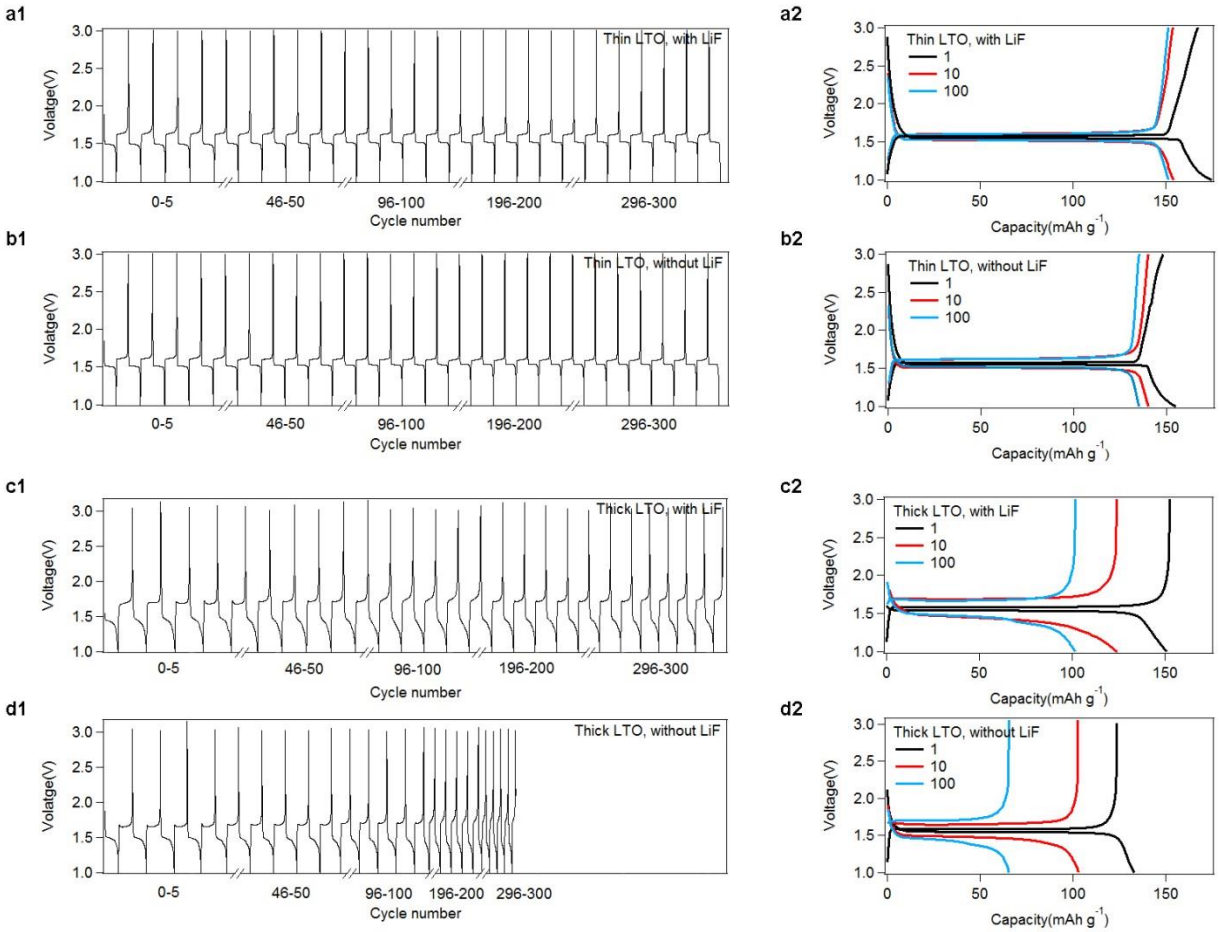

Figure 5.5 Charge-discharge characteristics of Li/$Li_4Ti_5O_{12}$ (Li/LTO) with 30mol% LiF+LiTFSI/EC:DEC and LiTFSI/EC:DEC electrolytes at room temperature. Thin LTO electrode: Voltage *vs.* time profile for the first 5 cycles, 46-50 cycles, 96-100 cycles, 196-200 cycles and 296-300 cycles at 1C rate (0.18 mA cm^{-2}) with LiF (a1) and without LiF

(b1). About 0.88μm lithium (charge passed=0.65C cm^{-2}, about 2.2μm LTO is reacted) is transported from one electrode to the other in each half cycle. Initial, 10^{th}, 100^{th} charge-discharge profiles with LiF (a2) and without LiF (b2). Thick LTO electrode: Voltage *vs.* time profile for the first 5 cycles, 46-50 cycles, 96-100 cycles, 196-200 cycles and 296-300 cycles at 1C rate (2 mA cm^{-2}) with LiF (c1) and without LiF (d1). About 9.8μm lithium (charge passed=7.2C cm^{-2}, about 24.5μm LTO is reacted) is transported from one electrode to the other in each half cycle. Initial, 10^{th}, 100^{th} charge-discharge profiles with LiF (c2) and without LiF (d2).

Supplemental Information

Table S5.1| Contact angles, liquid electrolyte surface tensions (γ_L), lithium surface energy (γ_S) and solid/liquid interfacial energies (γ_{SL}) of various electrolyte compositions.

Sample	θ(°)	cos(θ)	Electrolyte surface tension($N\ m^{-1}$)	Liquid-solid surface energy($J\ m^{-2}$)
Pure PC	23.0	0.92	0.0448	0.479
Pure DMC	7.3	0.99	0.0291	0.491
PC/1M LiTFSI	22.0	0.93	0.0426	0.480
5 mol% LiF	19.5	0.94	0.0403	0.482
10 mol% LiF	18.5	0.95	0.0381	0.484
30 mol% LiF	16.0	0.96	0.0358	0.486
50 mol% LiF	15.0	0.97	0.0336	0.487
Li: 0.52 $J\ m^{-21}$; PC: 0.045 $N\ m^{-12}$; DMC: 0.0286 $N\ m^{-13}$				

Table S5.2 | VFT fitting parameters and scaling exponent by power law fitting. The fittings of these two equations were conducted by Origin 8.0.

Sample	VFT: $\sigma = A\exp(-B/(T-T_0))$			$T_{SC} = AJ^{-m}$
	$A(S/cm)$	$B(K)$	$T_0(K)$	m
0.1 mol% LiF	0.081 ± 0.0029	461 ± 12	162 ± 2.1	-
1 mol% LiF	0.079 ± 0.0011	485 ± 5.1	156 ± 0.88	-
3 mol% LiF	0.035 ± 0.0028	291 ± 22	188 ± 4.9	-
5 mol% LiF	-	-	-	1.42
10 mol% LiF	0.0033 ± 0.0085	365 ± 8.1	168 ± 1.7	1.53
30 mol% LiF	0.0061 ± 0.00097	127 ± 32	215 ± 12	1.70
100 mol% LiF	0.00052 ± 0.000030	506 ± 21	138 ± 3.8	
30 mol% LiF @ 70 ℃	-	-	-	0.60
30 mol% LiCl	-	-	-	1.36
30 mol% LiBr	-	-	-	2.10
30 mol% LiI	-	-	-	1.27

The continuous lines through the data in Figure 1a are obtained by fitting the experimental results to the Vogel-Fulcher-Tammann (VFT) formula, $\sigma = A\exp(-B/(T-T_0))$, where B is the effective activation energy barrier, in the units of absolute temperature; T and T_0

are the measurement and reference temperatures, respectively; and A is a pre-exponential factor which equals to the ionic conductivity in the high-temperature limit. The equation fits the data over the range of temperature and lithium fluoride content studied[4-6]. The short-circuit time *vs.* current density by galvanostatic polarization measurement is fitted by power law dependence[7-10:] $T_{SC} = AJ^{-m}$. The parameter A is related to the diffusion coefficient of ions, mobile ion concentration, anion transport number, and ion mobility[8-10].

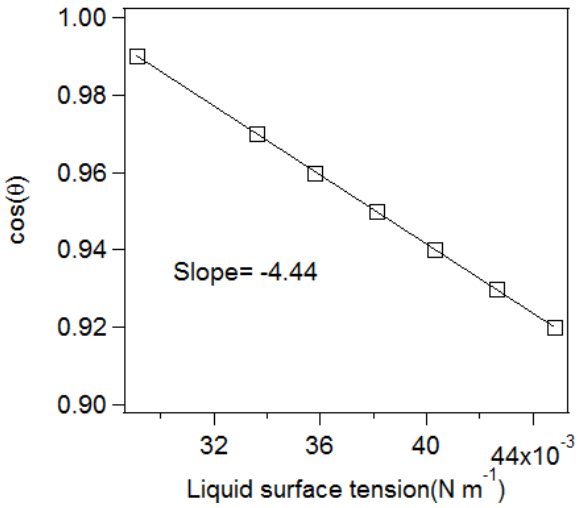

Figure S5.1 | Zisman's plot ($\cos\theta$ vs. γ_L) for LiF+LiTFSI/PC, PC, DMC on lithium metal surface. Based on Zisman approach, the contact angle of different liquids on the same surface is linearly dependent on the liquid surface tension.

Further analysis of the surface tension provides considerable insight of this dendrite suppression mechanism. The surface angle was measured by a goniometer and the liquid-solid (electrolyte-lithium substrate) surface energy was obtained by Young's equation and Zisman approach[11-13].

Surface energy calculation:

$$\gamma_L \cos\theta = \gamma_S - \gamma_{SL} \quad (1)$$

$$\cos\theta = 1 - b(\gamma_L - \gamma_C) \quad (2)$$

Where γ_L is the experimentally determined surface energy (surface tension) of the liquid (electrolyte), θ is the contact angle, γ_S is the surface energy of the solid (lithium: 0.52 J m^{-2}), γ_{SL} is the solid/liquid interfacial energy, b is the slope of the regression line and γ_C is the critical surface tension when $\cos\theta = 1$.

The contact angle of each liquid was measured from a goniometer. b and γ_C are calculated from (2) by γ_L (from literature) and θ (from measurement) of the pure PC and DMC solvents. The rest of γ_C with different amount of LiF were extracted from the regression line (Figure S1). γ_{SL} were then calculated from (1). Note that the deviations of the measurements and Zisman calculation may apply but the results in terms of the L-S surface energy change very small due to the large lithium surface energy compared with that of a liquid electrolyte. Results from this method are displayed in **Table S5.1**. This analysis suggests that although the contact angle decreased by LiF concentration increment, the L-S surface energy has negligible increase which is essentially due to the high surface energy of lithium. There are two possible mechanisms related to this behavior. First, during this aggressive polarization, the striped lithium ions deposit on the negative lithium electrode and create a newly formed lithium surface. For the initially deposited lithium ions, they tend to create a homogenous dispersity since the lithium surface is pristine thus the current density is uniform on the surface. When the liquid electrolyte has great wettability (the tendency of the electrolyte to spread out over a flat, solid surface), the lithium ions near the negative electrode are prone to migrate. This migration follows the nanostructure created by the formerly deposited lithium ions creating a concentrated lithium sheet during the subsequent deposition. In addition, because of the relatively homogenous surface morphology, the centralization of the current density along the surface is reduced, which also retards the propagation of the dendrite growth. Consequently, the cell lifetime is prolonged when the contact angle is decreased. Second, during the dendrite proliferation process, the lithium ions are more likely to deposit on dendrite tips when the surface energy is low. This is due to the energy for creating a new surface on the tip is higher than that on

a flat surface. So the propagation of the dendrite would be suppressed by increasing the S-L surface energy[14-17]. The experimental results convince that by lowering the contact angle or increasing the S-L surface energy, the surface roughness of lithium substrate tends to decay.

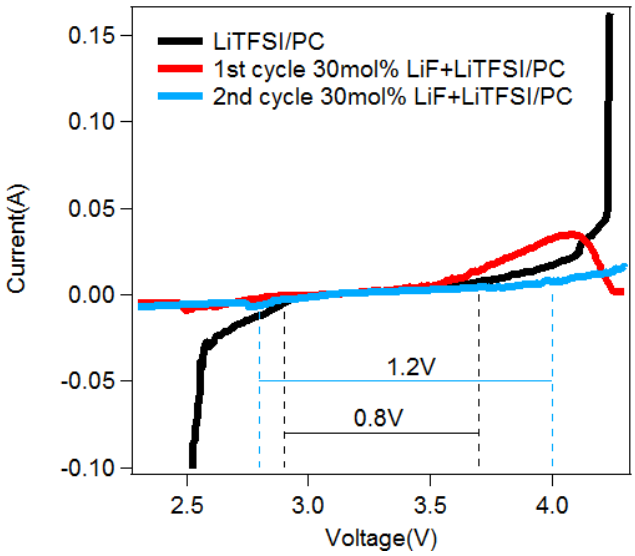

Figure S5.2| Electrochemical stability window from cyclic voltammetry measurements for 1M LiTFSI/PC and 30mol% LiF+LiTFSI/PC at a rate of 0.5 mV s^{-1}. The measurements were conducted in symmetric lithium cells.

Figure S5.2 exhibits that by doping 30mol% LiF additive, the electrochemical stability window of the electrolyte increases from 0.8V to 1.2V *vs.* Li/Li^+. A passivation film was created around 4.1 V *vs.* Li/Li^+, proved by a peak appeared in the first cycle but disappeared afterwards. The combination of carbonate with fluorinated salt could have similar effect as fluorinated carbonate compound which has low melting point, increased oxidation stability and less flammability[18].

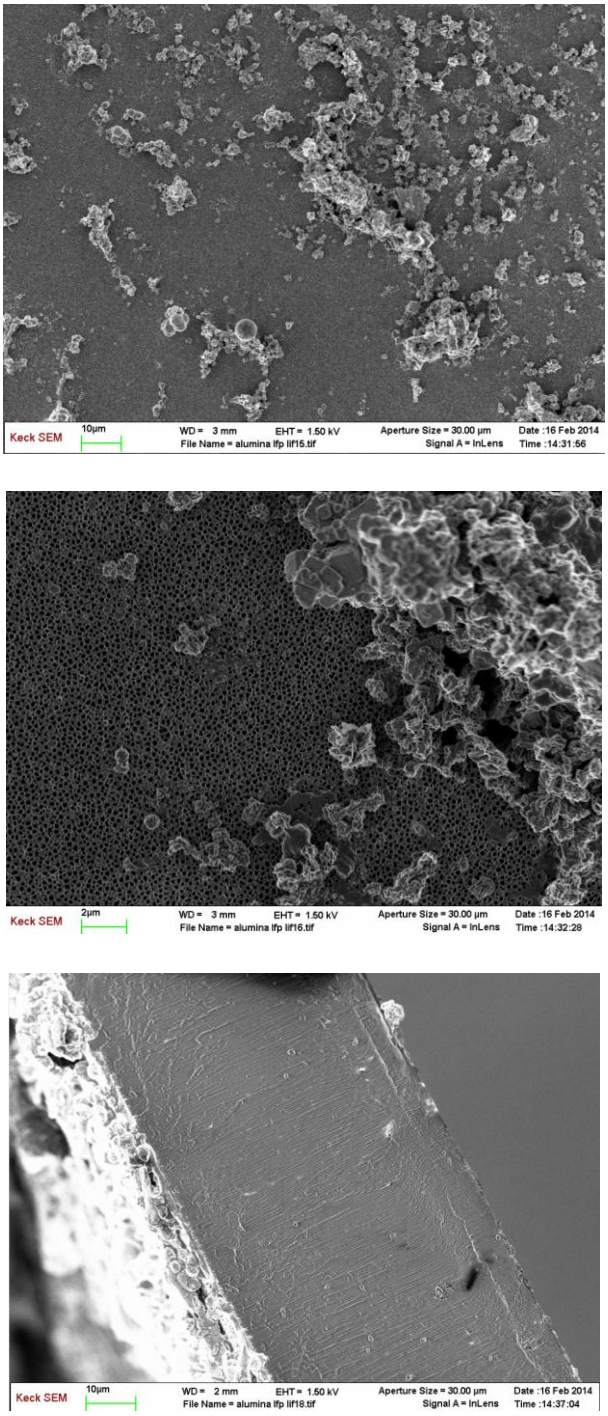

Figure S5.3| SEM analysis of alumina/PVDF-HFP separator and lithium substrate after 400 hours lithium plating/striping test at 0.5 mA cm^{-2}. a, Alumina/PVDF-HFP separator with lithium metal on one side. **b**, Zoom in picture of **a**. **c**, cross section of alumina/PVDF-HFP lithium surface.

Figure S5.3 shows the SEM pictures of alumina separator after 400 hours lithium plating/striping test at 0.5 mA cm^{-2}. The alumina surface is sparsely covered by dendritic structure, which cannot penetrate through the pores on separator. This proves that although porous structures in alumina allow ions to move through for high conductivity, they are small enough to prevent dendrite movement. The morphology of lithium surface indicates that the size of lithium dendrite is much larger than the pore size, meaning that the dendrite cannot penetrate through the porous media.

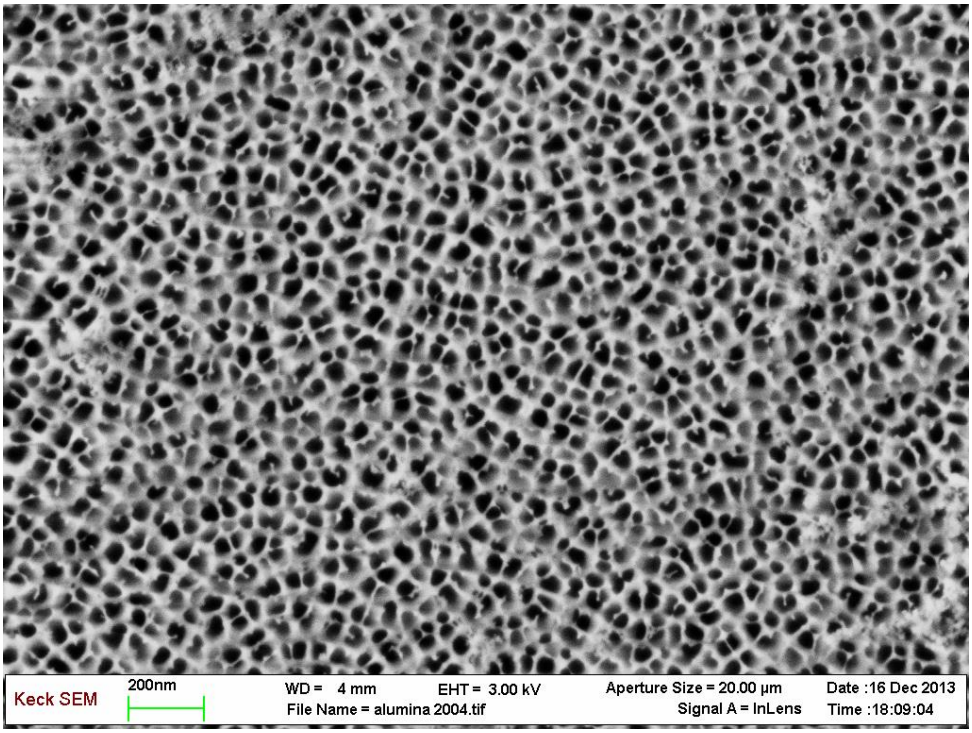

Figure S5.4| SEM analysis for nanoporous alumina membranes. The pore size of the alumina film is around 20nm.

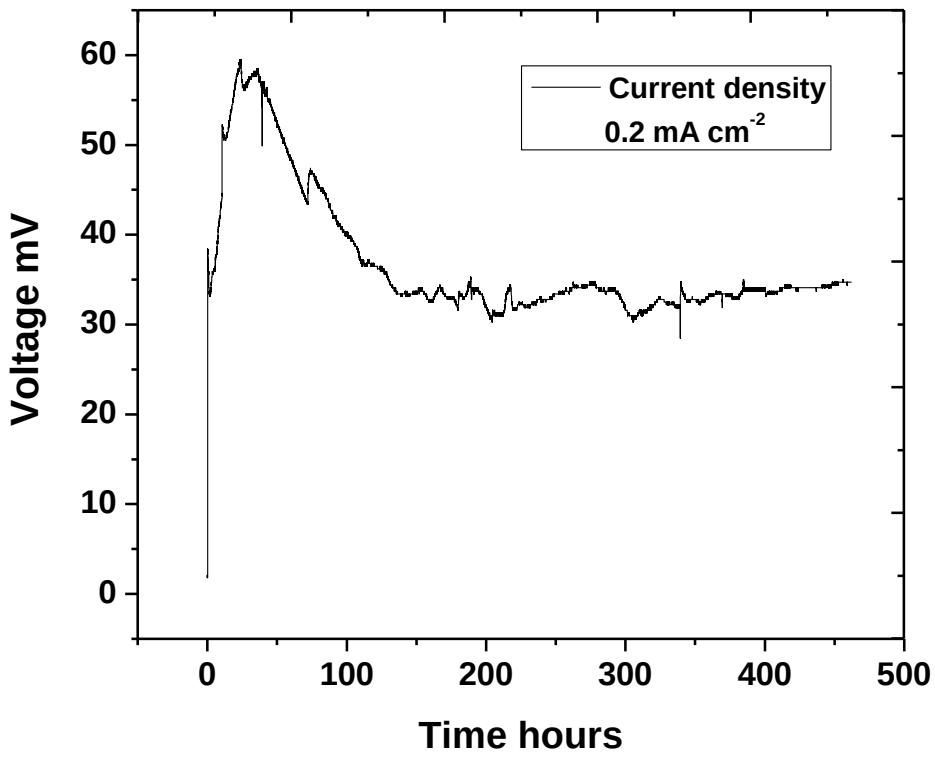

Figure S5.5| Potential profile for symmetric lithium cell with 30mol% LiF+LiTFSI/PC using nanoporous alumina separator. The current density for this typical polarization test is 0.2 mA cm^{-2}.

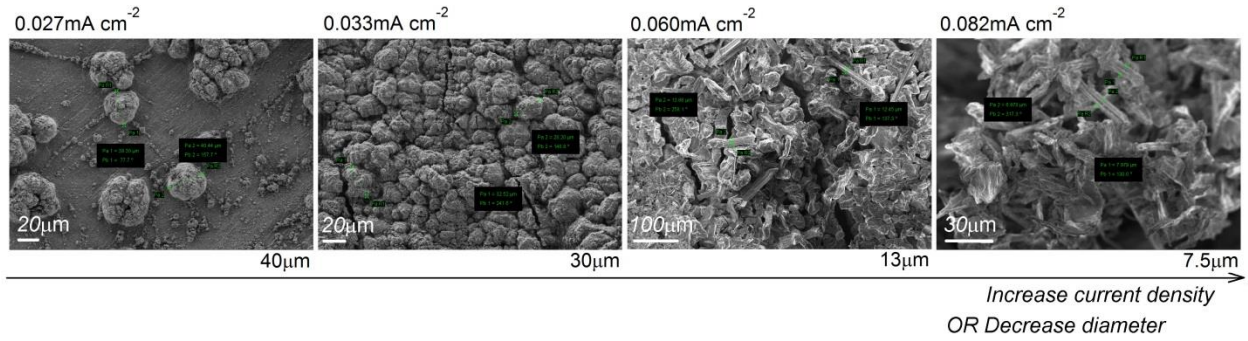

Figure S5.6| Post-mortem SEM images of the lithium negative electrodes at various polarization current densities. The average cross section diameters are shown on the bottom right of each picture.

Figure S5.6 exhibits the post-mortem SEM images of the lithium negative electrodes at various polarization current densities. It shows that the majority of the electrodes were still flat (Figure S8) after short-circuiting, with small patches of mushroom-like dendrite at low current densities (i.e. 0.027 mA cm^{-2}, 0.033 mA cm^{-2}) and thicker needle-like structure at high current densities (i.e. 0.060 mA cm^{-2}, 0.082 mA cm^{-2}). Note that at current density as high as 0.082 mA cm^{-2}, it is difficult to focus all the dendrite tips in one x-y plane because the structures are thick and overlapped. The average cross section diameter of each dendrite structure arises from 7.5 to 40 microns as reducing the polarization current density. To obtain the average diameter, the smallest tips in each figure are chosen for calculation because they are the most possible dendrites to cause a short circuit. Specifically, the current density is higher on a tip with larger curvature, thus the dendrite growth rate increases.

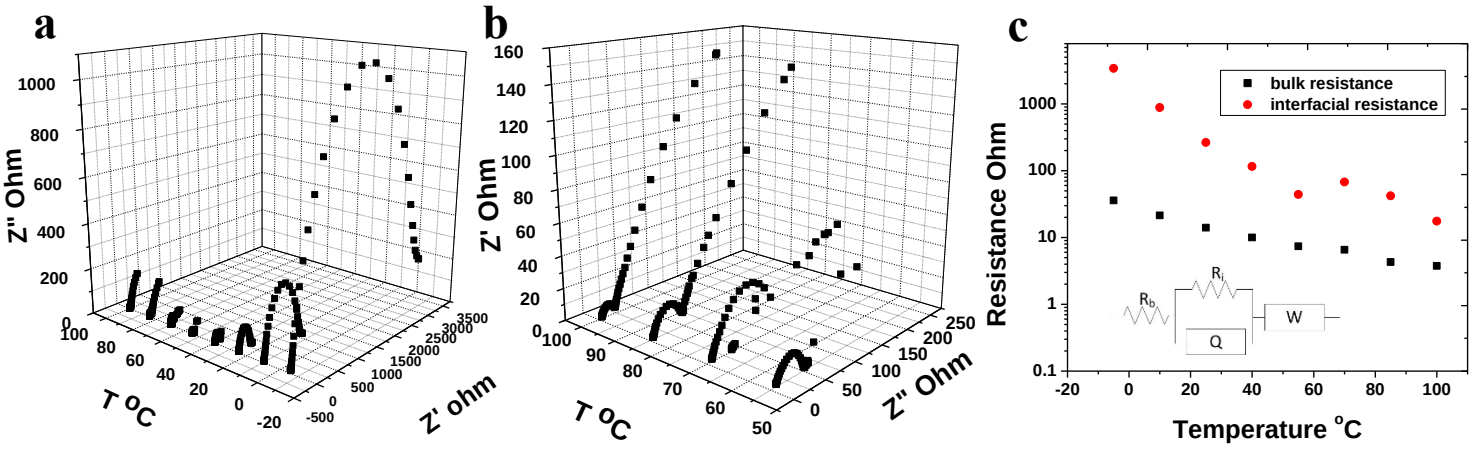

Figure S5.7| Impedance spectra of 30% LiF + LiTFSI/PC in alumina/PVDF separator. a, Impedance spectrum versus temperature of 30% LiF + LiTFSI/PC in alumina/PVDF separator. **b**, A zoom-in impedance spectrum in **a** from 55 ℃ to 100 ℃. **c**, Extrapolated bulk and interfacial resistance from **a**; the fitting circuit is shown as inset.

Figure S5.7 reports the impedance of 30% LiF+LiTFSI/PC soaked in alumina separator. As expected, both real and imaginary impedance decrease within the increase of temperature from -5 ℃ to 100 ℃. **Figure S5.7** shows a zoom-in impedance spectrum from 60 to 100 ℃. An R(RQ)W circuit model is used to extrapolate bulk and interfacial resistance. The results are displayed in **Figure S5.7**. It's clear that the alumina/PVDF separator with 30% LiF additive shows low bulk and interfacial resistances at room temperature, which is favor of battery function. The interfacial resistance unexpectedly increases at 75 ℃ and then decreases again, indicating that diffusion at interface becomes the dominating factor that influences the charge transport.

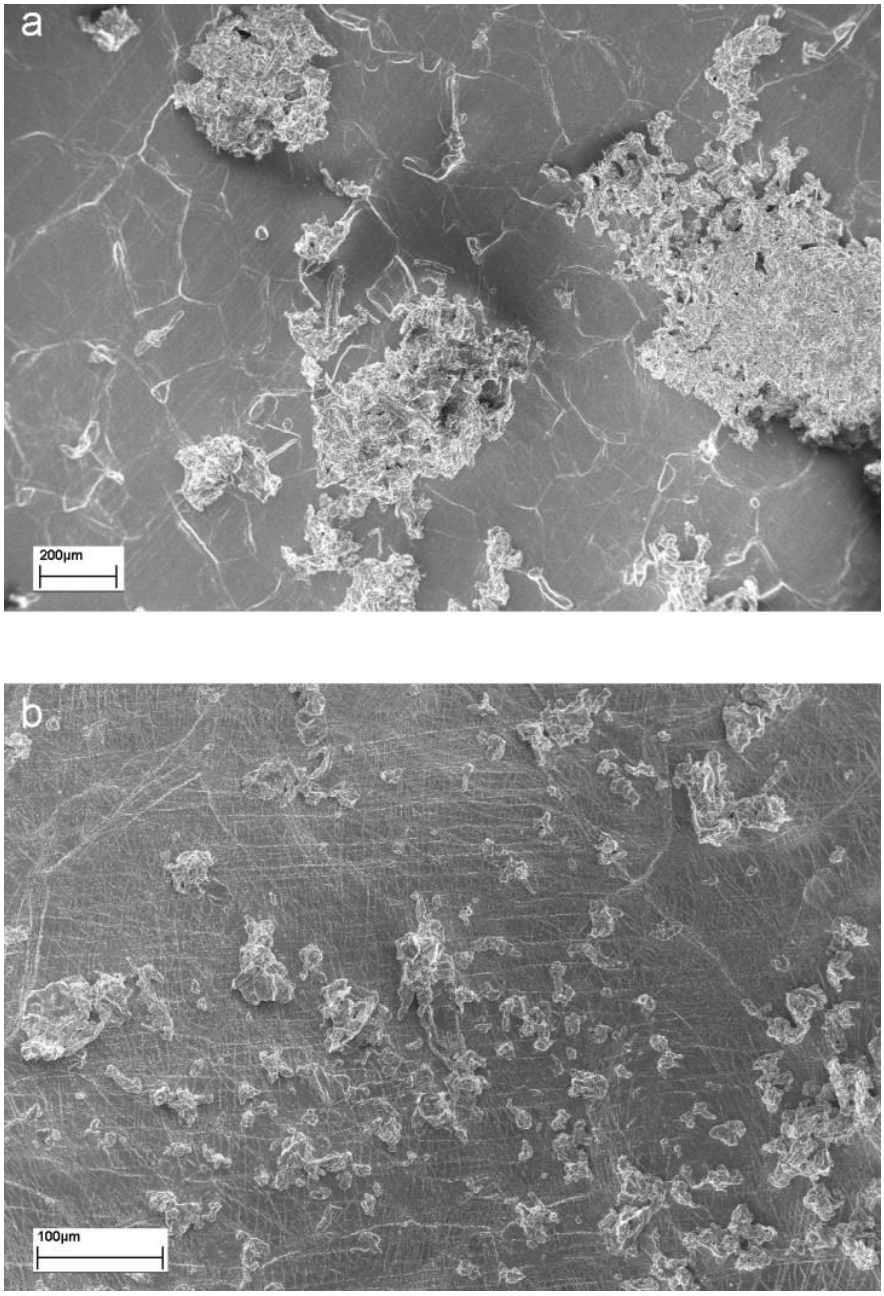

Figure S5.8 | Post-mortem SEM images of the lithium negative electrodes after galvanostatic polarization measurement. a. at fixed current density of 0.082mA cm^{-2}. b. at fixed current density of 0.06mA cm^{-2}.

Figure S5.8 shows that the majority of the lithium electrode was still flat after cell short-circuits by polarization test, especially for electrode after higher current density charging. The dendrite tip is smaller under higher current density. The dendrite tip with smaller size collects more lithium during ion deposition, because such dendrite tip has large curvature which increases the local current density. As a result, the flat surface is prone to remain flat while the dendritic area tends to amply the roughness.

1. Aurbach, D., et al., *Prototype systems for rechargeable magnesium batteries.* Nature, 2000. **407**(6805): p. 724-727.
2. Ling, C., D. Banerjee, and M. Matsui, *Study of the electrochemical deposition of Mg in the atomic level: Why it prefers the non-dendritic morphology.* Electrochimica Acta, 2012. **76**: p. 270-274.
3. Gunceler, D., et al., *The importance of nonlinear fluid response in joint density-functional theory studies of battery systems.* Modelling and Simulation in Materials Science and Engineering, 2013. **21**(7).
4. Lu, Y.Y., et al., *Ionic-Liquid-Nanoparticle Hybrid Electrolytes: Applications in Lithium Metal Batteries.* Angewandte Chemie-International Edition, 2014. **53**(2): p. 488-492.
5. Yi, T.F., et al., *Recent development and application of Li4Ti5O12 as anode material of lithium ion battery.* Journal of Physics and Chemistry of Solids, 2010. **71**(9): p. 1236-1242.

Chapter 6

NANOPOROUS ALUMINA/FUNCTIONAL POLYMER LAMINATES AS NOVEL SEPARATOR/ELECTROLYTE

6.1 Introduction

Rechargeable lithium-based battery is one of the most promising battery candidates for high energy storage devices. Unfortunately, significant improvements in safe and stable battery performance are needed due to the non-uniform lithium deposition on the negative electrode [1, 2]. The uneven dendritic structures increase the potential risk of cell short-circuiting, energy fading or even fire hazards [3]. Recent discoveries and advances have focused on electrolyte reconfigurations for the sake of suppressing or even eliminating dendrite formation.

Electrolytes with high lithium transference number are promising candidates for both lithium metal and lithium ion batteries [4]. They are able to lower the internal resistance, extend the cell lifetime, increase the energy density, and enhance the cycle life of lithium battery. An electrolyte with low lithium transference number exhibits low lithium ion mobility regardless of the overall conductivity of the system is high or not, which leads to low active material utilization and ion concentration gradient during charge and discharge cycles. The concentration gradient lowers the rate capability of the batteries and causes the nucleation of lithium dendrites. Previously, researchers have developed lithium salts with bulky immobile anions such as LiTFSI and $LiPF_6$. But these salts are not cost-effective and usually have a lithium transference number lower than 0.5. Moreover, they are highly flammable, leaky and may cause fire hazards when combined with conventional liquid solvents [5]. These electrolytes usually form dense and concentrated solid electrolyte interface after reacting with lithium metal. It hinders the lithium ion diffusion and migration, which consequently prejudices the lithium ion plating.

One possible approach to increase the lithium transference number is to create immobile lithium counter-ions, which are essentially tethered anions or the anion with low mobility. Based on the previous study in our group, the employment of ionic liquid modified silica nanoparticles in the electrolyte is capable of fixing TFSI anions which significantly enhances the transference number and elongates the battery lifetime. The experiment is in accordance with theoretical simulation in Chazaviel's model predicting that the high lithium transference number can help achieving dendrite-free battery operation by mitigating the space charge region [6]. Nanoporous alumina based laminates are considered as a powerful platform to fabricate high transference number electrolyte due to their controllable pore structure and chemical flexibility. Thus we are considering to adopt the similar approach to modify the nanoporous alumina with ionic liquid, expecting an enhanced lithium transference number by fixing anions.

Another approach in parallel to functionalize alumina/polymer composites is to laminate nanoporous alumina with charged polymer, in which case anions are fixed on the polymer backbones so that only cations are allowed to move freely. A number of literature have reported the application of polyelectrolyte as lithium transport medium with high lithium transference number [7]. We have herein prepared nanoporous alumina based laminates with various functionalized polymer. The list of polymer includes polyacrylic acid (PAA), polystyrene sulfonates (PSS), PSS based block polymer and Nafion. Some of these studies are in progress.

6.2 Experimental Section

Silane attached imidazole based ionic liquid was synthesized as reported before [8]. Briefly, 1-Methyl-imidazoe and (3-chloropropyl)trimethoxysilane were dissolved in DMF at 80 ^{o}C. The solution is further purified by liquid extraction and solvent evaporation to form trimethoxysilane functionalized ionic liquid (Silane-IL). Excessive amount of LiTFSI was added into the ionic liquid to substitute the anion to $TFSI^{-}$. The nanoporous alumina membranes were placed in a home-made mesh cage (**Figure** 6.1) which was hanged in a reaction bottle. The height of the cage was adjusted so that a magnetic stirring bar can be placed underneath. Silane IL was slowly added into the reaction bottle with strong stirring. The reaction lasts for 12 hours at 100 ^{o}C. The excess silane-IL were rigorously removed in ether/ethanol mixture. The membrane were characterized by TGA and FTIR. The conductivity of the membranes were measured by N40 Novocontrol Broadband Dielectric Spectrometer. The pore size and surface area of the pristine alumina were studied based on BET measurement.

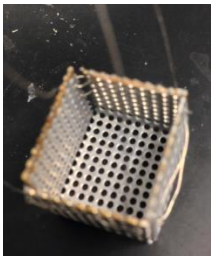

Figure 6.1. Homemade cage for functionalizing brittle ceramics

Active polymer (PAA, PSS, PSS based block polymer and Nafion)/nanoporous alumina laminates were prepared by the solvent casting approach. Briefly, a predetermined amount of active polymer solution was dispersed on a clean piece of Kapton polyimide

film, and then the nanoporous alumina was placed on the polymer solution. After evaporating the solvent, the Kapton film was carefully peeled of and thus an intact active polymer/alumina membrane was obtained. Then the composite membranes were lithated by soaking in 2M LiCl solution for overnight, and then 0.05M LiOH was used to titrate the pH to neutral. The lithated composite membranes were rinsed with DI water and transferred into large amount of PC with the presence of molecule sieves and lithium metal. PC was repeatedly refreshed to remove the residual water. The laminated membranes were characterized by dielectric spectrometer, SEM, EDAX, TGA, FTIR and related battery studies, as described in previous chapters.

6.3 Result and discussion

Ionic liquid functionalized nanoporous alumina

Silane-ionic liquid is chosen as the reactant to functionalize nanoporous alumina based on Popat et al.'s previous work[9]. Alumina surface is able to form monovalent or multivalent Al-O-Si bonds and thus immobilize ionic liquid, as shown in **Figure** 6.2.

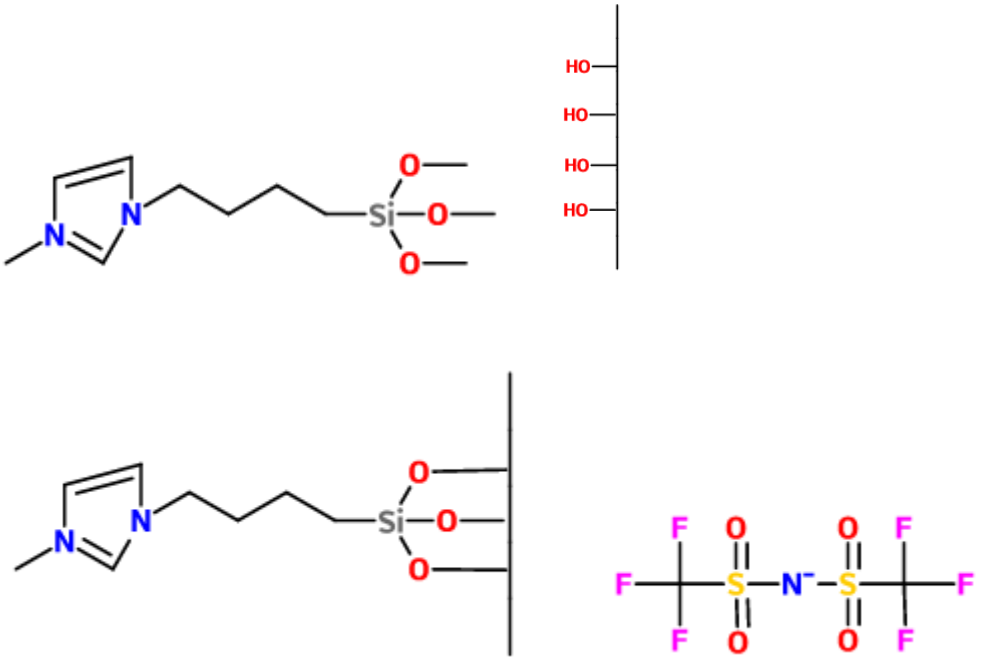

Figure 6.2. Structure of imidazoe based silane-ionic liquid with TFSI anion and its reaction with alumina surface.

The IL-functionalized alumina membranes show no major appearance change. SEM picture in **Figure** 6.3 confirms that the nano-structure of the functionalized alumina also remain unchanged. EDAX analysis on the alumina surface show no obvious elemental signals other than aluminum (near 1.5keV) and oxygen (near 0.55keV), which probably means only few ionic liquid molecules are attached on the surface. It is also confirmed by FTIR that the surface chemistry of the nanoporous alumina undergoes no remarkable transformation. The peaks appear on the FTIR spectra of the alumina before and after the functionalization are very similar.

The only technique that allows us to identify the functionalized alumina membranes so far is the dielectric spectrometer. **Figure** 6.4 reports the AC conductivity of the alumina

membrane/PC before and after reaction, as well as the conductivity of the functionalized alumina being washed for different periods of time. It is shown that the conductivity of the functionalized alumina reaches 10^{-4} S/cm even being washed in ether/ethanol for two days. Such conductivity is at least two orders of magnitude higher than that of the pristine alumina. The functionalized alumina membranes have been further rigorously washed for 5 days. The conductivity only show a slight decrease, meaning most ionic liquids are stably attached. However, one should note that even though the conductivity of alumina is remarkably enhanced by functionalization with ionic liquid, a conductivity of 10^{-4} S/cm is still below expectation considering the high ionic conductivity of ionic liquid. In order to better characterize the IL/alumina system, TGA has been used to quantify the amount of ionic liquid that is grafted in the porous alumina. It is shown in TGA (**Figure** 6.5), only 1% of weight is observed even though the temperature is raised up to 600 ^{o}C. Thus, it can be concluded that only trace amount of ionic liquid is chemically grafted on the alumina surface.

The low grafting density of ionic liquid may originate from the low surface area of the nanoporous alumina. Although the porosity of alumina membrane reaches as high as 50%, most of the pores are actually straight channels that show large volume voids instead of large surface area. BET analysis has been used to quantify the surface area and the volume of nanoporous alumina as shown in **table** 6.1. It is clear that nanoporous alumina exhibits very limited surface area available for functionalization. The same BET experiment has been performed on nanoporous silica. As expected, the irregular and torturous structure of nanoporous silica enlarges the surface area. But the total surface area is still not sufficient for functionalization.

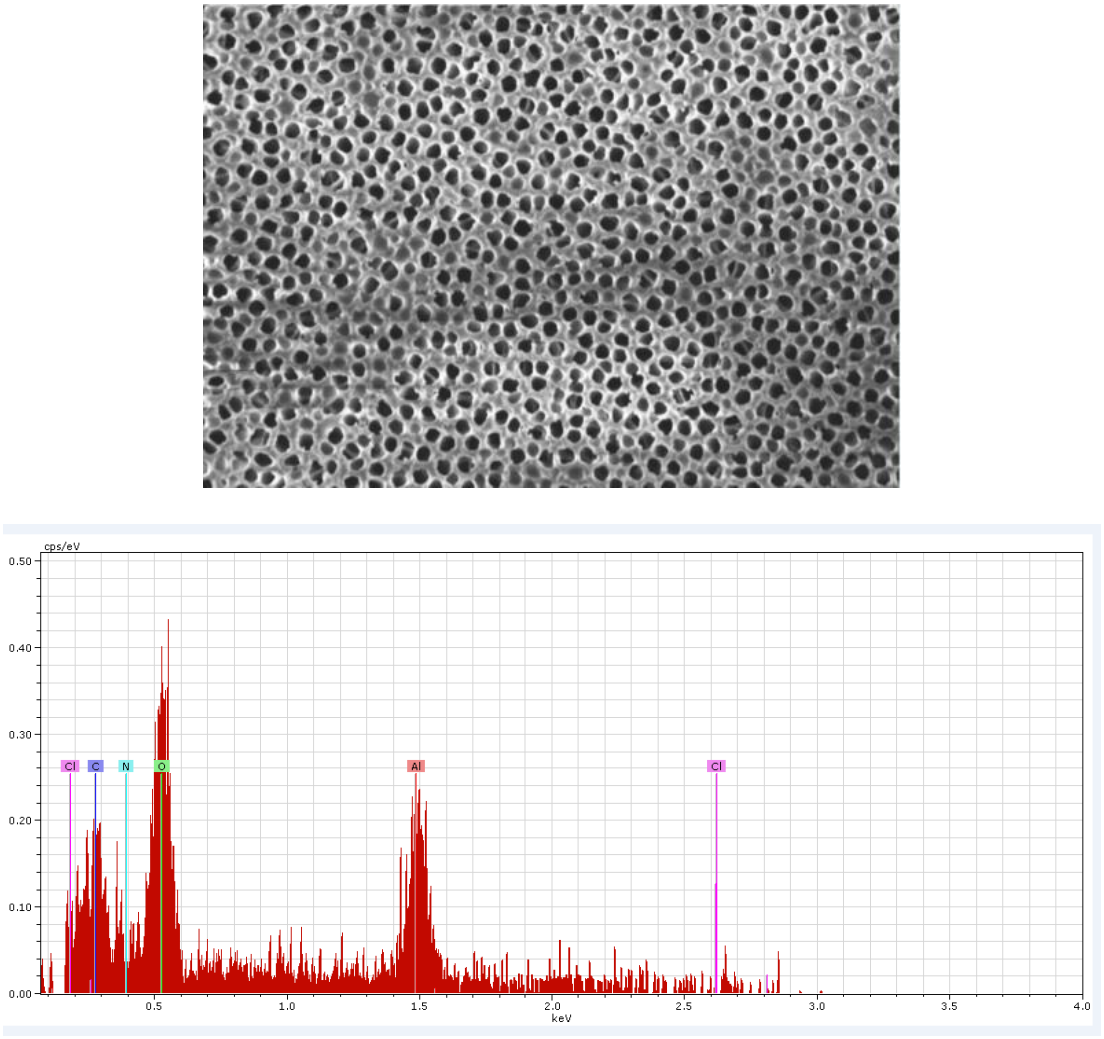

Figure 6.3. SEM image of ionic liquid functionalized alumina and EDAX analysis

`

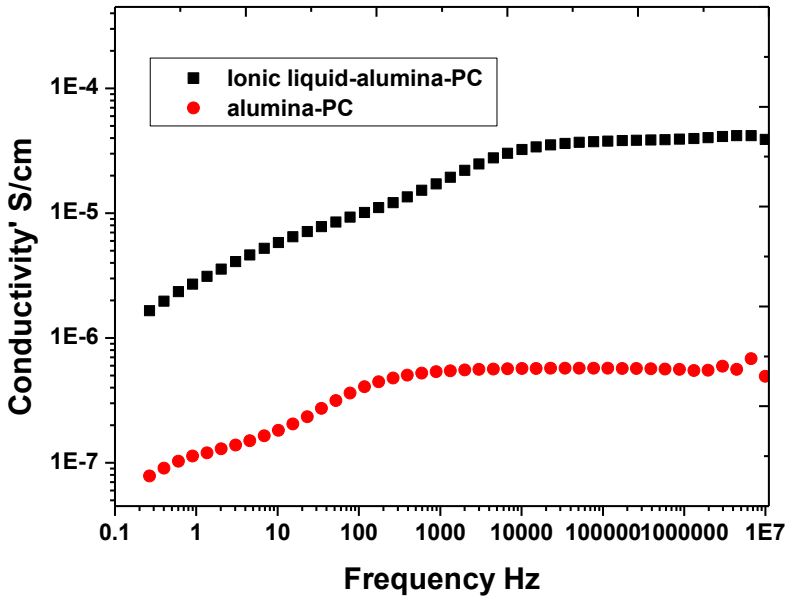

Figure 6.4. AC conductivity of ionic liquid functionalized alumina/PC (black) compared with that of the pristine alumina/PC (red).

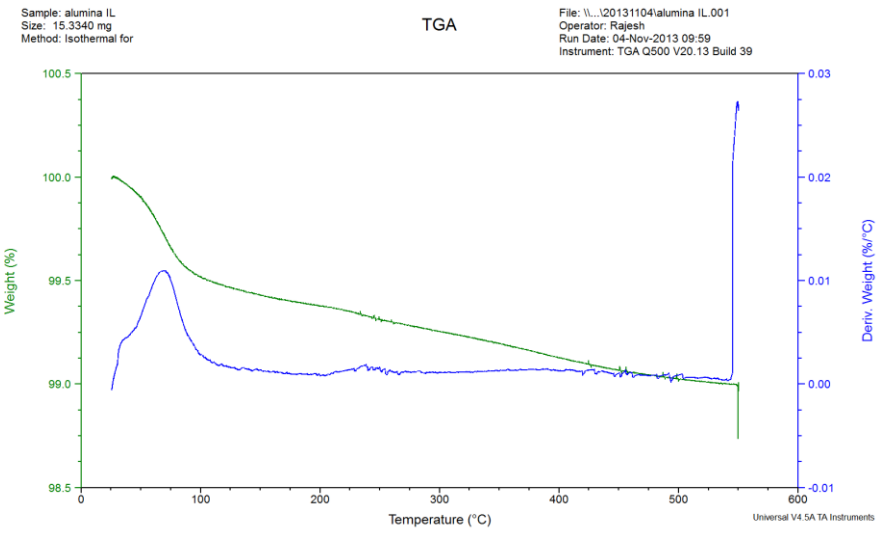

Figure 6.5. TGA profile of ionic liquid functionalized alumina.

Surface Area of silica membrane		Surface Area of alumina membrane	
Single point surface area at P/Po = 0.299652563:	16.7606 m ²/g	Single point surface area at P/Po = 0.299573093:	4.2509 m ²/g
BET Surface Area:	17.2330 m ²/g	BET Surface Area:	4.4460 m ²/g
Langmuir Surface Area:	25.8692 m ²/g	Langmuir Surface Area:	6.8486 m ²/g
t-Plot External Surface Area:	13.0800 m ²/g	t-Plot External Surface Area:	4.4850 m ²/g
BJH Adsorption cumulative surface area of pores between 17.000 Å and 3000.000 Å diameter:	13.404 m ²/g	BJH Adsorption cumulative surface area of pores between 17.000 Å and 3000.000 Å diameter:	3.400 m ²/g
BJH Desorption cumulative surface area of pores between 17.000 Å and 3000.000 Å diameter:	17.9890 m ²/g	BJH Desorption cumulative surface area of pores between 17.000 Å and 3000.000 Å diameter:	4.5482 m ²/g

Table 6.1 BET measurement results of nanoporous silica and nanoporous alumina

Active polymer/nanoporous alumina laminates

As described in the introduction, a second approach to functionalize polymer/alumina composite separator/electrolyte is to laminate alumina with lithiated polymer. We have firstly attempted to laminate nanoporous alumina with PAA and PSS due to their simple chemical structure and broad application as polyelectrolyte. After being laminated by solvent casting, the conductivity of PAA/alumina/PC and PSS/alumina/PC increase by an order of magnitude compared with that of the pure alumina/PC (**Figure** 6.6). However,

the high crystallinity of PAA and PSS leads to the brittleness of the polymer lamination layer, which not only deteriorate the mechanical support for alumina, but also increase the difficulty to handle the materials. Thus it is decided that PAA, PSS and their derivatives are not suitable for polymer/alumina laminated system.

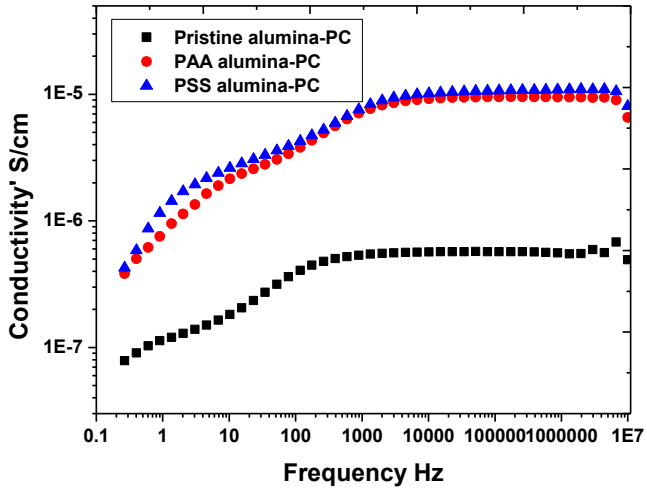

Figure 6.5. AC conductivity of PAA/alumin/PC, PSS/alumina/PC and alumina/PC

We have then turned our attention to apply Nafion, a commercial perfluorinated polymer with sulfonic acid side chains, as the polymer laminate. Nafion has been commercialized by DuPont Company in late 1960s and is generally used as proton exchange membrane for fuel cells. It shows high proton conductivity, great thermal/electrochemical stability and satisfactory mechanical property. Recently, some literature report that Nafion can be lithiated and thus exhibit promising property as separator for lithium battery [10]. More importantly, it is easy to prepare intact Nafion thin layers on both sides of alumina through solvent casting without encountering crystalline problem. Thus, we have focused

on studying the suitability of Nafion/alumina laminated composite as the separator in the lithium battery.

The lithiated Nafion/nanoporous alumina composites are prepared as described in the experiment section. **Figure** 6.6 reports the FTIR of the Nafion/alumina membrane before (red) and after (purple) the lithiation. The peak at 1052 cm^{-1} shifts to 1075 cm-1 after lithiation, indicating the transformation from O-H group to O-Li group. TGA data (**Figure** 6.7) shows that the Nafion is thermally stable at the temperature above 350 ^{o}C, and the weight loss after 400^{o}C is attributed to the decomposition of Nafion.

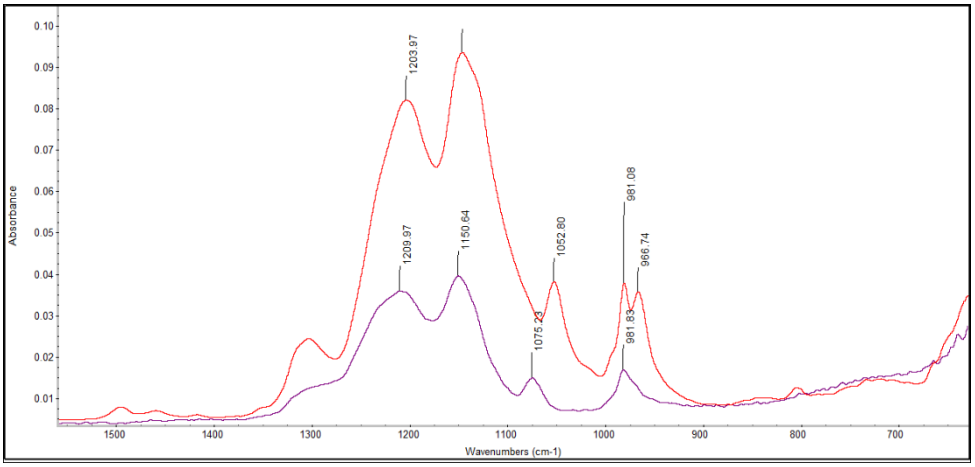

Figure 6.6. FTIR plot of the Nafion/nanoporous alumina before and after lithiation.

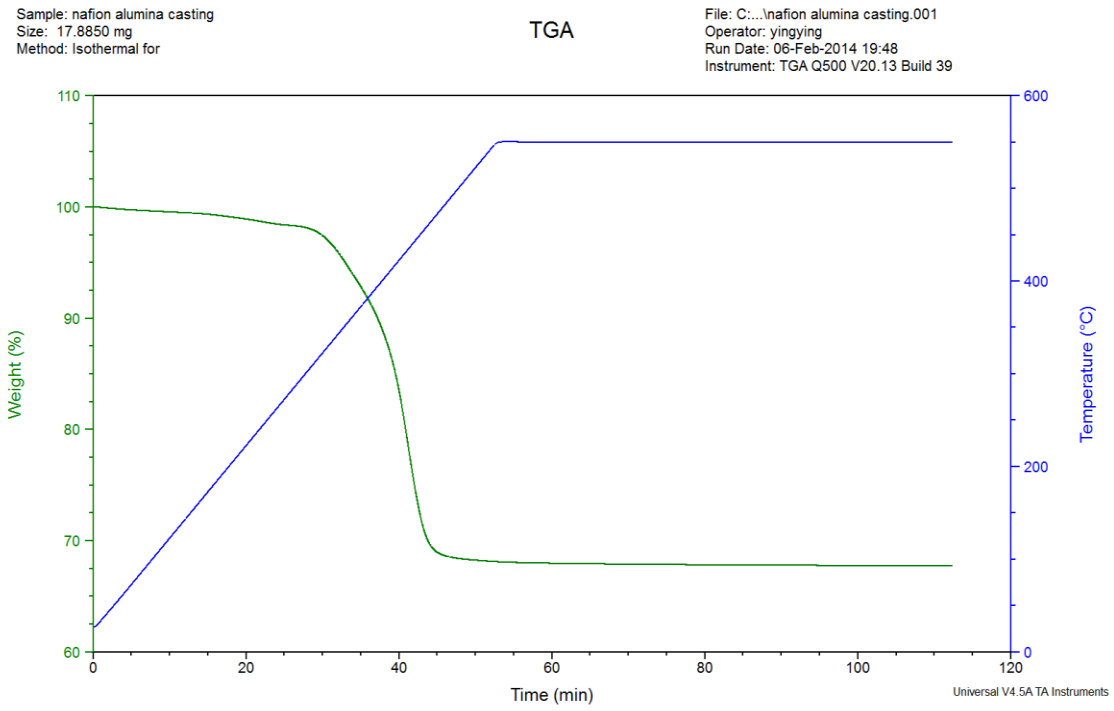

Figure 6.6. TGA profile of the Nafion/nanoporous alumina prepared by solvent casting.

After immersing the Nafion/alumina composite separator in PC or LiTFSI/PC, the Nafion is able to absorb a certain amount of PC and be plasticized. **Figure** 6.7 presents the AC ionic conductivity of the Nafion/alumina composites swollen by PC. Two plateau regions are observed at both low and high frequency, thus two DC ionic conductivity can be extrapolated based on Jonscher's equation [11]. **Figure** 6.8a and b report both low and high frequency DC conductivity of the Nafion/alumina membranes soaked with various electrolyte. As expected, both conductivity increase with the addition of LiTFSI. But the conductivity slightly decrease if the electrolyte is blended with LiF, which is highly likely due to its incomplete disassociation. The low frequency conductivity is lower than the high frequency conductivity, but it exhibits a more typical Arrehnius behavior. On the

contrary, the high frequency conductivity only presents a weak correlation with the variation of the temperature.

Impedance spectra are able to provide more insightful information about ion transportation in the electrolyte. **Figure** 6.8a compares the impedance spectra of Nafion/alumina soaked with a number of electrolyte at 25^{o}C. It is observed that both the bulk impedance of Nafion/alumina/PC decrease with the increasing of LiTFSI concentration. Figure 6.8b and c report the temperature-dependent impedance spectra of Nafion/alumina/1M LiTFSI/PC and Nafion/alumina/PC. In both cases the interfacial resistance drastically decrease with increasing temperature. However, the bulk resistance only weakly dependent on the temperature. Combining with the conductivity data, it is concluded that the high frequency conductivity is attributed to the bulk conductivity while the low frequency conductivity may relate to interfacial transport.

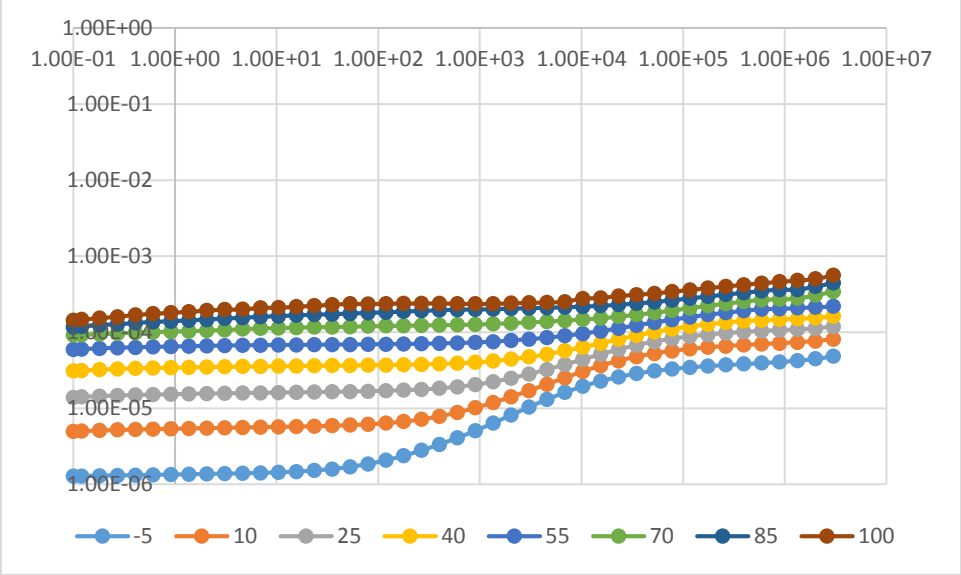

Figure 6.6. AC conductivity of the Nafion/nanoporous alumina soaked in PC.

a)

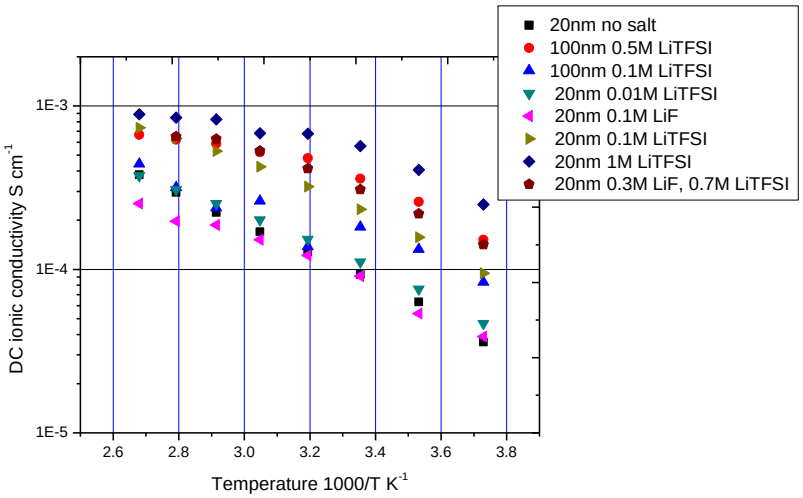

b)

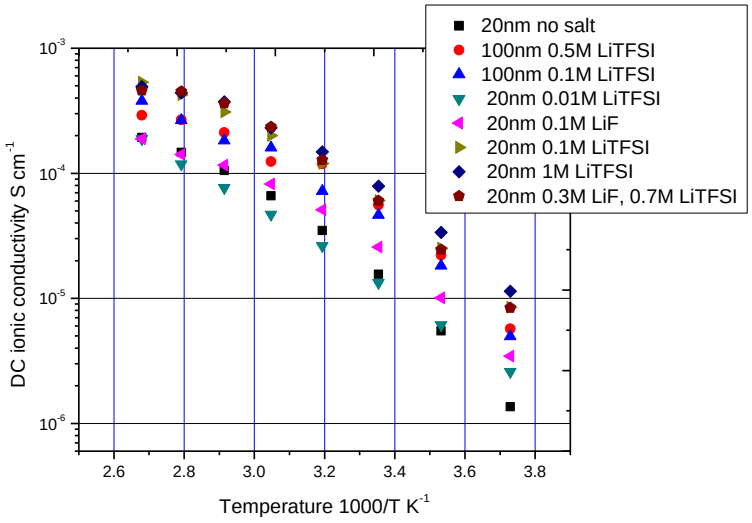

Figure 6.7. DC ionic conductivity of Nafion/alumina with various electrolyte. a) the conductivity extrapolated from low frequency region; b) the same from high frequency region.

a)

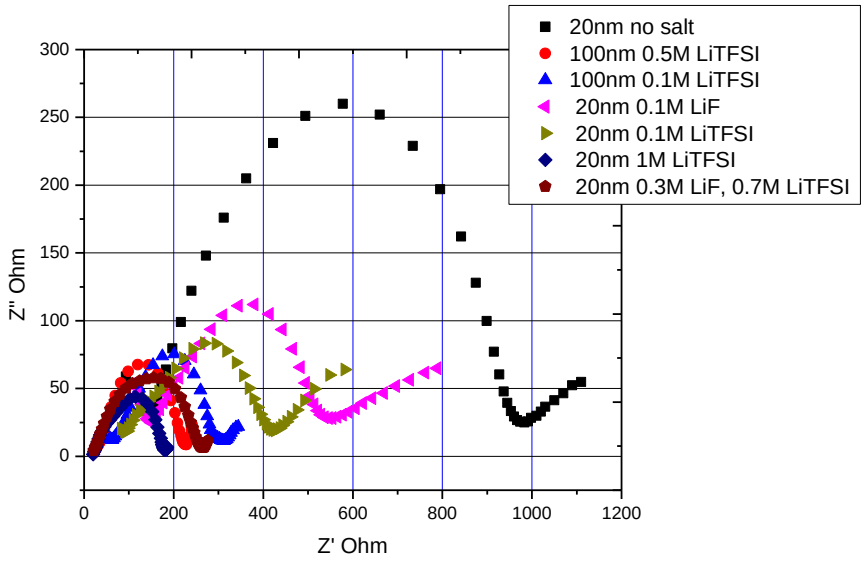

b) c)

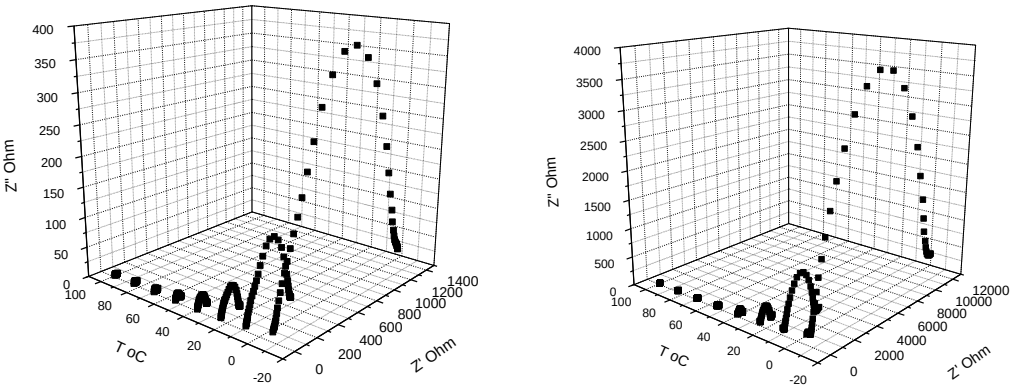

Figure 6.8. a) the comparison of the impedance spectra of Nafion/alumina soaked with a number of electrolyte at 25°C; b) temperature-dependent impedance spectra of Nafion/alumina/1M LiTFSI/PC; c) temperature-dependent impedance spectra of Nafion/alumina/PC;

Reference

1. Brissot, C., et al., *In situ study of dendritic growth in lithium/PEO-salt/lithium cells.* Electrochimica Acta, 1998. **43**(10-11): p. 1569-1574.
2. Brissot, C., et al., *In situ concentration cartography in the neighborhood of dendrites growing in lithium/polymer-electrolyte/lithium cells.* Journal of the Electrochemical Society, 1999. **146**(12): p. 4393-4400.
3. Rosso, M., et al., *Dendrite short-circuit and fuse effect on Li/polymer/Li cells.* Electrochimica Acta, 2006. **51**(25): p. 5334-5340.
4. Agrawal, R.C. and G.P. Pandey, *Solid polymer electrolytes: materials designing and all-solid-state battery applications: an overview.* Journal of Physics D-Applied Physics, 2008. **41**(22).
5. Nugent, J.L., S.S. Moganty, and L.A. Archer, *Nanoscale organic hybrid electrolytes.* Advanced Materials, 2010. **22**(33): p. 3677-3680.
6. Chazalviel, J.N., *Electrochemical Aspects of the Generation of Ramified Metallic Electrodeposits.* Physical Review A, 1990. **42**(12): p. 7355-7367.
7. Kerr, J.B., et al., *Interfacial behavior of polymer electrolytes.* Electrochimica Acta, 2004. **50**(2-3): p. 235-242.
8. Lu, Y.Y., et al., *Ionic Liquid-Nanoparticle Hybrid Electrolytes and their Application in Secondary Lithium-Metal Batteries.* Advanced Materials, 2012. **24**(32): p. 4430-4435.
9. Popat, K.C., et al., *Surface modification of nanoporous alumina surfaces with poly(ethylene glycol).* Langmuir, 2004. **20**(19): p. 8035-8041.

10. Dias, F.B., L. Plomp, and J.B.J. Veldhuis, *Trends in polymer electrolytes for secondary lithium batteries.* Journal of Power Sources, 2000. **88**(2): p. 169-191.

11. Jonscher, A.K., *The Universal Dielectric Response and Its Physical Significance.* Ieee Transactions on Electrical Insulation, 1992. **27**(3): p. 407-423.